1

REPORT DOCUMENTATION PAGE

Form Approved
OMB No. 0704-0188

Public reporting burden for this collection of information is estimated to average 1 hour per response, including the time for reviewing instructions, searching existing data sources, gathering and maintaining the data needed, and completing and reviewing this collection of information. Send comments regarding this burden estimate or any other aspect of this collection of information, including suggestions for reducing this burden to Department of Defense, Washington Headquarters Services, Directorate for Information Operations and Reports (0704-0188), 1215 Jefferson Davis Highway, Suite 1204, Arlington, VA 22202-4302. Respondents should be aware that notwithstanding any other provision of law, no person shall be subject to any penalty for failing to comply with a collection of information if it does not display a currently valid OMB control number.
PLEASE DO NOT RETURN YOUR FORM TO THE ABOVE ADDRESS.

1. REPORT DATE *(DD-MM-YYYY)*
8/4/03

2. REPORT TYPE
Final Report

3. DATES COVERED *(From - To)*
2/1/99-4/30/03

4. TITLE AND SUBTITLE
Dynamics and Acoustics of Trailing Edge Flows at High Reynolds Numbers

5a. CONTRACT NUMBER

5b. GRANT NUMBER
N00014-99-1-0341

5c. PROGRAM ELEMENT NUMBER

6. AUTHOR(S)
Steven L. Ceccio and David Dowling

5d. PROJECT NUMBER

5e. TASK NUMBER

5f. WORK UNIT NUMBER

7. PERFORMING ORGANIZATION NAME(S) AND ADDRESS(ES)
Mechanical Engineering
2011 Automotive Lab
University of Michigan
Ann Arbor, MI
48109-2121

8. PERFORMING ORGANIZATION REPORT NUMBER

9. SPONSORING / MONITORING AGENCY NAME(S) AND ADDRESS(ES)
Office of Naval Research
800 N. Quincy St., BCT 1
Arlington, VA 22217-5660

10. SPONSOR/MONITOR'S ACRONYM(S)
ONR

11. SPONSOR/MONITOR'S REPORT NUMBER(S)

12. DISTRIBUTION / AVAILABILITY STATEMENT
distribution unlimited

DISTRIBUTION STATEMENT A
Approved for Public Release
Distribution Unlimited

13. SUPPLEMENTARY NOTES

14. ABSTRACT
This project involved high Reynolds number testing and measurements of the flow around a two-dimensional hydrofoil having a Navy-relevant cross section. Three multi-week test campaigns in the US Navy's William B. Morgan Large Cavitation Channel were completed. These experiments extended the Reynolds number range of prior hydrofoil tests by more than an order of magnitude. The measurements included laser-Doppler velocimetry profiles and spectra, particle-imaging velocimetry flow fields, static surface pressure distributions, dynamic surface pressure fluctuations, and hydrofoil vibration. This experimental effort emphasized the flow physics leading to trailing-edge vortex shedding. The main outcomes of this work are a complete fluid mechancial data set for use in development, testing, and validation of high Reynolds number flow models; and insight and understanding of the fluid phenomena that lead to trailing edge vortex shedding.

15. SUBJECT TERMS

20030826 029

16. SECURITY CLASSIFICATION OF: unclassified			**17. LIMITATION OF ABSTRACT**	**18. NUMBER OF PAGES**	**19a. NAME OF RESPONSIBLE PERSON** S. L. Ceccio
a. REPORT	**b. ABSTRACT**	**c. THIS PAGE**			**19b. TELEPHONE NUMBER** *(include area code)* 734-936-0433

Standard Form 298 (Rev. 8-98)
Prescribed by ANSI Std. Z39.18

A Final Report:

Dynamics and Acoustics of Trailing Edge Flows at High Reynolds Numbers

Steven L. Ceccio and David R. Dowling
Department of Mechanical Engineering
University of Michigan, Ann Arbor, MI 48109-2133
phone: (734) 936-0433 fax: (734) 764-4256 email: ceccio@umich.edu

Grant Number: N00014-99-1-0341

ABSTRACT

This project involved high Reynolds number testing and measurements of the flow around a two-dimensional hydrofoil having a Navy-relevant cross section. Three multi-week test campaigns in the US Navy's William B. Morgan Large Cavitation Channel were completed. These experiments extended the Reynolds number range of prior hydrofoil tests by more than an order of magnitude. The measurements included laser-Doppler velocimetry profiles and spectra, particle-imaging velocimetry flow fields, static surface pressure distributions, dynamic surface pressure fluctuations, and hydrofoil vibration. This experimental effort emphasized the flow physics leading to trailing-edge vortex shedding. The main outcomes of this work are a complete fluid mechancial data set for use in development, testing, and validation of high Reynolds number flow models; and insight and understanding of the fluid phenomena that lead to trailing edge vortex shedding.

RESULTS

The main findings of this project are contained in the two attached manuscripts. The research work completed here represents the doctoral dissertation of Dwayne A. Bourgoyne, and the master's thesis of Joshua A. Hamel.

ATTACHMENTS

[1] Bourgoyne, D.A., Hamel, J.A., Ceccio, S.L., and Dowling, D.R. "Time averaged flow over a hydrofoil at high Reynolds number," Journal of Fluid Mechanics, in press, June 2003.

[2] Bourgoyne, D.A., Ceccio, S.L., and Dowling, D.R. "Dynamic flow over a hydrofoil at high Reynolds number," submitted to the Journal of Fluid Mechanics, July 2003.

DISTRIBUTION STATEMENT A
Approved for Public Release
Distribution Unlimited

Time-averaged flow over a hydrofoil at high Reynolds number

(Submitted to the *Journal of Fluid Mechanics*)

**DWAYNE A. BOURGOYNE, JOSHUA M. HAMEL,
STEVEN L. CECCIO AND DAVID R. DOWLING**

Department of Mechanical Engineering
University of Michigan, Ann Arbor, MI 48109, USA

At high Reynolds number, the flow of an incompressible viscous fluid over a lifting surface is a rich blend of fluid dynamic phenomena. Here, boundary layers formed at the leading edge develop over both the suction and pressure sides of the lifting surface, transition to turbulence, separate near the foil's trailing edge, combine in the near wake, and eventually form a turbulent far-field wake. The individual elements of this process have been the subject of much prior work. However, controlled experimental investigations of these flow phenomena and their interaction on a lifting surface at Reynolds numbers typical of heavy-lift aircraft wings or full-size ship propellers (chord-based Reynolds numbers, $Re_C \sim 10^7 - 10^8$) are largely unavailable. This paper presents results from an experimental effort to identify and measure the dominant features of the flow over a two-dimensional hydrofoil at nominal Re_C values from near one million (1M) to more than 50 million (50M). The experiments were conducted in the U. S. Navy's William B. Morgan Large Cavitation Channel with a solid-bronze hydrofoil (2.1 m chord, 3.0 m span, 17 cm maximum thickness) at flow speeds from 0.25 to 18.3 m/s. The foil section, a modified NACA 16 with a pressure side that is nearly flat and a suction side that terminates in a blunt trailing-edge bevel, approximates the cross section of a generic naval propeller blade. Time-averaged flow field measurements drawn from laser-Doppler velocimetry, particle-imaging velocimetry, and static pressure taps were made for two trailing-edge bevel angles (44° and 56°). These velocity and pressure measurements were concentrated in the trailing edge and near wake regions, but also include flow conditions upstream and far downstream of the foil, as well as static pressure distributions on the foil surface and test section walls. Observed Reynolds-number variations in the time-averaged flow over the foil are traced to changes in suction-side boundary layer transition and separation. Observed Reynolds-number variations in the time-averaged near wake suggest significant changes occur in the dynamic flow in the range of Re_C investigated.

1. Introduction

Relative motion between a submerged body and a viscous incompressible fluid induces hydrodynamic lift and drag. The shape of the body and the characteristics of its flow field govern the distributions of surface pressure and shear stress that lead to these forces. Typically, the steady or unsteady components of these hydrodynamic forces ultimately determine the utility of the body for potential applications. Air- and water-borne transportation systems are often characterized by turbulent, high-Reynolds number flows. Thus, experimental research in this area commonly strives to deduce scaling laws and cause-and-effect relationships, while computational efforts focus on developing and validating predictive flow models. Unfortunately, the scarcity of experimental studies at high Reynolds numbers hampers all of these approaches. The goal of this paper is to address this situation through the presentation of experimental results for the time-averaged incompressible flow over a lifting surface at Reynolds numbers approaching those of heavy-lift aircraft wings and full-scale ship propellers.

The surface-bounded, near-wake, and far-wake flows formed by a lifting surface are phenomenologically interesting and have practical importance. For example, surface curvature influences boundary layer development, transition, and separation, which together determine the initial conditions for the foil's wake. Given that these phenomena may all behave differently with increasing Reynolds number, any overall scaling for lift, drag, hydroacoustic noise, or other foil-performance measure may result from the interplay of multiple phenomena. On the practical side, high-Reynolds number lifting surfaces are essential for flight, maneuvering, propulsion, and control of air- and water-borne vehicles. In such applications, the lifting surface is designed to meet performance criteria. Given the complexity of flow phenomena and the wide range of length and time scales that must be managed in high-Reynolds number turbulence, it is safe to say that the development of the needed design tools is not yet complete. For lifting surfaces in incompressible flow, this situation exists in part because of the lack of controlled experimental data at full-scale chord-based Reynolds numbers, $\mathrm{Re}_C = U_o C/\nu$ (where U_o is the flow speed far upstream of the foil, C is the foil chord, and ν is the kinematic viscosity of the flowing liquid). Few experimental results exceed Re_C of several million (M) while many applications lie in the Re_C range of 30M to 100M.

This paper presents the results of an experimental study of the flow over a two-dimensional hydrofoil for Re_C values from near 1M to more than 50M. The foil has a nearly flat pressure side and a NACA-16 suction side modified with a rounded trailing edge bevel of apex angle 44° (Geometry I) or 56° (Geometry II). The foil section is typical of naval propeller blades of moderate thickness and chamber, and was chosen for its application-relevance and its potential for Re-dependent flow features. In particular, three-dimensional propeller design techniques often rely on two-dimensional section performance data (Kerwin 1986). Also, the trailing-edge bevel – typically introduced on propeller blades for structural integrity during severe off-design operations – leads to a compact region of flow separation whose characteristics depend on bevel geometry and Reynolds number. The present experimental effort is concentrated on this near-trailing-edge region, and the results reported here augment the available measurements of flat plate boundary layer flows (Eaton and DeGraaff 2000, Österlund et al. 2000) suitable to test high-Reynolds-number exterior-flow models.

The principal goals of this study were to identify phenomena that affect foil performance at high Reynolds number, and to provide a comprehensive data set for validation of high Reynolds number numerical models. Here, foil performance includes lift, drag, and the prevalence of near wake vortex shedding, an important hydroacoustic noise source for non-cavitating lifting surfaces (see Blake 1986, Blake and Gershfeld 1989, or Howe 1998). The measurements reported here document only the time-averaged flow over the foil, but even these results display interesting Reynolds number dependences resulting from the interplay of boundary layer transition, flow separation, and wake formation. Featured prominently in this interplay is the phenomenon of near-wake vortex shedding, though these findings are beyond the scope of this paper.

Prior results documenting the mean flow at low-Mach number on foils, struts, and turbine blades has been largely motivated by the need to understand and predict lifting-surface performance, and possibly eliminate vortex shedding. Early work in this area, particularly for compact bodies, is reviewed in Bearman (1965); a more recent review is provided in Blake (1986). Mean velocity profiles in the boundary layer and in the near wake of minimally lifting struts are provided in Blake (1975) for Re_C of ~ 2M. The findings of the present effort are similar to these but extend the range of experimental Re_C to more than 50M and include the influence of lift. More recent research on individual foils and struts experiencing steady inflow conditions has been computational (Wang and Moin 2000, 2002), but again, at lower Re_C than reached in the present studies. This situation is similar for unsteady foil-flow studies (Luire et al. 1998, Ho and Lakshminarayana 1997) where Re_Cs only as high as 4M have been investigated.

Low-Mach number airfoil studies cover many of the same phenomena presented in this paper. Boundary layer transition on airfoils is reviewed in Malick (1997) and a recent prediction technique is presented in Brodeur and van Dam (2000). Experimental studies of steady (Bastedo and Mueller 1986, Fitzgerald and Mueller 1990) and unsteady (Covert and Lorber 1982) boundary layer separation have been conducted at Re_C values from 0.14M to 0.7M. Mean and turbulent flow fields in the vicinity of boundary layer separation on an asymmetric trailing edge in a two-stream wind tunnel are reported in Thompson and Whitelaw (1985). Here, at $Re_C \sim 2M$, it was determined that the boundary layer flow that enters the separated region near the trailing edge significantly influences the development of the wake. The present study shows that this result persists at higher Re_C. A general review of turbulent boundary layer separation is provided in Simpson (1989).

Research into the performance of compressor and turbine blades and cascades has many similarities to the current study as well, including the emphasis on lift, drag, boundary layer development, trailing edge characteristics, and near-wake vortex shedding. A review of this literature prior to 1987 is provided in a series of papers (Deutsch and Zeirke 1987, 1988a,b) where experimental results at $Re_C = 0.5M$ are reported. More recent experimental (Umbaldi 1996, Halstead et al. 1997a) and computational (Halstead et al. 1997b) efforts cover single- and multi-stage cascades at Re_C's up to 1.6M and 0.6M, respectively. In addition, measurements of boundary layer transition and separation conducted on flat plates at turbine-blade conditions are reported in Volino and Hultgren (2000) for plate-length-based Reynolds numbers up to 0.3M.

All of the experimental work described above on foils, struts, and blades involves test models having Re_C values at or below 4M. Furthermore, prior steady-flow results at or above $Re_C = 2M$ involve minimally lifting struts with section lift coefficients that fall below that typically sought for propeller blades or aircraft wings. By comparison, the current test model generated significant lift forces, and represents an important step towards the understanding of practical, three-dimensional propeller blades. Moreover, the Re_C values in the current experiments are high enough to comfortably span the gap between the prior studies and many full-scale applications.

The remainder of this paper presents our results, observations, and analysis of the time-averaged low-Mach number flow over a two-dimensional hydrofoil with two different trailing edges. The next section describes the test model, flow facility, experimental apparatus, and measurement techniques. The third section provides the results for the mean flow upstream, on the surfaces, and in the wake of the hydrofoil, with emphasis on the trailing-edge region under variations of Reynolds number and geometry. These data are used to determine how the growth of boundary layers on the suction and pressure sides of the hydrofoil influence the separated region at the trailing edge. The fourth section discusses these results and attempts to link the observed phenomena to well-established Reynolds number trends in turbulent wall-bounded flows and wakes. The final section summaries the effort and presents the conclusions drawn from this work.

2. Experimental Setup and Techniques

The high Reynolds numbers of this experiment were achieved with a large hydrofoil tested in the U.S. Navy's William B. Morgan Large Cavitation Channel (LCC). The LCC is a low turbulence re-circulating water tunnel with a 3.05 m × 3.05 m × 13 m test section and is capable of steady flows from 0.25 to 18.3 m/s (Etter and Wilson 1992). The hydrofoil spanned the test section and was mounted near its geometric center (see Figure 1). Gaskets at the hydrofoil-wall junction prevented bypass flow, and tunnel blockage based on the hydrofoil's maximum thickness (0.171 m) was 6%. The ratio of the foil chord to the vertical test section dimension was 0.70. The foil's angle of attack, α, was measured between the tunnel axis and the flat pressure side of the hydrofoil. For all results reported here, the foil was mounted at $\alpha = 0°$, measured within an estimated uncertainty of +/-0.05°. At the maximum flow speed of 18.3 m/s and $\alpha = 0°$, the hydrofoil generates approximately 590 kN (60 metric tons) of lift. At this speed and the facility's limit on water temperature (104° F), a maximum Re_C value of 61M was achieved.

Testing was conducted in three experimental campaigns (separate testing periods of approximately six-week duration) with the first campaign measurements limited to laser Doppler velocimetry (LDV). Between the first and second testing campaigns, debris was discovered in the LCC's flow management section, and an assessment has been made of its impact on the test results. Measurements from the first campaign (with debris) showed spatial variation in the time-averaged inflow freestream velocity of approximately +/-1%, over the measured flow range of 3 to 18.3 m/s. Measurements of the root-mean-square (RMS) of freestream velocity near the leading edge of the hydrofoil, though insufficient to fully characterize the inflow turbulence, limit its value to +/-1.5% of the velocity far upstream. After debris removal, extensive freestream uniformity and turbulence measurements were made in the empty test section at a streamwise location corresponding roughly to the hydrofoil's leading edge. Over the full range of facility flow speeds, spatial variation of the mean freestream velocity was within +/-0.5%, and the RMS of freestream velocity was within 0.5% of the velocity far upstream (Cutbirth and Park 2002). These conditions apply to the second and third testing campaigns in which selected trailing edge LDV measurements were repeated and all other data were acquired. Though the debris measurably affected inflow uniformity and may have elevated freestream turbulence, a critical comparison of the LDV measurements repeated between campaigns did not reveal flow variation exceeding experimental uncertainty.

The hydrofoil test model was cast from Ni-Al bronze, machined to the specified shape (Jessup 1999) and polished to a RMS surface roughness of 0.25 μm. Using flat plate boundary layer scaling, this roughness represents $k^+ < 1$ at the highest test speed, and thus the clean foil may be considered hydrodynamically smooth (White, 1991). However, for PIV flow measurements the tunnel was flood-seeded with silver-coated glass spheres of 16 μm mean diameter. The gradual accumulation of these particles varied the effective surface finish of the hydrofoil, and the large tunnel drain and fill times made frequent cleaning impractical. The diameter of these particles was equivalent to $k+ \sim 20$ at the highest Re_C tested. As will be discussed in Section 3.2, these particles may have affected boundary layer transition. Otherwise, no boundary layer tripping device was employed.

The hydrofoil cross section is depicted in Fig. 2 and provided in table form in Appendix A. Both the figure and coordinates reflect a hypothetical sharp trailing edge. In reality, a 0.4-mm radius was applied to the geometry specified, reducing the chord by a negligible amount. Fig. 2a also defines the coordinate frames used in this paper. In the *tunnel coordinate frame*, the streamwise coordinate, x, is defined by the tunnel axis, and vertical coordinate, y, is taken normal to x. (The spanwise coordinate, z, completes the set of right-handed Cartesian coordinates). The vertex of the trailing edge bevel angle is defined as the coordinate $(x/C, y/C) = (1,0)$. In the *surface-aligned coordinate frame*, the t coordinate is defined by the local surface tangent with the h coordinate taken normal to t. Finally, some results are presented in a rotated Cartesian coordinate frame defined by h and t at 93% chord. This frame is designated the *trailing edge coordinate frame.*

A bolt-on trailing edge modification was used to vary the suction side bevel geometry. The two bevel designs tested are shown on Fig. 2b: the more streamline trailing edge, Geometry I (bevel radius, $R_B = 76.2$ mm and apex angle, $\beta = 44^o$), and the more bluff trailing edge, Geometry II ($R_B = 38.1$ mm, $\beta = 56^o$). Both geometries generate suction side boundary layer flow separation in the last 2% of the chord. Laser-based metrology on the finished Geometry-I hydrofoil confirmed a typical tolerance of +/-0.2 mm and a maximum tolerance of +/-0.5 mm between the as-designed and as-built geometries. The trailing edge of Geometry II, which was applied in the field, could not be constructed to as high a tolerance. Therefore, the geometry given in Figure 2b and Appendix A is the as-built geometry, measured to within +/-0.5 mm.

The hydrofoil experiments were conducted using well-established water tunnel testing techniques for fluid velocity and static pressure measurements. Test section pressure was held constant and sufficiently high to suppress significant cavitation. Test section flow speed was controlled through the rotational velocity of the tunnel's axial-flow impeller and monitored by a fixed LDV probe. Tunnel water temperature was monitored but not controlled; it increased by as much as 1.3°C/hr during tests at 18.3 m/s and varied between 24 and 40°C over the course of the tests. As a result, water viscosity and the Re_C achieved at a given test speed varied by as much as 20%. Table 1 lists the nominal Re_C values based on an average water temperature of 32°C. Measurements of vibration in a bandwidth from 2 Hz to 1 kHz were made with eight accelerometers (Wilcoxon 754-1) distributed within the hydrofoil. These measurements confirmed that the hydrofoil was effectively rigid even when unsteadiness developed in the foil's near wake.

Static pressure measurements were made on the hydrofoil using 30 taps distributed along the suction and pressure side surfaces. Each tap was progressively offset by in the spanwise direction by 40 mm, and all taps were contained within the middle 50% of the span. Leading edge taps at $x/C \leq 0.03$ were 0.8 mm in diameter and the remaining taps were 1.6 mm in diameter. The measurements were made with a Rosemont differential pressure transducer (3051CD, +/-250 kPa, differential) referenced to a 1.6 mm-diameter tunnel wall tap at $x/C = -2.38$, and routed to individual hydrofoil taps with a rotary sampling valve (Scanivalve J-type). The pressure transducer was calibrated with a pressure standard (Paroscientific 740 DigiQuartz, 124 kPa, differential) of accuracy +/-12 Pa. Significant sources of static pressure measurement uncertainty include (1) uncertainty in the calibration method, (2) transducer non-linearity, (3) zero bias, and (4) hole error (see Benedict 1984). At Re_C=50M, hole error governs, and the overall uncertainty is +/-0.006 in pressure coefficient units. At Re_C=4M and excluding zero bias, calibration error governs, and the overall uncertainty is +/-0.015. However, at all but the highest Re_C, transducer drift between calibrations produced zero bias in excess of the other uncertainties. The LCC's flow deceleration time precluded zero-flow measurements at a frequency sufficient to address this zero bias. Consequently, corrections for zero bias have been made by matching the pressure coefficient near mid-chord (average of the three mid-chord taps) on the hydrofoil's pressure side to that on the Geometry I hydrofoil at Re_C = 50M. This method produces static pressure distributions that are consistent with the steady Bernoulli equation using LDV-acquired velocities outside the boundary layer on the pressure side of the trailing edge and on the suction side near mid-chord. The method also yields pressure coefficient values at the leading edge tap consistent with the free-stream stagnation pressure. Computation of pressure gradients, lift, and drag are not affected by the zero-bias error correction.

Static pressure measurements were also made on the walls and ceiling of the test section. Wall taps extended along three lines from $-3.0 < x/C < 3.0$ at $y/C = -0.19$, 0.04, and 0.26, respectively. Single taps were located at mid-span on the test section ceiling ($y/C=0.71$) at $x/C = 0.0$, 0.5, and 1.0. All wall and ceiling taps were 1.6 mm in diameter and were routed via solenoid-actuated ball valves to a second differential pressure transducer (Rosemount 3051P, 6350 mm-water differential). For the tunnel wall pressure data, zero flow measurements were used to correct the transducer zero bias. At Re_C = 50M, the overall uncertainty is governed by hole error and is estimated to be ±0.006 in pressure coefficient units. At Re_C = 4M, the uncertainty of the calibration governs and the overall uncertainty rises to ±0.015.

Flow velocities above and below the foil were measured with three systems: *i*) a two-component Dantec laser-Doppler velocimetry (LDV) at 0.25 span, *ii*) a two-component Particle Imaging Velocimetry (PIV) system at 0.36 span and iii) a miniaturized one-component LDV probe (Fourguette, *et al.*, 2001) housed within the hydrofoil body at $x/C = 0.43$ and 0.35 span. Table 2 provides the LDV and PIV measurement locations. Results from all three systems were normalized by the flow speed upstream of the foil, U_o, measured at $x/C = -2.38$ with a dedicated one-component Dantec LDV system. To support LDV acquisition in all three testing campaigns, the LCC was flood-seeded with Silicon Carbide particles of 2 µm mean diameter. To support PIV acquisition in the second and third testing campaign, the channel was additionally seeded in much higher density (0.004 kg/m3) with silver-coated glass spheres of 16 µm mean diameter (Potters Industries, SH400S33).

The fixed and traverse-mounted LDV systems utilized Dantec components including signal processors (BSA57N11), fiber optic probes, a three-dimensional probe traverse, and control software. Laser light was provided by two 6-Watt Argon-Ion lasers (Spectra Physics 2016 and 2017). The external 2-component LDV used a Dantec optical head having 111-mm beam spacing and a 1600-mm (in air) focal length. The head was mounted on a large traverse and provided an in-water focal volume of approximately 170 µm in diameter and 6 mm in length. The traverse and the test section windows allowed LDV data collection over approximately the middle 1 m of the test section height. This LDV system was calibrated as a unit using a rotating disk to generate the velocity standard, and separate calibrations were used for low speeds (Re_C=17M and below) and high speeds (Re_C=33M and 50M). The uncertainty in locating the disk center is the dominant source of velocity bias error, and generates uncertainties of +/-

0.04 m/s and +/-0.08 m/s (at the 95% confidence level) for the low and high-speed calibrations, respectively. In comparison with bias error, random error is negligible. To estimate the uncertainty in the normalized velocity data, a distinction must be made between results for which data is taken and normalized by a single LDV system, and data taken and normalized using separate systems. In the former, the uncertainty in the normalized value is 0.08 and 0.004 in normalized units at Re_C=1.4M and 50M, respectively. In the later, uncertainties are generally higher.

To best select a spanwise location for the LDV measurements, the spanwise uniformity of the Geometry I hydrofoil flow was assessed. Measurements at Re_C = 8M and 50M were collected on a coarse grid (50 mm by 50 mm) in a planes perpendicular to the flow direction at fixed x-locations far upstream of the foil and just aft of the trailing edge (Bourgoyne, 2001). Within the resolution of the grid, these measurements showed the time-averaged flow to be two-dimensional over the middle 90% of the foil span. (Side-wall contamination extends out to only 5% span on each side.) Motivated by the higher LDV data rates near the test section windows, this finding was used to justify collection of the remaining LDV at z/S=0.25. (Further findings concerning spanwise uniformity are presented in Section 3.4.)

Measurements in the trailing edge region were taken to confirm repeatability between campaigns. These revealed that the first campaign LDV measurements differed from those of the second two campaigns by a consistent factor of 1.04. This difference was traced to the calibration of the upstream LDV system that monitored U_o. (Due to this error, the normalized velocity data published in Bourgoyne (2001) is overstated by a constant factor of 1.04.) The error was systematically corrected using comparisons between the measurements of U_o from the fixed single-component LDV and the measurements of the local freestream velocities from the traverse-mounted two-component LDV. The correction method relies on the assumption of negligible Re_C-dependence in the local freestream at coordinates y/C > 0.26. Following this correction to U_o, all LDV velocity statistics from all three campaigns match within experimental uncertainty.

Planar PIV instantaneous flow field measurements in the vicinity of the hydrofoil trailing edge were made using a LaVision Flowmaster-3S PIV/PTV system, including two digital cameras (1280 by 1024 pixels) and a PC-based data acquisition system. Light was provided by two flash-lamp-pumped Nd-YAG lasers (Spectra Physics Pro 250-10) delivering 800 mJ per pulse at 532 nm. The laser sheet was masked to 3 mm thickness and relayed downward through the top of the LCC test section to illuminate the suction-side trailing edge and near wake. The pressure side of the hydrofoil was not illuminated. Due to test section geometry, the laser sheet could not be installed at the spanwise location of the LDV and was instead installed at the nearest practical location (z/S=0.36). The two cameras were operated in tandem at a magnification of 0.1 mm/pixel to capture a composite field of view. Camera depth of field exceeded the light sheet thickness. Raw images from the two cameras were processed individually using LaVision's DaVis v6.0.4 analysis software in cross-correlated mode with 32 by 32 pixel interrogation areas. Accordingly, each PIV vector produced is the result of particle-pair averaging over a cube of flow measuring approximately 3 mm on a side. Images were acquired at a rate of approximately 1 Hz.

The PIV image magnification was optimized to capture in a single frame the wake physics of interest and produce typical particle image diameters of 3 pixels. The optimal time between images was governed by the low velocities in the re-circulating region of the near wake, and produced a field-averaged particle displacement of approximately 7 pixels. This determined the minimum suitable interrogation area of 32 by 32 pixels, typically capturing 10 particle pairs. The raw images were good. For example, when processed with a single-pass calculation for each interrogation area, they produced vector fields with less than 10% erroneous vectors and an average peak ratio (ratio of the magnitudes of highest and second-highest cross-correlation peaks) of 1.8. When processed with an adaptive, multi-pass algorithm, the percentage of erroneous vectors dropped to less than 3% and the average peak ratio improved to 2.6. In the plots presented in this work, the adaptive, multi-pass algorithm was used, and vectors with high uncertainty ($Q<1.8$) were dropped from the sample population.

PIV uncertainties include random and bias error in the velocity measurements and bias error in the spatial location of these velocities. Assuming a characteristic sub-pixel resolution of ±0.25 pixels, the uncertainty due to random error in the velocity magnitude derived from particle pairs with a 7-pixel displacement is ±3%. This estimate is supported by the measured self-consistency of the PIV. Specifically, images of a particle field were taken simultaneously with different cameras and processed by the same PIV algorithm. Comparison of the resulting instantaneous vector fields produced an L_2 error norm of 3% for the velocity magnitudes. An identical comparison of the time-average of 500 instantaneous fields yielded an L_2 error norm of less than 1%. The reduction in the error norm by time-averaging confirms the predominately random nature of the error and supports the estimate of ±3% random error.

Bias error in the PIV velocities is introduced through uncertainty in image scaling. Images of a precision calibration grid mounted to the submerged hydrofoil (in the absence of flow) provided this scale with approximately ±1% accuracy. Velocity uncertainty is also introduced through the normalization velocity, U_o, acquired with the upstream reference LDV, discussed earlier. The combined effect of these sources of error is a characteristic uncertainty of the normalized mean PIV velocities of ±1.5%. Note that this estimate is overstated in regions of high velocity and understated in regions of low velocity.

Simultaneous images from the two cameras are located relative to one another within ±0.2 pixels using a PIV correlation of the overlapping region of the images. The composite velocity field is then located relative to the foil within ±2 pixels (±0.2 mm) using the image of the trailing edge surface and its laser sheet shadow.

3. Results

Experimental data were collected for both trailing-edge geometries for zero angle of attack at the flow speeds and nominal Reynolds numbers listed in Table 1. This table also includes the symbols and line types used in the remainder of this paper to designate Re_C values. Geometry I and II results are reported with filled and open symbols, respectively. The presentation of results follows in subsections devoted to: static and dynamic foil deflections, static pressure profiles, outer (potential) flow results, and inner (viscous) flow results.

3.1 Hydrofoil Deflection and Vibration

Though the foil was made of solid metal and mounted with the greatest practical rigidity, the static lift at Re_C=50M and α=0.0 deflected the trailing edge 8mm at the midspan. At Re_C=33M, this deflection decreased to 3.5 mm. Leading edge static deflections were not measured but should approximate those of the trailing edge based on the near-symmetry of the hydrofoil's cross section, lift distribution, and mounting scheme. Also based on the mounting scheme and system symmetries, the spanwise dependence of the static deflection should approximate that of a simply supported beam under a uniform load. Deflection of this kind may potentially affect the hydrofoil flow. However, the ratio of the maximum midspan deflection to the total hydrofoil span is less than 0.002. For such small deflections, the flow field is presumed to locally approximate that of the undeflected shape.

Measured fluctuating acceleration levels increased rapidly with flow speed but were broadband and did not suggest problems with flow-excited oscillations of foil-tunnel structural modes. At 18.3 m/s (the worst case), the highest RMS surface-normal vibratory speed recorded by any of the eight accelerometers was 1.5 mm/s. This RMS velocity is less than 0.01% of U_o, significantly below the turbulence level of the water tunnel. In addition, the greatest observed change in vibration level occurred between flow speeds of 12 and 18.3 m/s yet the differences between the normalized mean flow fields at these speeds are well within experimental uncertainty. Together these observations suggest that foil vibration was insignificant in these experiments.

3.2 Static Pressures

The pressure coefficient, $C_P = (P - P_o)/\frac{1}{2}\rho U_o^2$ where P is the measured static pressure and ρ is the water density, was measured on the surface of the hydrofoil and on the walls of the LCC test section. The reference pressure P_o was measured at the same upstream location as the reference velocity U_o. Measured C_P values for Re_C between 4M and 50M are shown on Figures 3 and 4 for Geometries I and II, respectively. Following convention, the vertical axes on these figures display $-C_P$; this places the suction side data in the upper half of each figure. For clarity, data at Re_C = 8M and 33M are omitted from Fig. 3, and data from Re_C = 17M and 33M are omitted from Fig. 4. In both cases, the omitted data fall monotonically between the plotted points for neighboring Re_C values. The fitted curves are cubic splines constrained to pass within the uncertainty range of each data point. For each flow speed, the C_P value at x/C = 1 was extrapolated from the suction and pressure side measurements nearest the trailing edge. Variations in the static pressure distributions between measurements at different Re_Cs are small, and are most discernable near the foil's midchord and trailing edge. The left and right inset panels in Figs. 3 and 4 show the leading and trailing edge C_P-data at greater scale, with the location of the suction side separation shown as a shaded region on the x/C axis. The sharp changes in C_P-curve slope near the trailing edge are nearly coincident with the initiation of the suction side bevel depicted in Fig. 2b and denoted by 'Bevel' on the right-side insets of Figs. 3 and 4. Note that the suction side tap at x/C=0.958 with the Geometry II fell within the faired seam of the trailing edge modification and did not have a sharp-edged hole. As a result, the measurements there have increased uncertainty.

A comparison of Figs. 3 and 4 shows that the C_P measurements are similar but there is less variation with increasing Re_C with Geometry II. As might be expected from the geometrical difference, Geometry II allows the foil to maintain a negative suction-side C_P to greater x/C but then the C_P turns positive with a steeper pressure gradient as x/C approaches unity. On both trailing edges, the pressure gradient just prior to boundary layer separation becomes less adverse with decreasing Re_C, a trend linked to the decrease in the $-C_P$-peak near midchord on the suction side. For both edges, the C_P at $x/C = 1$ (the base pressure coefficient) decreases with decreasing Re_C, an indication that the near wake dynamics are changing over this Re_C range. Specifically, the dynamic flow measurements reveal a correlation between reduced base pressure and increased proximity to the trailing edge of developed pressure side vortices (not shown here). A similar relationship was demonstrated by Bearman (1965) for blunt bodies with splitter plates, and is consistent with the increase in drag generally associated with vortex shedding. The Re-dependence of the base pressure is weaker for Geometry II.

Figure 5 presents C_P measured on the tunnel walls above (y/C=0.26) and below (y/C= –0.19) the foil for Re_C = 4M and 50M for Geometry I, and at Re_C = 50M for Geometry II. The foil's mounting system prevented the collection of wall pressure data near mid-chord, so an interpolated data point (*) has been added at the x/C of foil's peak C_P. This value is the average of the measurements on the foil surface and water-tunnel ceiling at the given x/C. With this point, the splined C_P-curves and measured velocities conserve vertical momentum in a control volume enclosing the foil and described in Section 4.5. Here, variation in C_P with Re_C and trailing edge geometry is less than experimental uncertainty except very near the foil.

The foil's lift and test section blockage both contribute to static pressure variations on the test section walls. Given the length of the foil's chord compared to the transverse test section dimension, the lift on the foil produced by bound circulation was determined by the upstream flow speed and the confining effects of the test section walls. At matching free-stream speeds, foil lift would be lower in an infinite environment. Interestingly, the measured C_P on the ceiling of the test section directly above the foil (–0.28, see Fig. 5a) can be used to determine the foil's lift to within a few percent using of a two-dimensional vortex to represent the foil's bound circulation, a source and sink to represent the foil's thickness, and the method of images to account for the tunnel walls.

3.3 Outer mean flow

The measurements presented in this section document the global flow around the Geometry I foil, specifically the tunnel-confined potential-flow. Based on the minimal geometry-dependence of the static pressure coefficient, this data is expected also to approximate the flow over the Geometry II foil. These measurements are presented as vertical profiles of horizontal mean velocity, U, and vertical mean velocity, V, normalized by U_o. Data are presented at stations upstream of the foil, at the trailing edge, and downstream of the foil. The vertical extent of the measurements (see Table 2) is the maximum afforded by the test section windows. All data are for z/S=0.25.

The upstream LDV-acquired average profiles of U and V are provided in Fig. 6a and 6b, respectively, for Re_C = 8M, and 50M just upstream of the hydrofoil leading edge at x/C = – 0.014. The foil's leading edge lies at (x/C, y/C)= (0,0.0092) and is indicated by the dashed line in the figure. The (U, V)-profiles at Re_C = 17M and 33M are identical within data scatter to the results at Re_C = 8M and 50M.

Normalized mean flow velocities (U,V) above and below the foil near its trailing edge, at x/C = 0.930, 0.958, and 1.000 are shown in Fig. 7 for Re_C = 8M, and 50M. Here, a small difference is seen in the data from the two plotted Re_C values, especially for U on the suction side of the foil. Measurements from Re_C = 17M and 33M have been omitted for clarity. If shown, these data would fall smoothly and monotonically between the plotted data in Fig. 7. Velocity profiles from these three x/C locations have been included because they show the strong suction-side outer flow deceleration (compare Fig. 7 a and e) that occurs near to but upstream of the trailing-edge bevel.

Normalized mean flow wake profiles downstream of the foil at x/C = 1.028, 1.070, and 1.43, are shown in Fig. 8 for Re_C = 8M and 50M. As for the near-trailing edge measurements in Fig. 6, only small differences are apparent between the data from these two Re_C's, and the data from Re_C = 17M and 33M (not plotted) fall smoothly and monotonically between the plotted results. At the farthest downstream location (Fig. 8e and f), evidence of the lift generated by the foil is apparent in the non-uniformity of U, and the negative average value of V. Here, the vertical extent of the measurements reported in Figs. 6-8 hides the details of the near-foil boundary layer and wake flows that have thicknesses of order 0.01C. The next section presents measurements of the mean flow close to the foil surfaces.

3.4 Inner mean flow

This subsection covers the measured boundary layer and near-wake mean flow close to the foil's trailing edge. In this flow region, the LDV results are complemented with PIV results, for which more flow conditions were measured. Unfortunately, a systematic comparison of the PIV and LDV data revealed inconsistencies.

The foil and its mounting system were intended to produce two-dimensional flow over as much of the foil's span as possible. However, unrepeatable variation in the mean flow was measured with the PIV system, particularly at Re_C = 8M. The observed behavior is attributed primarily to uncontrolled variation with time and with spanwise location in the downstream location of suction side boundary layer transition. Evidence to this effect is found in the reduction or disappearance of these measurement variations at the highest and lowest Re_Cs. At the highest Re_Cs, suction side transition is believed to occur uniformly close to the foil's leading edge. At the lower Re_Cs, suction side transition occurs uniformly near 70% chord where the adverse pressure gradient first becomes steep (see Fig. 25). Unfortunately, foil surface imperfections or the accumulation of PIV seed may have been controlling factors for suction side boundary layer transition in the mid-range Re_C's of this study ($4M \leq Re_C \leq 17M$). Though the effect is small in the attached boundary layers, the resulting variation in suction side boundary layer separation appears to amplify the effect. Figure 9 shows the worst-case variations observed in the near-wake mean velocity profiles (Geomtery I at $Re_C = 8M$). The thicker wake profile in Fig. 9 is from the LDV measurements at 25% span. The thinner wake profile is from the PIV measurements at 36% span. The thinner PIV profile was never measured by the LDV system at this Re_C. In summary, some variation of the inner mean-flow profiles at the trailing edge was observed at 36%-span in the mid-range Re_Cs of this study. To address this, the data presented have been restricted to the LDV mean flow measurements made at the 25%-span location, and those PIV fields (measured at 36% span) that agree with these LDV measurements.

A measure of the viscous flow on the Geometry I foil's suction side was provided by measurements of U_t (= the surface-tangent mean velocity) made at x/C = 0.43 with a miniaturized one-component LDV mounted inside the foil (Fourguette et al. 2001). These measurements are plotted in Fig. 10 for Re_C = 8M, 17 M, 33M and 50M along with laminar and turbulent boundary layer profile fits. Following surface-aligned coordinates, h is the local surface normal coordinate and U_{te} is the surface-tangent mean velocity at the edge of the boundary layer ($h = \delta$) where δ is selected for a best fit for the boundary layer profile. Here, δ and other fitting parameters, C_f = skin friction coefficient and Π = Coles' wake parameter, are given in Table 3 for the Blasius profile fit at Re_C = 8M, and the Coles' profile fit (see White 1991),

$$U_t^+ = \frac{1}{\kappa}\ln h^+ + B + \frac{2\Pi}{\kappa}\frac{\sin^2(\pi h f/2\delta)}{\sin^2(\pi f/2)}, \qquad (1)$$

for the other Re_Cs. Here the usual definitions apply: $U_t^+ = (U_t/U_{te})\sqrt{2/C_f}$, $h^+ = hU_{te}\sqrt{C_f/2}/\nu$, $\kappa = 0.41$, $B = 5.5$, $\nu = 0.775\times10^{-6}$ m^2/s (at the average water temperature), $\delta = \delta_e$, and the f-parameter in (1) was set to unity. Neither a fully-laminar nor a fully-turbulent boundary layer profile could be successfully fit to the Re_C = 17M data which suggests a transitional boundary layer at this location and Re_C. These measurements indicate that suction side boundary layer transition: i) occurred downstream of x/C = 0.43 at Re_C = 8M, ii) was underway but incomplete x/C = 0.43 at Re_C = 17M, and iii) was complete upstream of x/C = 0.43 at Re_C = 33M. The load-bearing structure of the foil and the LCC precluded velocimetry at other mid-chord locations.

The next nearest downstream location at which boundary layer profiles could be measured was x/C = 0.930. Figure 11 shows the boundary layer U_t profiles for the suction side (a) and pressure side (b) at this location for the Geometry I hydrofoil. To present the data in surface-aligned coordinates, the suction side data measured in vertical profiles at x/C=0.930 and 0.953 have been interpolated to approximate the data along the surface normal at x/C=0.930. For Re_C=1.4M and 4M, data was not available at x/C=0.953, so the surface normal profile is estimated from the vertical profile using $y \approx h$. A zero velocity point has been added to each profile at the foil surface where neither PIV nor LDV measurements were possible. All the profiles represent turbulent boundary layers and their corresponding fitting parameters are provided in Tables 4 and 5 for the suction and pressure sides of the foil, respectively. Here, the *f*-parameter in (1) and the added degree of freedom provided by $\delta \neq \delta_e$ were used to enhance the smoothness of the profile fits. Also, a vertical coordinate shift within the uncertainty in the LDV's spatial reference was allowed to achieve B=5.0 simultaneously with a best fit to the linear-log region of the boundary layer profiles. Note that the approximation $y \approx h$ used for the low Re_C data is expected to have a small effect on the boundary layer fits. As a test case, the same approximation was applied to the Re_C=8M data, producing a 2% overstatement of Π and negligible effect on the other fitting parameters.

An overview of the mean flow fields near the Geometry I and II foil derived from the PIV measurements is provided in Figs. 12-14. The first two of these figures show multiple velocity profiles of U (Fig. 12a & 13a) and V (Fig. 12b & 13b) above and downstream of the foil, which is depicted on the left side of each panel. The gray vertical lines indicate the positions at which the profiles were measured. One or two horizontal arrows connects a given flow profile with its measurement location. A relative scale for the flow speeds is given at the lower left of each panel. The more nearly horizontal curves on each figure indicate the suction-side and pressure-side boundary layer thicknesses above and below the foil, and the boundaries of the foil's wake beyond x/C of unity. Excluding Re_C=4M, three general trends are observed: 1) the wake thins as Re_C increases, 2) the wake is thicker with Geometry II, and 3) the reverse flow region is longer with Geometry II. Interestingly, Geometry II at Re_C = 4M is the lone exception to all three of these trends. Figure 14 provides normalized U and V values for Geometry I (a) and Geometry II (b) at the boundary-layer and wake edges shown on Figs. 12 and 13. These velocities are used to normalize several of the following plots.

The PIV measurements near the trailing edge and Tecplot® 9.0 software were used to compute apparent stagnation points and separating streamlines. These are shown on Fig. 15 where arrows indicate flow direction and the interior of closed streamlines are shaded. The apparent stagnation point(s) are marked with black dots, and dashed lines represent streamlines that must exist but were either not resolved or not recorded within the PIV measurement suite. These streamline patterns are subject to uncertainty from the finite PIV accuracy and from weak, unintended (and unmeasured) spanwise flow, particularly in the recirculation region. In addition, streamlines under the foil could not be determined because shadowing prevented PIV measurements there.

Both geometry and Re-dependence is apparent in these streamline patterns, with Geometry I at $\mathrm{Re_C} = 1.4\mathrm{M}$ (Fig. 15a) providing the most unique case. Here, there is no indication of stagnation or separation at the trailing edge and the streamtube that emerges just below the foil appears to turn upwards without separating from the foil's trailing edge (a complete violation of the Kutta condition), and then flow backwards along the foil surface until it separates on the suction side. This places an apparent stagnation point just aft of the foil's trailing edge on the lower extent of a detached recirculation zone. However, the volume flux in this contorted streamtube lies at the confidence limits of the PIV measurements. It may be best described as speculative because weak spanwise flow gradients – normal to the PIV plane – might be holding this streamtube open and any spanwise gradient changes might close this streamtube in an orderly fashion. Nevertheless, the $\mathrm{Re_C} = 1.4\mathrm{M}$ case remains distinguished because the streamline flow-angle farther aft of the foil, which should be much less susceptible to unintended spanwise flow gradients, differs from that shown for the seven other panels of Fig. 15.

The remaining flow cases (Fig. 15b-15h) place a stagnation point at the trailing edge that captures the suction-side separating streamline and launches the dividing streamline into the wake. The suction-side separating streamline encloses a clockwise-rotating recirculation region. Secondary counterclockwise-rotating recirculation regions were found with Geometry II (Fig. 15b and 15d). For Geometry I, such counter-clockwise recirculating regions and associated stagnation points are absent or unresolved.

The location of suction side boundary layer separation was estimated from the data used to create Figs. 12 and 13 by two methods, and the results appear on Figure 16. In the first method, the loci of points at which $U_t = 0$ are plotted in surface-aligned coordinates. Excluding near-wall data contaminated by laser glare and downstream points for which the surface normal has extended into the wake, this loci of points closely approximates a straight line. Taking advantage of this linearity, the loci points for $x/C<0.998$ and over the ranges $0.0015< h/C < 0.0050$ and $0.0015< h/C < 0.0080$ for Geometries I and II, respectively, were linearly extrapolated to the surface. This surface point was taken as the zero-velocity separation point, x_{sep}^{U}. The second method is identical to the first, except that the plotted points are the loci of 50% probability of forward tangential velocity and the extrapolation produces x_{sep}^{γ}. These two methods would produce identical results in the case of a symmetric probability distribution function for the tangential velocity. However, the results on Fig. 16b show that x_{sep}^{U} is consistently larger than x_{sep}^{γ} by a small amount. On Fig. 16a two results are plotted for Geometry I at Re_C = 8M corresponding to the two trailing edge flow fields measured at this condition (see Fig. 9). The solid dark symbol is for the thicker wake that is consistent with the LDV measurements.

In Fig. 16a, the two trailing edge geometries show similar trends of suction side separation with Re_C for Re_C>3M. However, as Re_C decreases below 3M, suction side separation on Geometry I moves rapidly downstream, while separation on Geometry II is roughly constant. This behavior is attributed to differences in boundary layer separation on the pressure side. At the lowest Re_Cs, the pressure side boundary layer is laminar or transitional when it reaches the trailing edge, while the suction side boundary layer is turbulent. As these boundary layers evolve downstream and encounter an increasingly adverse pressure gradient at the trailing edge, the laminar pressure side boundary layer thickens more quickly than the turbulent suction side layer, and is believed to detach prior to the trailing edge. On Geometry I, the suction side boundary layer is then able to advance further downstream. The Geometry II edge sees a similar competition between its laminar pressure side and turbulent suction side boundary layers, but the steep trailing edge bevel prevents the suction side from advancing further downstream. As a result the pressure side boundary layer remains attached. Early pressure side separation on Geometry I provides an explanation not only for Fig. 16, but also for the unique appearance of panel (a) among the other panels of Fig. 15.

The evolution of the suction side boundary layer across separation for both trailing edges, is provided in Fig. 17 at x/C = 0.930, 0.979, 0.998, and 1.028 and Re_C = 1.4M, 4M, 8M and 50M. Here, the trailing edge coordinate frame (a fixed, rotated Cartesian coordinate system defined by h and t at 93% chord) is used to determine the U_t profiles at each x/C value. This coordinate system, which is rotated $\beta = 14.12°$ from the x-y system, was chosen because it approximates a streamline coordinate system for all flow conditions in the region 0.930<x/C<1.028. The U_t profiles are also vertically aligned to match at h_e, the location of the boundary-layer edge or near-wake edge in the 93%-chord Cartesian frame. The data show that the thinnest boundary layers occur at ReC = 4M, and that the outer part of the boundary layer flow evolves more rapidly at the lower two Re_Cs than at the higher two Re_Cs. In fact, at the higher two Re_Cs the outer part of the boundary layers (when normalized by the local external velocity) appears to be insensitive to the presence or absence of the foil surface. Under this velocity normalization and coordinate frame, the outer portion of the attached boundary layers crosses separation with little change, and the Re-dependence of the attached boundary layers sets the Re-dependence of the initial wake.

This geometry dependence is explored more fully on Fig. 18 which shows trailing edge profiles of U_t at Re_C = 1.4M, 4M, 17M, and 50M from the suction side at x/C=1.000 and the pressure side at x/C = 1.002. Here the suction side results are again plotted in the trailing edge coordinate frame, but the profiles are now vertically aligned by the h-coordinate of the foil surface at suction side separation, h_{sep}. The pressure side profiles simply present U plotted in the x-y coordinates frame. (On the pressure side $U = U_t$ and $y_{sep} = 0$, so Fig. 18 actually presents the pressure and suction side results on an equal footing.) The normalizing velocities can be derived from the data on Fig. 14. The three higher Re_Cs show good profile agreement on the pressure side and on the suction side for $h - h_{sep} > 0$. Thus, the main geometric effect of the trailing edge modification on the wake is communicated through the suction side separation point. The Re_C = 1.4M case does not fit this geometrical trend because the pressure side boundary layer separates prior to the trailing edge on Geometry I and at the trailing edge on Geometry II. Therefore a shift accounting only for suction side separation does collapse the geometry dependence.

The flow profiles that appear in Fig. 18 initiate the foil's wake. Figures 19, 20 and 21 show the subsequent flow evolution in x-y coordinates at x/C = 1.009, 1.028, and 1.047, respectively, for Re_C = 1.4M, 4M, 17M, and 50M. Here, the flow has been scaled as a plane wake; the horizontal axes are $\Delta U/\Delta U_{\max}$ where $\Delta U = U - U_e^{ss}$, and the vertical axes are $(y - y_{ctr})/y_{1/2}$ where y_{ctr} denotes the average of the vertical coordinates corresponding to $\Delta U = \Delta U_{\max}/2$, and $2y_{1/2}$ is the full wake width where $\Delta U = \Delta U_{\max}/2$. On each frame of Figs. 19-21 a Gaussian profile, matched at the half-width points, is plotted to indicate the extent of wake convergence to a standard symmetrical form. On Fig. 19 (x/C = 1.009), every profile shows some skewness as a remnant of the foil boundary layers' asymmetry, with Re_C = 4M being the most symmetrical. On Fig. 20 (x/C = 1.028), the profile skewness is reduced in every case and is nearly absent at Re_C = 4M. On Fig. 21, the various wakes have relaxed to a self-similar Gaussian profile and subsequent wake evolution involves little or no further profile shape changes.

Given the similarities shown on Figs. 19-21, wake flow differences can be readily assessed by examining how y_{ctr}, $\Delta U_{\max}$, and $y_{1/2}$ evolve downstream of the foil. The first of these is shown of Fig. 22 for where $(y_{ctr} - y^*)/C$ is plotted vs. x/C. Here, the value of y^* is the vertical increment obtained by extrapolating the foil thickness at suction side separation downstream to the trailing edge along a line parallel to the t-axis of the 93%-chord rotated Cartesian system: $y^* = \left(1.0 - x_{sep}^{U}/C\right)\tan\beta$. This vertical shift nearly collapses the wake center results for the two trailing edge shapes at each Re_C except for Re_C = 1.4M. This further confirms that the main impact of the differing trailing edges on the foil's mean flow can be accounted for with a vertical shift related to suction side separation. As mentioned earlier, the $\mathrm{Re_C}$ = 1.4M case involves early pressure side separation and a shift based on suction side separation is insufficient to collapse the geometry dependence.

The downstream evolution of the wake velocity deficit, $\Delta U_{\max}$, is shown in Fig. 23 for both trailing edges at $\mathrm{Re_C}$ = 1.4M, 4M, 17M, and 50M. As before, the normalizing velocity U_e^{ss} is extracted from the data on Fig. 14. The curves are downward trending as expected, and the strongest Reynolds number variation reveals a pairing of the two higher $\mathrm{Re_C}$ and the two lower $\mathrm{Re_C}$. Finally, the downstream evolution of the wake half width, $y_{1/2}$, is shown in Fig. 24 for both trailing edges and the same four $\mathrm{Re_C}$s. The curves are upward trending as expected, and there is substantial Reynolds number variation. In particular, at $\mathrm{Re_C}$ = 4M with Geometry II the wake leaves the trailing edge as the thinnest but by 10% of chord downstream it has become the thickest, and this growth rate is not matched nor exceeded by the flow at any other Reynolds number.

4. Discussion

The data presented above indicate that the flow near the trailing edge and in the near wake changes with both Reynolds number and trailing edge geometry. These changes can be related to the state of the suction and pressure side boundary layers upstream of the trailing edge separation. Here, a combination of laminar and turbulent boundary-layer integral calculations were used to infer transition location, shape factor $H = \delta^*/\theta$, and momentum thickness θ for the two boundary layers where direct measurements of these flow parameters were not possible. Here the usual definitions of δ^* and θ apply:

$$\delta^* = \int_{h=0}^{h=\delta_e} \left(1 - \frac{U_t}{U_{te}}\right) dy \text{ and } \theta = \int_{h=0}^{h=\delta_e} \frac{U_t}{U_{te}} \left(1 - \frac{U_t}{U_{te}}\right) dy. \qquad (2,3)$$

4.1 Boundary Layer Transition on the Hydrofoil

First, the averaged pressure distribution (average of all $\mathrm{Re_C}$s and geometries) on the hydrofoil and Thwaites' method (see White 1991) were used to compute the growth of the laminar boundary layer from the leading edge stagnation point to the region of boundary layer transition. The one-step method of Michel (1952, see White 1991) was then used to predict the location of boundary layer transition. The results of these calculations are depicted on Fig. 25 against the speed-averaged $-C_p$ curves. The calculated location of transition on both sides of the foil moves upstream with increasing $\mathrm{Re_C}$. For $\mathrm{Re_C}$ below 4M, the flow on the suction side is computed to remain laminar until the steep adverse pressure gradient beginning at x/C ~ 0.7. These calculations are confirmed, where data is available, by the LDV-measured velocity profiles from x/C = 0.43 (Fig. 10). These profiles suggest that transition moved upstream of x/C = 0.43 between Re_C of 8M and 17M.

4.2 Boundary Layers Approaching TE Region

The boundary layer parameters obtained from the Thwaites' method at the Michel-predicted transition point were employed as initial values for a turbulent boundary-layer integral calculation (White 1991). The momentum thickness was assumed continuous across the calculated transition point. Of course, actual boundary layer transition occurs over a finite region so the computed results obtained here are approximate in this regard. The turbulent boundary layer calculations were not used for the pressure side boundary layer below Re_C = 3M because the PIV results at x/C = 1 revealed a laminar or transitional boundary layer leaving the trailing edge on the pressure side. At these conditions, a transition location was not calculated, and Thwaites method was used exclusively.

A sample of the outcome of these calculations is shown on Fig. 26 where the predicted and measured suction- and pressure-side boundary-layer momentum thicknesses, θ, at x/C = 0.93 are plotted vs. Re_C for Geometry I. Considering the approximate nature of the analysis, the agreement between the calculations and measurements is good. For the suction side, the location of transition is roughly fixed at Re_C below 4M (see Fig. 28). As a result, as Re_C increases from the lowest values to Re_C=4M, θ decreases due to boundary layer thinning with increasing Re_C. However, as Re_C increases above 4M, the transition point begins to move upstream and increases the turbulent development length of the boundary layer. Thus, θ increases with increasing Re_C for Re_C> 4M. As a result, Re_C=4M produces a minima in the suction side boundary layer thickness. The Re-dependence of the pressure side boundary layer thickness is due to similar effects, but without a fixed transition point. In this case, Re_C=4M corresponds roughly to a maxima in the pressure side boundary layer thickness.

The success of these boundary layer calculations has implications concerning the Re and geometry dependence of the hydrofoil flow. Since the evolution of θ with increasing x/C is well predicted by a single C_P distribution, the Re and geometry dependence of the potential flow must have a weak influence on boundary layer development. This means that the upstream feedback from separation and the wake does not appreciably affect the state of the attached boundary layers. Instead, the character of these attached boundary layers is derived primarily from the Re-dependence of transition and its effect on the laminar and turbulent boundary layer development. This claim is made more significant by the finding of Fig. 17, which shows the Re-dependence of the outer portions of the attached boundary layers crossing separation with little change. This behavior, as well as other aspects of separation and the near wake will be discussed in the following section.

4.3 Separating Boundary Layers and Initial Wake

This section discusses the more complex Re and geometry dependence of the flow nearest to the trailing edge. In this region, the boundary layers at x/C = 0.93 further evolve to separate and form the near wake. On the suction side of the foil aft of x/C = 0.93, a steep adverse pressure gradient leads to boundary layer separation and the boundary-layer integral methods lose validity. However, suction side boundary layer integral quantities are still expected to exhibit some similarities. As discussed in Simpson (1989), boundary layers near separation exhibit a relationship between a simple function of the shape factor, $\tilde{h} = (H-1)/H$, and the ratio δ^*/δ_e . Figure 27 presents these two quantities for the separating suction side boundary layers on both trailing edges along with correlations developed from backward facing steps, $\tilde{h} = 1.5(\delta^*/\delta_e)$ and power-law profiles, $\tilde{h} = (2-\delta^*/\delta_e)^{-1}$ (see Simpson 1989). The intersection of these two correlations indicates the point of intermittent boundary layer detachment on a flat-plate. Here, H and δ^*/δ_e are computed from U_t in surface-aligned coordinates, and the data plotted range from $x^{\gamma}_{sep}/C - 0.004 \leq x/C \leq x^{\gamma}_{sep}/C + 0.011$ for Geometry I and $x^{\gamma}_{sep}/C - 0.003 \leq x/C \leq x^{\gamma}_{sep}/C + 0.003$ for Geometry II. The open symbols on Fig. 27a and the filled symbols on Fig. 27b for each flow condition correspond to the boundary layer state at 50% probability of forward flow.

For surfaces of low curvature and pressure gradient, the paths of the boundary layers in the vicinity of separation are roughly linear and collapse on the line of slope 1.5 indicated in Figure 27. Several of the data sets presented here have linear regions with this slope, but the overall collapse to a single line is imperfect, as might be expected for the curved-surface foil boundary-layer flows of this study. However, Fig. 27 does reveal a relationship between boundary layer integral quantities at separation, and demonstrates both $\mathrm{Re_C}$ and geometry dependence in the flow. The $\mathrm{Re_C}$-dependence is apparent in the variation between paths at different values of $\mathrm{Re_C}$. In particular the $\mathrm{Re_C}$ = 4M data generally lie above the plotted points for the other $\mathrm{Re_C}$s. Trailing-edge geometry dependence is apparent in the grouping of the data, with the Geometry I results (Fig. 27a) lying above the Geometry II results (Fig. 27b). This places the higher surface curvature results from Geometry II further from the flat plate results. The extreme case high surface curvature at separation is achieved by the foil's separating pressure side boundary layer where $H \approx 1.3$ (as expected, see Schlichting 1979).

The data presented in Fig. 17 also show that when a turbulent boundary layer separates from a rapidly curving surface, there is a lag in the communication of the near wall changes to the outer flow, a finding is similar to that of Morris and Foss (2001). In particular, above $\mathrm{Re}_C = 17\mathrm{M}$, the momentum-containing portions of the separated boundary layers at the trailing edge, x/C = 1.0 are essentially the same as the outer portions of the attached boundary layers at x/C ≈ 0.98 (when normalized by the local freestream). In addition, the trailing-edge geometry dependence of the suction-side boundary layer flow as it leaves the foil appears to be determined by the location of the suction side separation point for ReC ≥ 4M. In the trailing edge coordinate frame (93%-chord Cartesian coordinates), the suction-side U_t profiles for $(h - h_{sep})/C > 0$ are essentially identical between the two geometries, at least at the higher three Reynolds numbers, and the primary flow field variations are confined to $(h - h_{sep})/C < 0$ (Fig. 18).

On the pressure side of the foil beyond x/C = 0.93, the boundary layer development story is much simpler. Here, the pressure side boundary layers encounter a mildly-adverse pressure gradient as x/C increases toward unity. In the absence of this pressure gradient, separation is expected at the trailing edge. Pressure-side boundary layer profile measurements made for 0.93 ≤ x/C ≤ 1 are limited to Geometry I at Re_C of 8M, 17M, 33M, and 50M. Results for Geometry II at these Re_C values were expected to be nearly identical between geometries because of their similar static pressure distributions (see Figs. 3 and 4). All pressure-side velocity profiles are very similar to flat plate results, the displacement and momentum thickness vary according to established correlations, and skin friction coefficients inferred from the pressure side velocity profiles agree well with the Schultz-Grunow correlation (see Schlichting 1979). Although pressure side boundary layer profiles were not recorded for Re_C below 8M, the initial wake velocity profiles from x/C = 1.002 (Fig 18) retain the character of the pressure side boundary layer. With the exception of Geometry I at $\mathrm{Re}_C = 1.4\mathrm{M}$, these nearest-wake profiles suggest pressure-side boundary layer separation occurs at the trailing edge.

4.4 Development of the Wake

As the near-wake of the foil converts to a far-wake, its characteristics should trend toward those of an ideal two-dimensional wake with a constant momentum thickness. Here the momentum thickness, θ_w, of the foil's wake is defined by

$$\theta_w = \int_{y=-\delta_{e,ps}}^{y=\delta_{e,ss}} \frac{U(y)}{U_e}\left(1-\frac{U(y)}{U_e}\right)dy \tag{4}$$

where δ_e^{ps} and δ_e^{ss} are defined by the vertical locations where $U = U_e^{ss}$. The Geometry I LDV profiles on Fig. 8 were used to calculate an average momentum thickness for the far-wake at Re_C = 8M to 50M, $\theta_w/C \approx 0.0039$. Due to the difficulty in defining δ_e^{ps} and δ_e^{ss}, the uncertainty in θ_w is high and a Re-specific calculation is not justified. The wake-center velocity deficit, $\Delta U_{\max}$, and half-width $y_{1/2}$, were then estimated from the wake scaling laws in Sreenivasan and Narasimha (1982): $\Delta U_{\max}/U_o \approx 1.63[\theta/(x-x_o)]^{1/2}$ and $y_{1/2} \approx 0.30[(x-x_o)\theta]^{1/2}$, where x_o is a hypothetical origin of the wake. These scaling relationships are plotted on Figs. 23a and 24a, where x_o is selected for a best fit and is 1.01 for the scaling of $\Delta U_{\max}$ and 0.91 for the scaling of $y_{1/2}$. The same values for x_o and θ_w (we lack far wake data for Geometry II) are used to produce the curves on Figs. 23b and 24b. Although the match to the measured data is better for the wake velocity deficit $\Delta U_{\max}$, the wake scaling laws appear reasonably successful the higher Re_C flows beyond x/C = 1.03.

Overall, the foil's wake flow changes little from Re_C of 8M to 50M, but the findings at $Re_C \leq$ 4M show much more variability. For example, the wake profile at Re_C = 4M for both trailing edges relaxes to near-perfect Gaussian form closest to the trailing edge when compared to the wake profiles at the other Re_Cs (see Figs. 19 and 20). These observations suggest there is augmented turbulent transport occurring in the foil's near wake at Re_C = 4M. This contention is supported by the observation of vortex shedding fluctuations in the foil's near wake at this Re_C. Additional discussion of vortex shedding is deferred to a future paper on this topic.

4.5 Hydrofoil Lift and Drag

The overall suite of measurements is sufficient to allow the calculation of the foil's lift and drag by two nearly independent methods for Geometry I. With Geometry II, only one of these methods was viable. These calculations were undertaken to establish foil performance and to validate the internal consistency of the measurements made with Geometry I. Here, lift and drag are reported as the two-dimensional lift and drag coefficients (C_L and C_D) with the foil chord C used as the length scale in both cases.

The first method involved integrating the foil's surface stresses to determine foil lift and drag. The input data here were the splined pressure distributions and the skin-friction stress calculated from the boundary-layer integral analysis. From this method, C_L for Geometry I was determined to vary approximately linearly with Re_C from 0.52 to 0.55 ±0.01 for Re_C between 8M and 50M, and C_L for Geometry II was determined to be 0.52 ±0.01 and constant within the given uncertainty for the same range of Re_C. Here, C_D was found to be 0.006 ±0.001 and constant with Re_C within the given uncertainty for both trailing edge geometries. In all cases, approximately 60% of the total drag originated from skin friction, and 40% from pressure. The uncertainty in lift is derived from that of the static pressure measurements, discussed earlier. For the drag calculations, the dominant source of uncertainty is the skin friction values predicted using the boundary layer integral method. This uncertainty is estimated at +/-20% by comparing the predicted C_f values to those derived from the linear-log region of the measured velocity profiles at x/C = 0.93.

The second method employed a two-dimensional rectangular control volume enclosing the hydrofoil flow and defined by the corner coordinates (x/C, y/C) = (-1.25, -0.19), (-1.25, 0.26), (1.43, 0.26), and (1.43, -0.19). A uniform inflow velocity and the LDV far-wake survey data (Fig. 8) were used as velocity boundary conditions on the upstream and downstream control surfaces. Wall static pressure (Fig. 5) confirmed that the upstream pressure is uniform, but showed that the pressure in the far wake location was not. Therefore, the steady incompressible Bernoulli equation was used to provide the pressure on the downstream control surface, with the exception of the region of the wake where measured velocity fluctuations are substantial ($-0.07 < y/C < 0.05$). Here, linear interpolation between the Bernoulli-derived pressures was used. The splined test section wall static pressures, including the interpolated value on the suction side at x/C = 0.7 (Fig. 5), were used to provide the pressure boundary conditions on the upper and lower control surfaces. Again, the Bernoulli equation was utilized to determine flow velocity magnitudes along this surface. The assumed pure horizontal inflow direction, and the measured flow directions at the leading edge, at the trailing edge, and in the far wake were then linearly interpolated to provide a continuous estimate of the flow direction along the upper and lower control surfaces. Lift and drag contributions from turbulent fluxes were not included. These control volume calculations were undertaken for Re_C = 8M, 17M, 33M, and 50M. The imbalance in mass conservation over this range of Re_C, for the control volume described, was no greater than ±0.1% of the mass flux at the inflow surface. This result is sensitive to the interpolation scheme used to provide the flow direction on the upper and lower surfaces, as well as the calibration uncertainty in the LDV measurements.

From this second method, C_L for Geometry I was found to be 0.55 ±0.05, with Re_C variation falling within this larger uncertainty. The greatest source of this uncertainty is the interpolated value of the wall static pressure at x/C = 0.7 used on the upper control surface. Here, the foil's C_D was found to be 0.009 ±0.003, with Re_C variation again falling within the uncertainty. For the drag calculations, the greatest source of uncertainty is the +/-1% calibration uncertainty in the LDV, exacerbated by the use of separate LDV systems for the inflow and far wake data acquisition. The upper and lower control surface approximations have minimal effect on the drag calculations. Most significantly though, the two methods for calculating lift and drag coefficients for the Geometry I foil, produced results that agree within uncertainty.

5. Summary and Conclusions

The mean flow around a large, two-dimensional hydrofoil has been experimentally investigated with special attention given to the separated flow near its beveled trailing edge. Two trailing edge shapes were investigated that are of interest for practical applications. The data reported here are unique because of the high Reynolds numbers attained. This research effort leads to four conclusions.

First of all, over the range of chord-based Reynolds number from 1.4 to 50 million, and for the geometries tested, the Reynolds number and geometric dependencies of the flow field are mild but clearly measurable. The majority of the observed Reynolds number dependence comes for the development of the attached suction and pressure side boundary layers where the location of transition moves upstream with increasing Reynolds number. This dependence is characterized by a minima (maxima) near Re_C=4M in the variation with Re_C of the suction (pressure) side boundary layer momentum thickness. This distinguishes Re_C=4M as the test condition with the greatest symmetry between the suction and pressure side boundary layers. The characteristics of these boundary layers set the initial conditions for the wake development. This is particularly true in the outer part of the near wake where boundary layer properties persist beyond separation.

Second, much of the trailing-edge geometry dependence of the mean flow is a mere displacement of suction side boundary layer flow over the blunter trailing edge having the larger bevel angle (Geometry II). Here, boundary layer separation is moved aft compared to that on the thinner trailing edge (Geometry I), but the thicker trailing edge leads to a thicker near wake. In addition, when combined with prior flat plate measurements, the observed trends in turbulent boundary layer separation location show that the shape-factor at separation is lower on more highly curved surfaces.

Third, when the separated boundary layers pass the trailing edge and merge to form the foil's wake, they relax quickly with downstream distance to conform to classical wake scaling laws. However, the manner in which the wake develops depends on its initial thickness and symmetry. The most symmetric wake profile was found at $Re_C = 4M$ for both trailing edges. These flows are distinguished by the thin suction side boundary layers and thick pressure side boundary layers near the trailing edge that create the most symmetrical near wakes found in these studies. Interestingly, the most symmetrical near wake ($Re_C = 4M$, Geometry II) thickens the most rapidly. Fluctuating flow field results (not presented here) suggest near wake vortex shedding occurs to some degree for both trailing edges at $Re_C = 4M$, and that this phenomena drives the mean-flow development.

Thus, the final conclusion can be stated: the mechanism by which the initial wake profile shape, thickness, and symmetry determine the subsequent wake evolution is likely to be found in the flow's dynamic components.

The authors of this paper wish to the acknowledge the contributions of Shiyao Bian and Kent Pruss of the University of Michigan; William Blake, Michael Cutbirth, Ken Edens, Bob Etter, Ted Farabee, Jon Gershfeld, Joe Gorski, Tom Mathews, David Schwartzenberg, Jim Valentine, Phil Yarnall, Joel Park, and the LCC technical staff from the Naval Surface Warfare Center - Carderock Division; and Pat Purtell and Candace Wark from the Office of Naval Research. In addition, the authors wish to thank the Office of Naval Research for supporting this research effort under contract numbers N00014-99-1-0341, and N00014-99-1-0856.

REFERENCES

Bastedo, W.G., and Mueller, T.J. (1986) "Spanwise variation of laminar separation bubbles on wings at low Reynolds numbers," *AIAA Journal of Aircraft* **23**, 687-694.

Bearman, P.W. (1965) "Investigation of the flow behind a two-dimensional model with a blunt trailing edge fitted with splitter plates," *Journal of Fluid Mechanics* **21**, 241-255.

Benedict, R.P. (1984) *Fundamentals of Temperature, Pressure, and Flow Measurements* (Wiley, New York) pp. 340-349

Blake, W.K. (1975) "A statistical description of the pressure and velocity fields at the trailing edges of flat struts," David Taylor Naval Ship Research and Development Center Report No. 4241, Bethesda, Maryland.

Blake, W.K. (1986) *Mechanics of Flow Induced Sound and Vibration, Vol. 2* (Academic Press, Orlando), Ch. 11.

Blake, W.K., and Gershfeld, J.L. (1989) "Aeroacoustics of trailing edges," in *Frontiers in Fluid Mechanics* edited by M. Gad-el-Hak (Springer-Verlag, Berlin), pp. 457-532.

Bourgoyne, D.A., Ceccio, S.L., Dowling, D.R., Jessup, S., Park, J., Brewer, W., and Pankajakshan, R. (2001) "Hydrofoil Turbulent Boundary Layer Spearation at High Reynolds Numbers," *Proc. 23nd Symposium on Naval Hydrodynamics*, Val de Reuil, France.

Bourgoyne, D. A., Hamel, J. M., Judge, C. Q., Ceccio, S. L., Dowling, D. R., Cutbirth, J. M. (2002) "Hydrofoil Near-wake Strucutre and Dynamics at high Reynolds Number," *Proc. 24nd Symposium on Naval Hydrodynamics*, Fukuoka, Japan, .

Bourgoyne, D. A., Judge, C. Q., Hamel, J. M., Ceccio, S. L., and Dowling, D. R. (2001) "Lifting Surface Flow, Pressure, and Vibration at High Reynolds Number," *Proc. of the ASME International Mechanical Engineering Conf. and Exposition.*

Bearman, P. W. (1965) "Investigation of the flow behind a two-dimensional model with a blunt trailing edge and fitted with splitter plates, " Journal of Fluid Mechanics, **21**, 241-255.

Brodeur, R.R., and van Dam C.P. (2000) "Transition prediction for a two dimensional Navier-Stokes solver applied to wind-turbine airfoils," AIAA paper no. 2000-0047.

Covert, E.E. and Lorber P.F. (1982) "Unsteady turbulent boundary layers in adverse pressure gradients," AIAA paper no. 82-0966.

DeGraaff, D.B. and Eaton, J.K. (2000) "Reynolds-number scaling of the flat-plate turbulent boundary layer," *Journal of Fluid Mechanics* **422**, 319-346.

Deutsch, S. and Zierke, W.C. (1987) "The measurement of boundary layers on a compressor blade in cascade: Part 1 – A unique experimental facility," *ASME Journal of Turbomachinery* **109**, 520-526.

Deutsch, S. and Zierke, W.C. (1988a) "The measurement of boundary layers on a compressor blade in cascade: Part 2 – Suction surface boundary layers," *ASME Journal of Turbomachinery* **110**, 138-145.

Deutsch, S. and Zierke, W.C. (1988b) "The measurement of boundary layers on a compressor blade in cascade: Part 3 – Pressure surface boundary layers and the near wake," *ASME Journal of Turbomachinery* **110**, 146-152.

Etter, R.J, and M.B. Wilson (1992) "The Large Cavitation Channel," *Proc. the 23rd American Towing Tank Conf.*, New Orleans.

Fitzgerald, E.J., and Mueller, T.J. (1990) "Measurements in a separation bubble on an airfoil using laser velocimetry," *AIAA Journal* **28**, 584-592.

Fourguette, D., Modarass, D., Taugwalder, F., Wilson, D., Koochesfahani, M., and Gharib, M. (2001) "Miniature and MOEMS Flow Sensors," AIAA paper no. 2001-2982.

Halstead, D.E., Wisler, D.C., Okiishi, T.H., Walker, G.J., Hodson, H.P., and Shin, H.-W. (1997a) "Boundary layer development in axial compressors and turbines: Part 1 of 4 – Composite Picture," *ASME Journal of Turbomachinery* **119**, 114-127.

Halstead, D.E., Wisler, D.C., Okiishi, T.H., Walker, G.J., Hodson, H.P., and Shin, H.-W. (1997a) "Boundary layer development in axial compressors and turbines: Part 4 of 4 – Computations and Analyses," *ASME Journal of Turbomachinery* **119**, 128-139.

Ho, Y.-H., and Lakshminarayana, B. (1997) "Computation of unsteady flow field over a hydrofoil, including boundary layer and wake," *AIAA Journal* **35**, 40-50.

Howe, M.S. (1998) *Acoustics of Fluid-Structure Interactions* (Cambridge University Press, Cambridge, UK) Ch. 3.

Jessup, S. (1999) "Large Hydrofoil for ONR High Reynolds Number Turbulence BAA," private correspondence.

Kerwin, J.S. (1986) "Marine propellers," *Annual Review of Fluid Mechanics* **18**, 367-403.

Lurie, E.A., Keenan, D.P., and Kerwin, J.E. (1998) "Experimental study of an unsteady separating boundary layer," *AIAA Journal* **36**, 565-570.

Malick, M.R. (1997) "Boundary layer transition prediction toolkit," AIAA paper no. 97-1904.

Morris, S.C. and Foss, J. (2001) "Turbulent boundary layer to single stream shear layer," *Bulletin of the American Physical Society* **46**, No. 10, 134.

Michel, R. (1952) "Etude de la transition sur les profils d'aile-establissment d'un point de transition et calcul de la trainee de la profil incompressible," ONERA Report No. 1/1578A.

Österlund, J.M., Johansson, A.V., Nagib, H.M., and Hites, M.H. (2000) "A note on the overlap region in turbulent boundary layers," *Physics of Fluids* **12**, 1-4.

Park J. T., and Cutbirth J. M. (2002) Uncertainty in HIFOIL Experiments, private correspondence.

Schlichting, H. (1979) *Boundary-Layer Theory*, 7th *Ed.* (McGraw-Hill, New York), pp. 643, 674-675.

Simpson, R. L., (1989) "Turbulent boundary-layer separation," *Annual Review of Fluid Mechanics* **21**, 205-234.

Sreenivasan, K.R. and Narasimha, R. (1982) "Equilibrium parameters for two dimensional turbulent wakes," *Journal of Fluids Engineering* **104**, 167-170.

Thompson, B.E. and Whitelaw, J.H. (1985) "Characteristics of a trailing-edge flow with turbulent boundary-layer separation," *Journal of Fluid Mechanics* **157**, 305-326.

Ubaldi, M., Zunino, P., Campora, U., and Ghiglione, A. (1996) "Detailed velocity and turbulence measurements of the profile boundary layer in a large scale turbine cascade," ASME International Gas Turbine & Aerospace Congress and Exposition, Birmingham, UK, paper No. 96-GT-42.

Volino, R.J. and Hultgren, L.S. (2000) "Measurements in separated and transitional boundary layers under low-pressure turbine airfoil conditions," ASME International Gas Turbine & Aerospace Congress and Exposition, Munich, Germany, paper No. 2000-GT-260.

Wang, M. and Moin, P. (2000) "Computation of trailing-edge flow and noise using large-eddy simulation," *AIAA Journal* **38**, 2201-2209.

Wang, M. and Moin, P. (2002) "Dynamic wall modeling for large-eddy simulation of complex turbulent flows," *Physics of Fluids* **14**, 2043-2051.

White, F.M.,1991, *Viscous Fluid Flow, 2nd Ed.* (McGraw Hill, Inc., New York), pp. 268-273, 377, 419, 450-456.

Pressure Side	
Geometry I & II	
x/C	y/C
0.0000184001	0.0091713492
0.0000184286	0.0091517136
0.0000190302	0.0091053424
0.0000215040	0.0090297833
0.0000278123	0.0089299027
0.0000405062	0.0088065858
0.0000630757	0.0086600823
0.0000990404	0.0084947519
0.0001520273	0.0083100488
0.0002291967	0.0081084449
0.0003333222	0.0078917572
0.0004707003	0.0076617027
0.0006474672	0.0074202969
0.0008694072	0.0071690505
0.0011432333	0.0069097507
0.0014752094	0.0066440514
0.0018720600	0.0063735465
0.0023405001	0.0060997597
0.0028872245	0.0058241425
0.0035189406	0.0055480633
0.0042422387	0.0052728091
0.0050636007	0.0049995790
0.0059893413	0.0047294803
0.0070255441	0.0044635344
0.0081780673	0.0042026642
0.0094524527	0.0039477870
0.0108539362	0.0036994065
0.0123873022	0.0034584140
0.0140572719	0.0032252974
0.0158676670	0.0030005329
0.0178221095	0.0027845212
0.0199239942	0.0025775731
0.0221757605	0.0023799338
0.0245796602	0.0021917645
0.0271373673	0.0020131686
0.0298500220	0.0018441753
0.0327182534	0.0016847628
0.0357421467	0.0015348464
0.0389212723	0.0013942978
0.0422546591	0.0012629373
0.0457400309	0.0011405497
0.0493777799	0.0010268787
0.0531630190	0.0009216424
0.0570935427	0.0008245259
0.0611659106	0.0007351996
0.0653761759	0.0006533082
0.0697200197	0.0005784913
0.0741926295	0.0005103699
0.0787888898	0.0004485680
0.0835032224	0.0003926992
0.0883297937	0.0003423837
0.0932623030	0.0002972419
0.0982945191	0.0002569812
0.1034194695	0.0002209989
0.1086302163	0.0001891800
0.1139196257	0.0001611052
0.1192802763	0.0001364461
0.1247046799	0.0001140905
0.1301051932	0.0000961426
0.1357140373	0.0000799222
0.1412034522	0.0000659665
0.1468855318	0.0000540307
0.1525123959	0.0000438863
0.1581562006	0.0000353221
0.1638090347	0.0000281456
0.1694631070	0.0000221786
0.1751106917	0.0000172594
0.1807440766	0.0000132439
0.1863557201	0.0000099999
0.1919302003	0.0000074093
0.1974841601	0.0000053699
0.2029864402	0.0000037898
0.2084700738	0.0000025851
0.2140915629	0.0000016931
0.2200128866	0.0000010563
0.2263644996	0.0000006238
0.2330363429	0.0000003480
0.2396960040	0.0000001846
0.2460505579	0.0000000946
0.2510644031	0.0000000440
0.2571931922	0.0000000172
0.2622030032	0.0000000044
0.2673404655	0.0000000004
0.2725594320	0.0000000000
1.0000000000	0.0000000000

Suction Side	
Geometry I & II	
x/C	y/C
0.0000184001	0.0091713492
0.0000184363	0.0091855283
0.0000188251	0.0092184614
0.0000205916	0.0092850071
0.0000255665	0.0093826012
0.0000364715	0.0095115900
0.0000568765	0.0096744745
0.0000912594	0.0098724687
0.0001450470	0.0101071720
0.0002245654	0.0103803244
0.0003378734	0.0106936803
0.0004900040	0.0110487415
0.0006949000	0.0114474338
0.0009594439	0.0118913574
0.0012954203	0.0123821377
0.0017147298	0.0129213261
0.0022381126	0.0135103892
0.0028551612	0.0141506854
0.0036042784	0.0148434464
0.0044925642	0.0155897666
0.0055358629	0.0163905847
0.0067506362	0.0172466620
0.0081539874	0.0181585745
0.0097631846	0.0191267818
0.0115963953	0.0201512061
0.0136717823	0.0212320202
0.0160070865	0.0223680442
0.0186230559	0.0235611334
0.0215361295	0.0248080082
0.0247655215	0.0261086153
0.0283295153	0.0274614036
0.0322460523	0.0288640385
0.0365325959	0.0303169977
0.0412060217	0.0318157298
0.0462024935	0.0333585663
0.0517772976	0.0349427685
0.0577047328	0.0365652797
0.0640780043	0.0382228165
0.0709098767	0.0399117863
0.0782085221	0.0416283261
0.0859854507	0.0433683112
0.0942474131	0.0451273658
0.1030002385	0.0469008610
0.1122479579	0.0486839348
0.1219927697	0.0504715820
0.1322349584	0.0522582799
0.1429727268	0.0540387845
0.1542022959	0.0558073652
0.1659178250	0.0575582264
0.1781113631	0.0592854434
0.1907728279	0.0609829928
0.2038900958	0.0626447781
0.2174498198	0.0642646656
0.2314333026	0.0658365138
0.2458250339	0.0673542058
0.2606039936	0.0688116892
0.2757484845	0.0702030183
0.2912358113	0.0715223925
0.3070385683	0.0727642000
0.3231327106	0.0739230544
0.3394897810	0.0749938442
0.3560006467	0.0759717821
0.3720757176	0.0768524297
0.3898442446	0.0776317407
0.4069549006	0.0783061361
0.4241759211	0.0788724697
0.4414752449	0.0793280870
0.4588286743	0.0796710753
0.4761800915	0.0798995185
0.4935216873	0.0800100823
0.5108137185	0.0800012524
0.5280255140	0.0798746166
0.5451267971	0.0796373842
0.5620882184	0.0792885187
0.5788814451	0.0788276881
0.5954792520	0.0782552358
0.6118556661	0.0775721470
0.6279868861	0.0767800779
0.6438473185	0.0758813116
0.6594176718	0.0748787238
0.6746771121	0.0737757196
0.6896071540	0.0725761389
0.7041918228	0.0712841887
0.7184136688	0.0699042348
0.7322616796	0.0684400389
0.7457234202	0.0668987565
0.7587889535	0.0652812185
0.7714499499	0.0635912686
0.7836998347	0.0618347489
0.7955335498	0.0600083341
0.8069475446	0.0580665527
0.8179399878	0.0560642546
0.8285104802	0.0540345124
0.8386597277	0.0520017612
0.8483901650	0.0499831874
0.8577050638	0.0479915782
0.8666090179	0.0460372591
0.8751075763	0.0441287896
0.8832072964	0.0422729583
0.8909156404	0.0404751783
0.8982407983	0.0387398312
0.9051917471	0.0370701211
0.9117780359	0.0354684980
0.9180098084	0.0339365985
0.9238976421	0.0324752719
0.9294525061	0.0310847357

Geometry I	
x/C	y/C
0.9294525061	0.0310847357
0.9350000000	0.0296891000
0.9396087961	0.0285161951
0.9442334873	0.0273350187
0.9485715938	0.0262200201
0.9526350643	0.0251767732
0.9564357581	0.0241965263
0.9599854319	0.0232355260
0.9632957666	0.0222581740
0.9663703683	0.0212499624
0.9692446364	0.0202072319
0.9719850613	0.0191305694
0.9743730401	0.0180537323
0.9766569294	0.0169628359
0.9787679756	0.0158757401
0.9807163201	0.0148021500
0.9825117916	0.0137507090
0.9841638361	0.0127207364
0.9856815693	0.0117425347
0.9870737369	0.0107769129
0.9883407196	0.0098958616
0.9895145175	0.0090419434
0.9905787710	0.0082370483
0.9915407360	0.0074820817
0.9924313106	0.0067769713
0.9932330285	0.0061215404
0.9939600560	0.0055146117
0.9952130267	0.0044404077
0.9962327884	0.0035396253
0.9970567651	0.0027940329
0.9977176000	0.0021845494
0.9982435476	0.0016921275
0.9986588264	0.0012986822
0.9989840400	0.0009876963
0.9991184357	0.0000584542
1.0000000000	0.0000000000

Geometry II	
x/C	y/C
0.9294525061	0.0310847357
0.9350000000	0.0296891000
0.9700000000	0.0212235000
0.9713500000	0.0208920000
0.9721490000	0.0206919000
0.9729480000	0.0204896000
0.9737480000	0.0202840000
0.9745470000	0.0200773000
0.9753460000	0.0198667000
0.9761450000	0.0196527000
0.9769440000	0.0194349000
0.9777430000	0.0192132000
0.9785420000	0.0189872000
0.9793410000	0.0187566000
0.9801400000	0.0185210000
0.9814140000	0.0181320000
0.9827900000	0.0176730000
0.9837490000	0.0173065000
0.9847000000	0.0168890000
0.9862020000	0.0160670000
0.9873000000	0.0154230000
0.9888210000	0.0149330000
0.9890090000	0.0142190000
0.9897930000	0.0136390000
0.9906340000	0.0129510000
0.9913670000	0.0122110000
0.9920040000	0.0114850000
0.9925130000	0.0108540000
0.9936220000	0.0094390000
0.9940620000	0.0088400000
0.9944950000	0.0082530000
0.9955620000	0.0067331000
0.9966290000	0.0051300000
0.9977190000	0.0034623000
0.9988090000	0.0017970000
1.0000000000	0.0000000000

Appendix A. Hydrofoil geometry in chord-normalized coordinates with the vertex of the trailing edge apex angle defined as (x/C, y/C) = (1,0)

Table 1. Upstream flow velocities and nominal Re_C with symbol and line-types listed. In the figures of this paper, filled and open symbols correspond to trailing edge Geometry I and II, respectively.

Table 2. PIV and LDV velocity survey locations.

Table 3. Parameters of boundary layers near mid-chord (x/C=0.43) on the suction side of the hydrofoil with trailing edge Geometry I.

Table 4. Parameters of boundary layers approaching the trailing edge region (x/C=0.930) on the suction side of the hydrofoil with trailing edge Geometry I.

Table 5. Parameters of boundary layers approaching the trailing edge region (x/C=0.930) on the pressure side of the hydrofoil with trailing edge Geometry I.

Table 1

U_o m/s	Re_C millions	Symbol / Line-type
0.5	1.4	– – – – – ■ – – – – – –
1.5	4	———————▲———————
3.0	8	–·–·–·–▼·–·–·–·–
6.0	17	- - - - - - - - ▶ - - - - - - - -
12.0	33	··················◀··················
18.3	50	–··–··–●·–··–··–

Table 2

	Measurement Station	Extent of Measurements Streamwise, *x/C*	 Vertical, *y/C*	 Spanwise, *z/S*
1.	Inflow Plane	-2.3	$-0.20<y/C<0.28$	$0<z/S<0.5$
2.	Leading Edge	-0.014	$-0.20<y/C<0.28$	0.25
3.	Suction Side Boundary Layer near Mid-chord	origin at $x/C=0.43$	$0<h/C<0.01$	0.35
4.	Boundary Layer approaching Trailing Edge	0.93	$-0.20<y/C<0.28$	0.25
5.	PIV Field at Trailing Edge	$0.96<x/C<1.11$	$-0.025<y/C<0.030$	0.36
6.	Near Wake Plane	1.028	$-0.20<y/C<0.28$	$0<z/S<0.5$
7.	Far Wake	1.42	$-0.20<y/C<0.28$	0.25

Table 3

Re_C [millions]	U_o [m/s]	δ/C	U_{te}/U_o	C_f	Π
nominal	+/- 0.01	+/- 0.0001	+/- 0.01	+/- 0.0002	+/- 0.03
8	3.0	0.0007	1.25	0.0004	---
17	6.0	0.0022	1.26	0.0042	0.00
33	12.0	0.0025	1.27	0.0030	0.11
50	18.3	0.0030	1.27	0.0022	0.75

Table 4

Re_C [millions]	U_o [m/s]	δ/C	δ_e/δ	U_{te}/U_o	C_f	Π	f
nominal	+/- 0.01	+/- 0.0002	+/- 0.01	+/- 0.01	+/- 0.0002	+/- 0.03	
1.4	0.5	0.0103	1.13	1.12	0.0037	0.51	1.18
4	1.5	0.0072	1.28	1.12	0.0027	0.95	1.10
8	3.0	0.0103	1.18	1.10	0.0020	1.50	1.06
17	6.0	0.0113	1.11	1.10	0.0017	1.70	1.06
33	12.0	0.0113	1.11	1.10	0.0015	1.71	1.06
50	18.3	0.0113	1.08	1.10	0.0015	1.60	1.06

Table 5

Re_C [millions] nominal	U_o [m/s] +/- 0.01	δ/C +/- 0.0002	δ_e/δ +/- 0.01	U_{te}/U_o +/- 0.01	C_f +/- 0.0002	Π +/- 0.03	f
8	3.0	0.0140	1.00	0.96	0.0025	0.62	1.15
17	6.0	0.0140	1.00	0.96	0.0023	0.60	1.15
33	12.0	0.0140	1.00	0.96	0.0020	0.60	1.15
50	18.3	0.0140	1.00	0.96	0.0019	0.58	1.16

Figure Captions

Figure 1. The test section geometry and hydrofoil mounting location, shown in an elevation view looking spanwise and two section views looking downstream. All dimensions are in meters unless otherwise noted, and the test section dimensions are referenced to the inside surface. Optical access at the leading and trailing edges required omission of the wall faring fillet radii on the wall at z/S=0 in the ranges x/C<0.19 and x/C>0.87. This configuration is depicted in Section-A. The ends of the remaining length of wall faring were smoothly tapered.

Figure 2. (a)The cross section of the Geometry I hydrofoil with chord and max thickness indicated. The chord length given is the idealized value, measured to the vertex of the trailing edge apex angle. This point defines (x/C, y/C) = (1, 0) in the tunnel coordinate system, for which the x-axis is taken as the streamwise axis of the tunnel. Also depicted is the hydrofoil coordinate system, for which the t-axis is taken as the local surface tangent. (b)A detail of the Geometry I and II trailing edges. The 0.4-mm radius, applied to the trailing edge tip, is not depicted. The dashed line indicates the direction of the surface tangent at x/C=0.930.

Figure 3. The static pressure coefficient, C_p, on the hydrofoil surface and on the vertical centerline of the test section side walls (y/C=0.04) for Geometry I at Re_C of 4M, 17M, and 50M. The stagnation pressure (C_p =1.0) was measured at x/C=0 but is not shown. The insets present at greater scale the data near the leading and trailing edges. Within the trailing edge inset, the x/C at which the suction side bevel initiates is labeled, and the region of mean suction-side flow separation is indicated by a gray bar on the x/C axis. Symbols represent the measured static pressure. Lines represent a cubic spline of the measured values. The straight line near zero C_p connects the wall data at the beginning and end of the hydrofoil influence.

Figure 4. Static pressure coefficient, C_p, for the hydrofoil with the Geometry II trailing edge, in a format similar to that of Figure 3. Data at Re_C = 17M are not available on the test section walls and are replaced with data at Re_C = 8M. In the trailing edge inset panel, the data from Geometry I at Re_C=50M is also shown for comparison. Also indicated in the trailing edge inset panel is the streamwise extent of the smooth seam between the hydrofoil and trailing edge modification. The static pressure tap in this region does not have a square edge and therefore has higher uncertainty.

Figure 5. Static pressure coefficient, C_p, on the test section walls and ceiling, for the both trailing edges at Re_C of 4M and 50M, in a format similar to Figure 3. (a) Data from the test section ceiling, and (b) data from the sidewalls on the suction side (y/C=+0.26) and pressure side (y/C= -0.19) of the foil. Symbols plot measured values and the solid line splines the average of the plotted points. Hydrofoil mounting hardware prevented data collection on the sidewalls near midchord, and the suction side point at x/C=0.65 (denoted by '*') is the average of the measured value on the suction side foil surface and the test section ceiling at Re_C=50M. The straight line near zero C_p is taken from Figure 3, and connects the centerline wall data (y/C=0.04) at the beginning and end of the hydrofoil influence.

Figure 6. The flow near the leading edge (x/C = -0.014) of the Geometry I hydrofoil, presented as the (a)streamwise and (b)vertical components of the time-averaged velocity, normalized by the velocity far upstream, U_o. The dashed line indicates the location of the vertical tangent of the leading edge (y/C=0.009). Data is shown for Re_C=8M and 50M. Data for Re_C=17M and 33M are omitted for graphical clarity, but collapse with the data shown.

Figure 7. The boundary layer flow on Geometry I, presented in the same format as Figure 6, and measured at (a,b) x/C=0.930, (b,c) x/C=0.958, and (e,f) x/C=1.000. The location of the hydrofoil surface is indicated by the gray bar. A zero vertical velocity at the hydrofoil surface is assumed and plotted for clarity. Data are shown for Re_C=8M and 50M. Data for Re_C=17M and 33M are omitted for graphical clarity, but trend monotonically in U_o with the data shown.

Figure 8. The wake flow of Geometry I, presented in the same format as Figure 6, and measured at (a,b) x/C=1.028, (b,c) x/C=1.070, and (e,f) x/C=1.430. Data are shown for Re_C=8M and 50M. Data for Re_C=17M and 33M are omitted for graphical clarity, but collapse with the data shown.

Figure 9. The near wake flow of Geometry I at Re_C=8M, presented in the same format as Figure 6, and measured at x/C=1.009. Symbols are measured values: ▲, LDV at z/S=0.25; and ——△——, PIV at z/S=0.36. Though pressure side measurements agree within experimental uncertainty, suction side measurements differ. The disagreement is attributed to spanwise variation in the location of suction side boundary layer transition at this Re_C. The measurements are consistent with transition and separation occurring further upstream at z/S=0.25 than at z/S=0.36.

Figure 10. Component of the time-averaged velocity tangent to the surface at x/C=0.43 on the suction side of the Geometry I hydrofoil. Symbols are measured values and solid lines are fits through the data, using a laminar boundary layer profile for Re_C=8M, and a turbulent boundary layer profile (Equ. 1) for Re_C=17M, 33M, and 50M. At Re_C=17M, the turbulent profile with Coles parameter, Π=0, fits the data below h/C=0.006. The data above h/C=0.006 fit neither a laminar nor turbulent profile, but are traced with a solid gray line to improve graphical clarity. Table 3 provides the parameters used in the curve fits. All fits use κ=0.41, B=5.5, and $\nu=0.775\ \mathrm{x}10^{-6}\ \mathrm{m}^2/\mathrm{s}$.

Figure 11. Component of the time-averaged velocity tangent to the surface at x/C=0.930 on the (a) suction and (b) pressure side surfaces of the Geometry I hydrofoil. Symbols are measured values. Lines are curve fits using a turbulent boundary layer profile (as in Figure 10) with the fitting parameters provided in Tables 4 and 5. For graphical clarity, symbols are shown for only two Re_C. The data scatter at these Re_C is representative of that found at the other Re_C.

Figure 12. The separating boundary layers and near wake with Geometry I, presented as the (a)streamwise and (b)vertical components of the time-averaged velocity, normalized by the velocity far upstream, U_o. The trailing edge geometry is depicted on the left side of the frame and flow is from left to right. Vertical gray lines are shown at the x/C coordinate of the measurements and provide the axes upon which the velocity values are plotted as black lines. An arrow extends from each axis line to its associated velocity profile. The velocity profiles are plotted within the range $\delta_e^{ps} \le y \le \delta_e^{ss}$, and the field values of δ_e^{ss}/C and δ_e^{ps}/C are shown as thin black lines. The scale used to extract velocity values is provided in the bottom-left corner of the frame. Data at Re$_C$=1.4M was not available at the downstream station.

Figure 13. The separating boundary layers and near wake with Geometry II, presented in the format of Figure 12. Data at Re$_C$=50M was not available at the three upstream stations.

Figure 14. Streamwise and vertical components of velocity measured along the field values of δ_e^{ss}/C and δ_e^{ps}/C shown in Figures 12 and 13. Panels are for the (a) Geometry I and (b) Geometry II. Streamwise (vertical) values are read from the axes on the left (right) edge of the panels. Line type indicates Re$_C$.

Figure 15. Stagnation and separation points and the associated streamlines, derived from the time-averaged velocity fields of the (a-d) Geometry I and (e-h) Geometry II. (a,e)Re$_C$=1.4M. (b,f)Re$_C$=4M. (c,g)Re$_C$=17M. (d,h)Re$_C$=50M. Separation points are from Figure 16a. Stagnation points are those coordinates at which (U,V)=(0,0). Note that the spanwise velocity was not measured, but is assumed negligible based on two-dimensionality. Closed streamlines are filled with gray. Dashed lines indicate sections of streamlines which must exist but are not resolved. The dash-dot line in the upper right corner of each panel runs parallel to the surface tangent at x/C=0.930. Note that for all conditions and geometry, this line approximates the direction of the streamlines for 0.93<x/C<1.03. No data are available for x/C<0.993 at Re$_C$=50M for Geometry II.

Figure 16. The location of separation for both trailing edges at varying Re$_C$., based on PIV and LDV velocity measurements. Separation was located using two methods: by inflection of the profile of the time-averaged velocity tangent to the surface, U_t, and by probability of forward flow, γ, equal to 50%, where 'forward' is defined by the direction of the surface tangent. Provided are (a) results from the first method and (b) the difference of the two methods. ●, Geometry I; ○, Geometry II; ◔, Separation at Re$_C$=8M for Geometry I with delayed suction side boundary layer transition, discussed in Section 3.4.

Figure 17. The time-averaged velocity profiles across separation, at varying Re$_C$ for both trailing edges. The profiles are presented in a rotated Cartesian coordinate frame aligned to the surface tangent at x/C=0.930. To best collapse the profiles, the spatial coordinate has been shifted by the boundary layer thickness, δ_e^{ss}, measured in the rotated frame and designated h_e. Presented are measurements at (a)Re$_C$=1.4M, (b)Re$_C$=4M, (c)Re$_C$=17M, and (d)Re$_C$=50M. Closed symbols are for Geometry I, while open symbols are for Geometry II at varying x/C: ■, x/C=0.930; ▲, x/C=0.979; ▼, x/C=0.998; ●, x/C=1.028. No data are available for x/C=0.979 at Re$_C$=50M for Geometry II.

Figure 18. The time-averaged velocity profiles for both trailing edges at varying Re_C. Suction side data are from x/C=1. Due to the shadow of the foil, pressure side data was not available at this coordinate, and so data at x/C=1.002 are presented. The suction (pressure) side data are presented in a rotated Cartesian coordinate frame, aligned to the suction (pressure) side surface tangent at x/C=0.930. To best collapse the geometry dependence of the flow, the spatial coordinate of the suction side data is shifted by the thickness of the trailing edge at the separation point, measured in the rotated frame and designated h_{sep}. No shift is applied to the pressure side data. Presented are measurements at (a)Re_C=1.4M, (b)Re_C=4M, (c)Re_C=17M, and (d)Re_C=50M. Closed symbols are for Geometry I, while open symbols are for Geometry II. Data at Re_C=50M for Geometry I is incomplete due to shadowing, but by all indications collapses with the data from Geometry II.

Figure 19. Time-averaged streamwise velocity profiles at x/C=1.0094, for the both trailing edges. Panel show results at (a) Re_C=1.4M, (b)Re_C=4M , (c)Re_C=17M, and (d)Re_C=50M. Symbols give measured values and the dashed line gives the Gaussian fit matched at the half-width points. Closed symbols are for Geometry I, while open symbols are for Geometry II.

Figure 20. Time-averaged streamwise velocity profiles at x/C=1.0281, for both trailing edges, in the format of Figure 19.

Figure 21. Time-averaged streamwise velocity profiles at x/C=1.0469, for both trailing edges at Re_C=1.4M, 4M , 17M, and 50M. Symbols give measured values and the solid line gives a Gaussian fit. Closed symbols are for Geometry I, while open symbols are for Geometry II

Figure 22. The wake profile center coordinate, y_{ctr}/C, used in Figures 19-21 and plotted against x/C for varying Re_C for both trailing edges. For all Re_C shown except 1.4M, a collapse of the geometry-dependence of this parameter is achieved by shifting y_{ctr} by an amount, y^*, derived from the hydrofoil thickness at the separation point. The lack of collapse at Re_C=1.4M is due to the variation with geometry of pressure side separation. Closed symbols are for Geometry I, while open symbols are for Geometry II.

Figure 23. The wake velocity deficit used in Figures 19-21, plotted against x/C for varying Re_C and for (a) Geometry I and (b) Geometry II. The black lines are polynomial fits of the measured values. The solid gray line is the wake scaling law of Sreenivasan and Narasimha (1982), using the momentum thickness of the far wake and x/C=1.01 as the hypothetical origin of the wake.

Figure 24. The wake half width used in Figures 19-21, plotted against x/C for varying Re_C and for (a) Geometry I and (b) Geometry II. The black lines are polynomial fits of the measured values. The solid gray line is the wake scaling law of Sreenivasan and Narasimha (1982), using the momentum thickness of the far wake and x/C=0.97 as the hypothetical origin of the wake.

Figure 25. Location of boundary layer transition, predicted from the mean C_p curve using Thwaites' method and the one-step method of Michel (1952). ○, measured C_p value; ———, spline of C_p values; △, predicted transition location at the Re_C (in millions) indicated.

Figure 26. Measured and predicted boundary layer momentum thickness, θ, at varying Re_C. (a)Thickness of the suction side boundary layers for Geometry I at x/C=0.930, shown in Figure 10. (b)Thickness of the pressure side boundary layers for both trailing edges at x/C=1. Where available (Geometry I, Re_C of 8M and above), the values are computed from LDV measurements at x/C=1. Otherwise, the values are computed from the wake data at x/C=1.002 shown in Figure 18; ●, computed from data from Geometry I; ○, computed from data from Geometry II; ———, prediction from the boundary layer integral methods.

Figure 27. Boundary layer parameters associated with separation for (a) Geometry I and (b) Geometry II at varying Re_C. Symbols give the boundary layer state derived from PIV measurements. The boundary layer state at the separation point (from Figure 16a) is plotted as a symbol with inverse fill. Lines provide the fits (see Simpson 1989): — — , correlation for boundary layers separating from flat plates and steps; — · · –, probability of forward flow, $\gamma = 0.8$ on flat plates and steps.

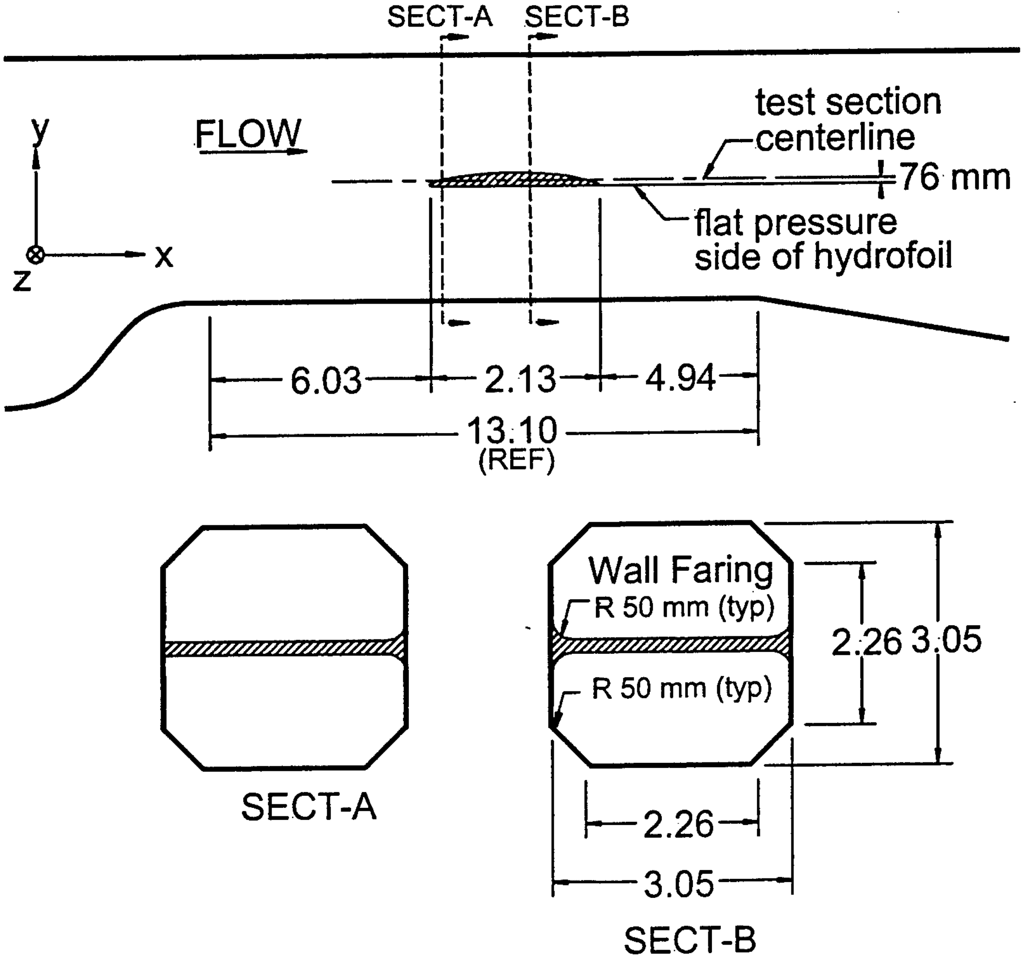

SECT-A
SECT-B
test section
centerline
y
FLOW
76 mm
flat pressure
side of hydrofoil
x
z
6.03
2.13
4.94
13.10
(REF)
Wall Faring
R 50 mm (typ)
R 50 mm (typ)
2.26
3.05
SECT-A
2.26
3.05
SECT-B

Fig. 1

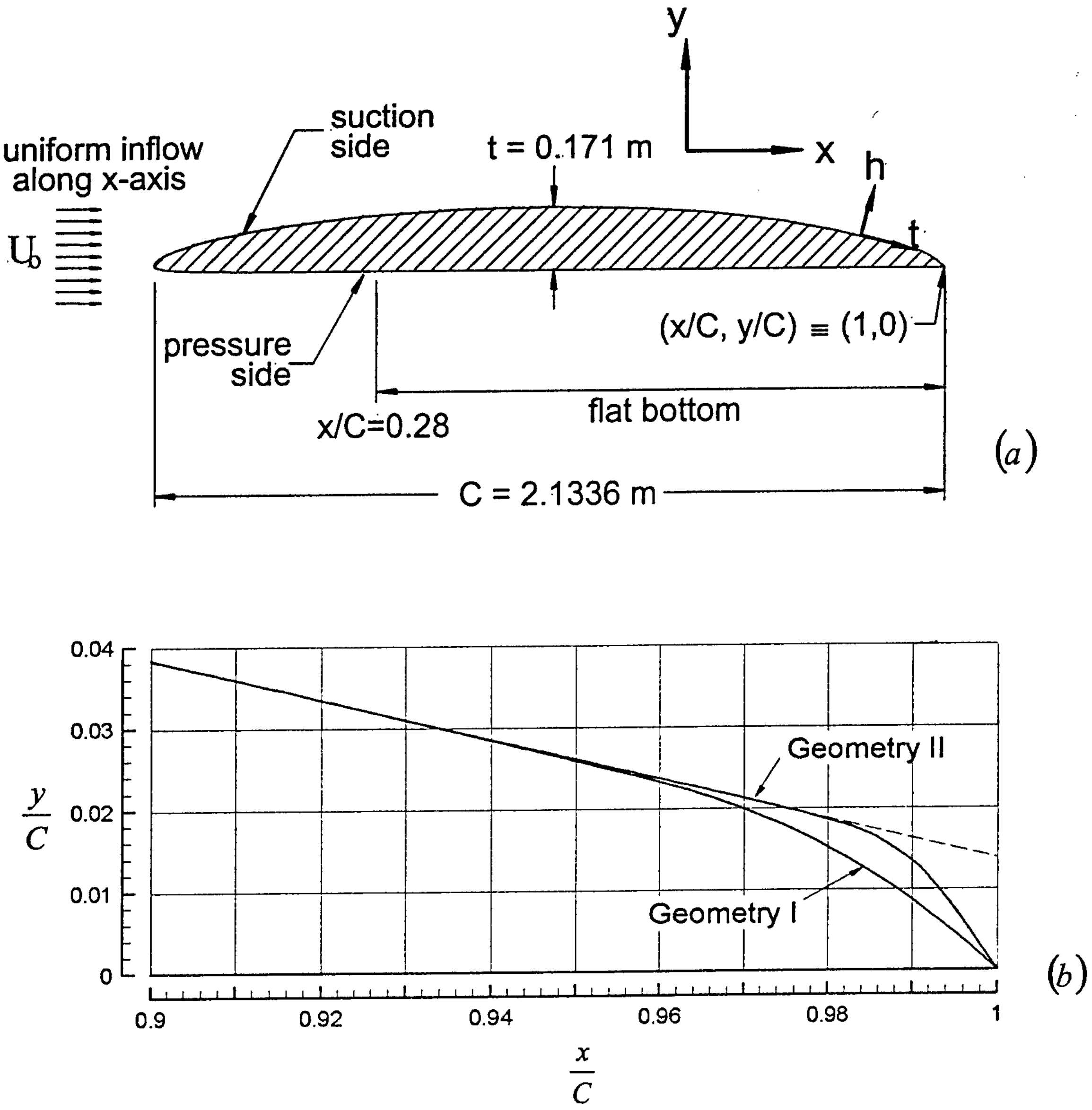
y
x
h
t
suction side
uniform inflow along x-axis
U_0
t = 0.171 m
pressure side
(x/C, y/C) ≡ (1,0)
x/C=0.28
flat bottom
C = 2.1336 m
(a)
0.04
0.03
0.02
0.01
0
$\frac{y}{C}$
Geometry II
Geometry I
0.9
0.92
0.94
0.96
0.98
1
$\frac{x}{C}$
(b)

Fig. 2

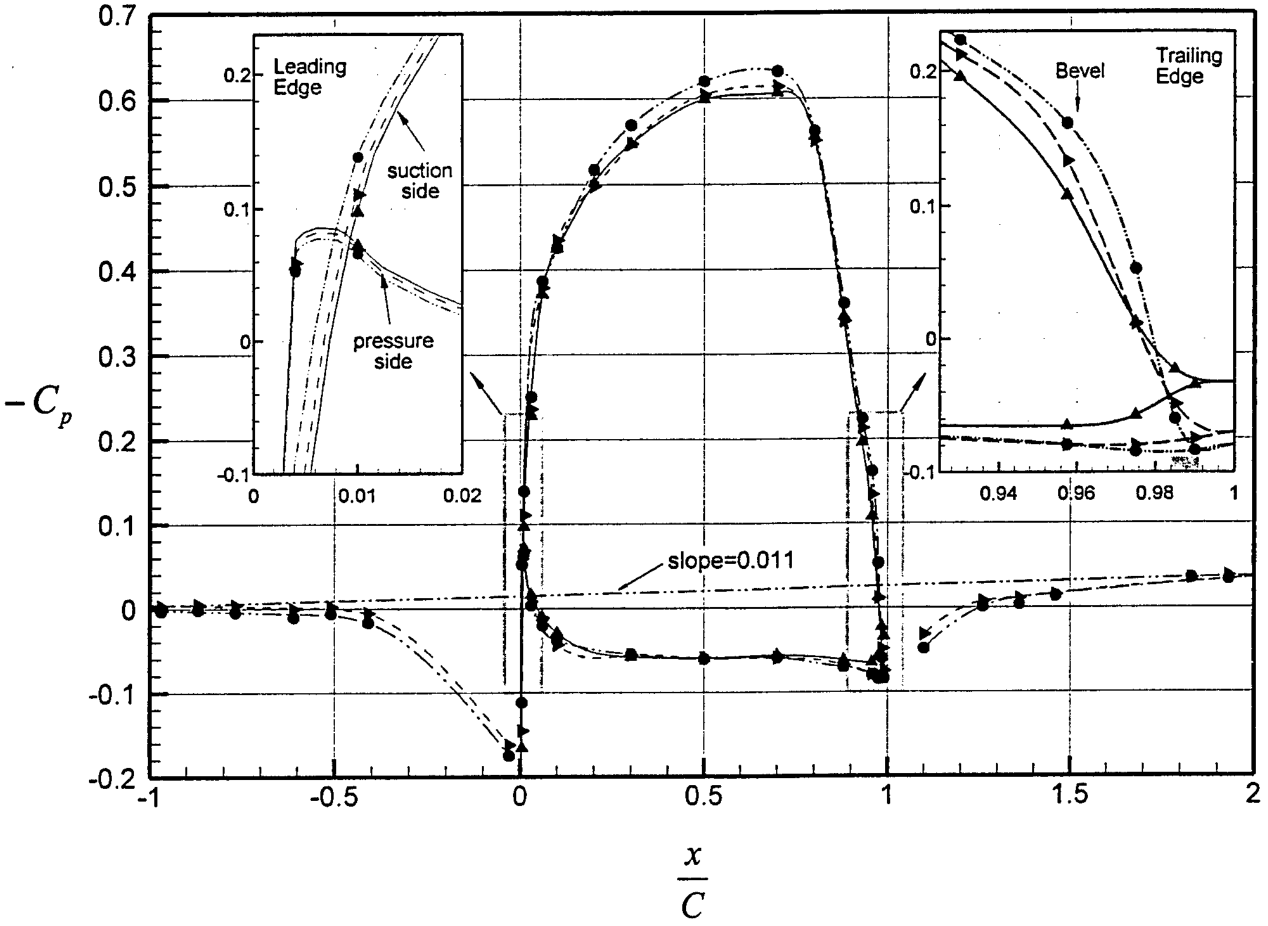
0.7
0.6
0.5
0.4
0.3
0.2
0.1
0
-0.1
-0.2
$-C_p$
-1
-0.5
0
0.5
1
1.5
2
$\frac{x}{C}$
slope=0.011
Leading Edge
suction side
pressure side
0.2
0.1
0
-0.1
0
0.01
0.02
Bevel
Trailing Edge
0.2
0.1
0
-0.1
0.94
0.96
0.98
1

Fig. 3

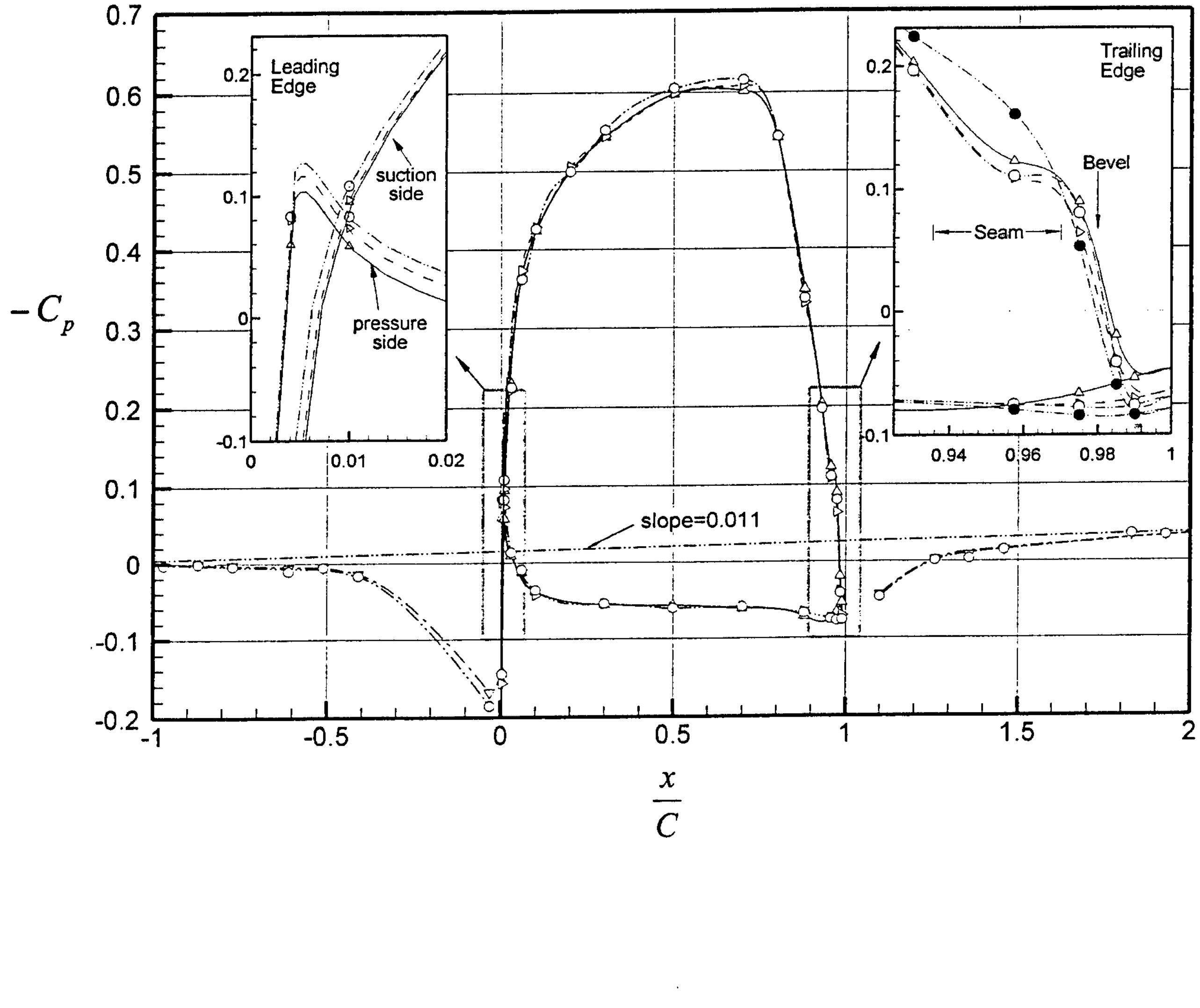

0.7
0.6
0.5
0.4
0.3
0.2
0.1
0
-0.1
-0.2
$-C_p$
-1
-0.5
0
0.5
1
1.5
2
$\frac{x}{C}$
slope=0.011
Leading Edge
suction side
pressure side
0.2
0.1
0
-0.1
0
0.01
0.02
Trailing Edge
Bevel
Seam
0.2
0.1
0
-0.1
0.94
0.96
0.98
1

Fig. 4

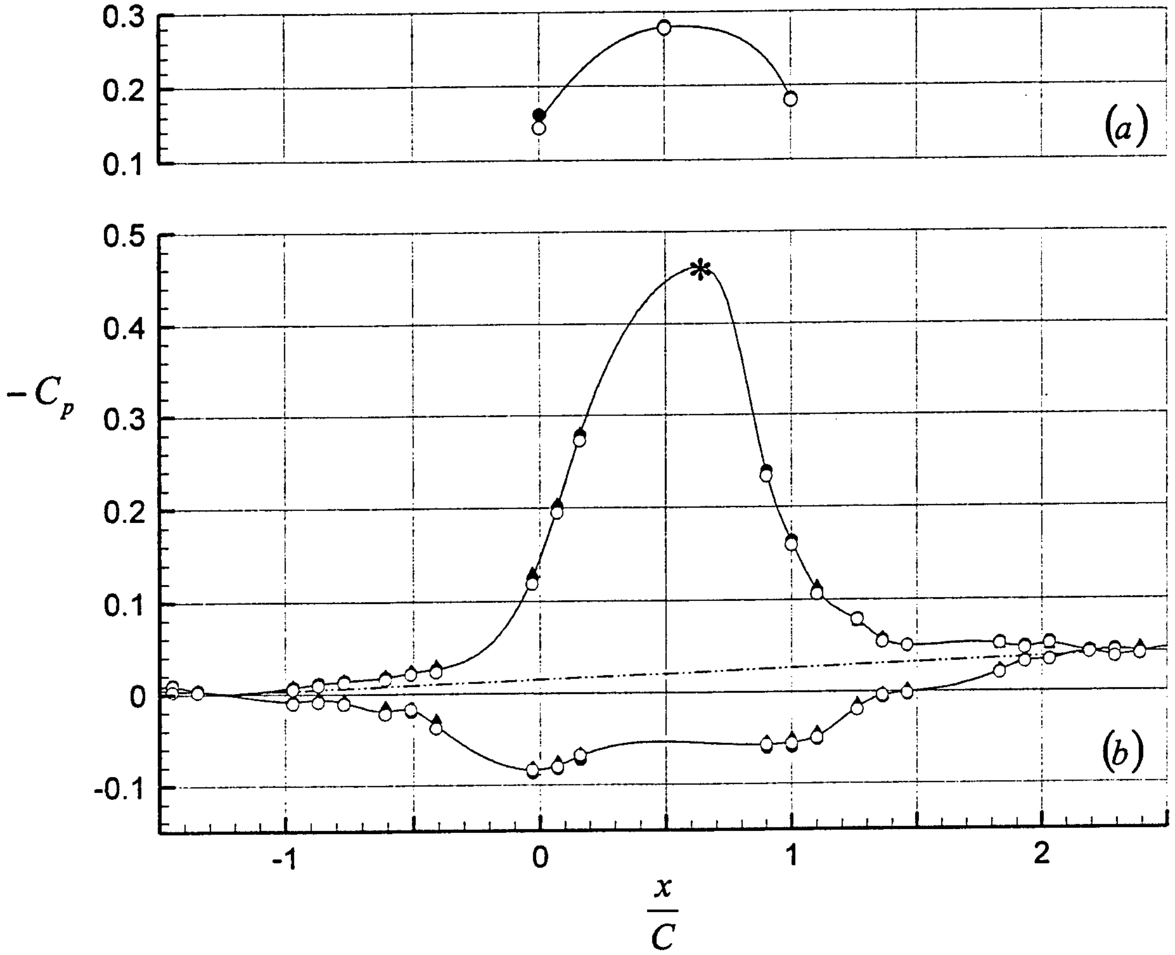

Fig. 5

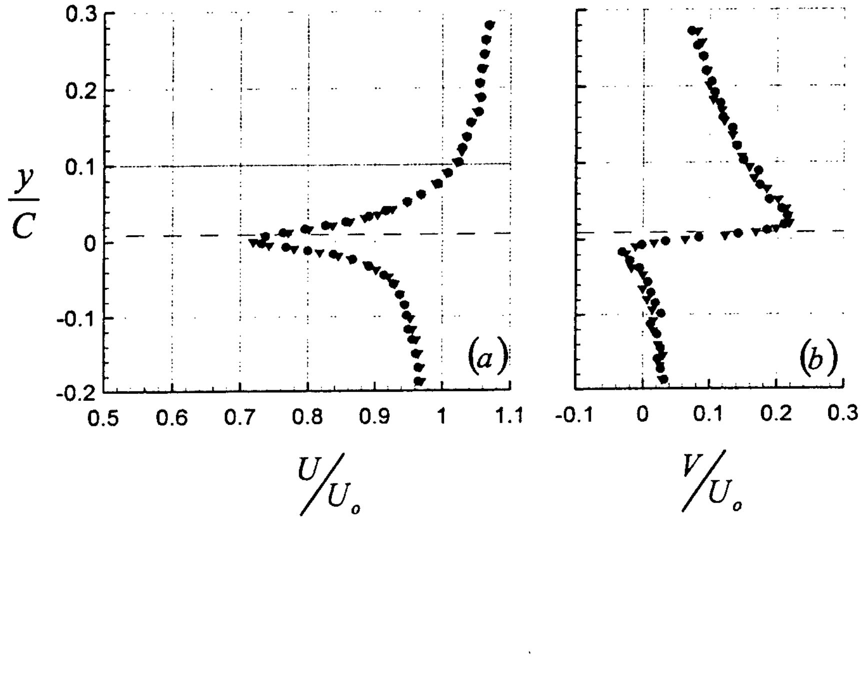

Fig. 6

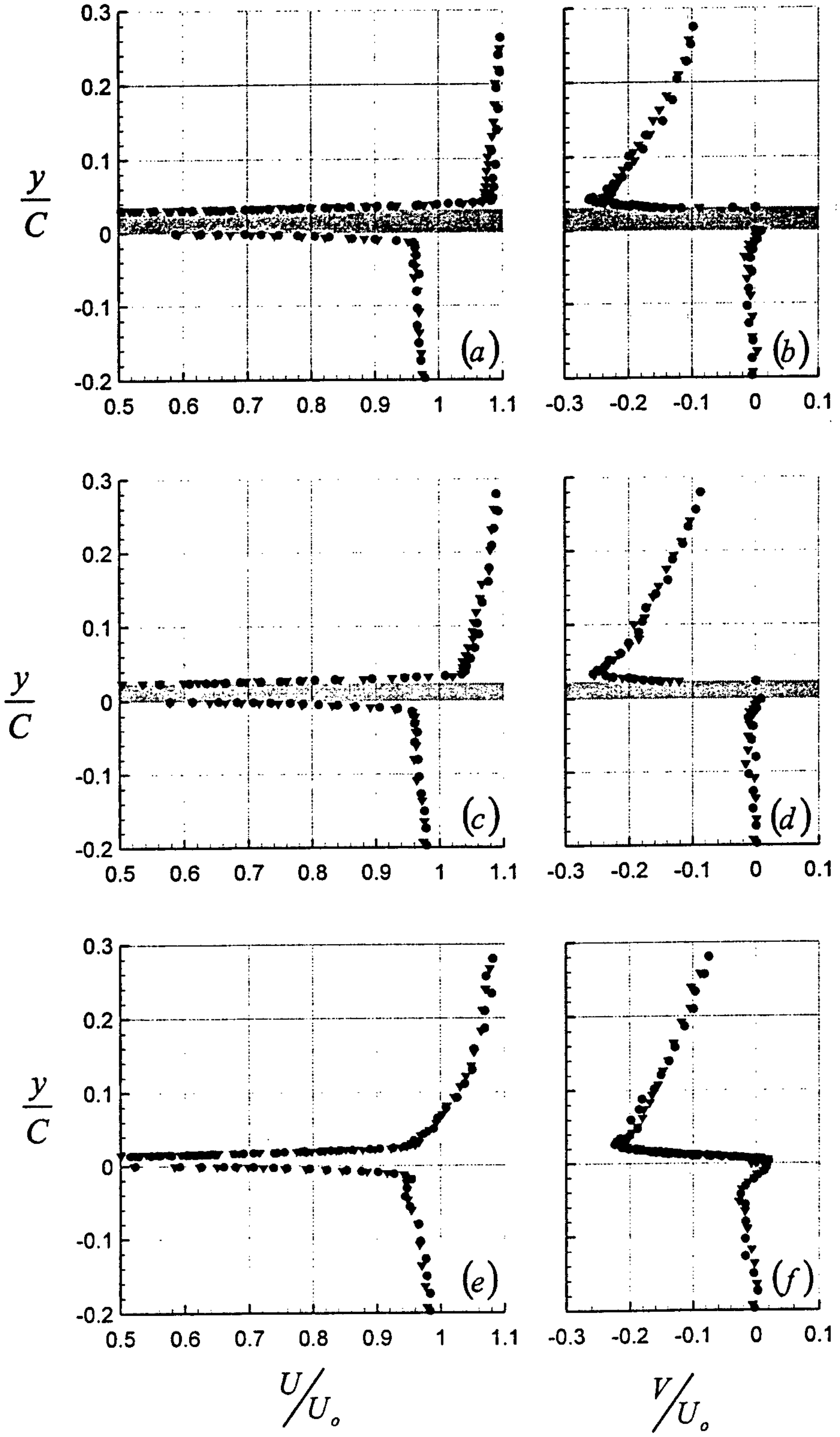

Fig. 7

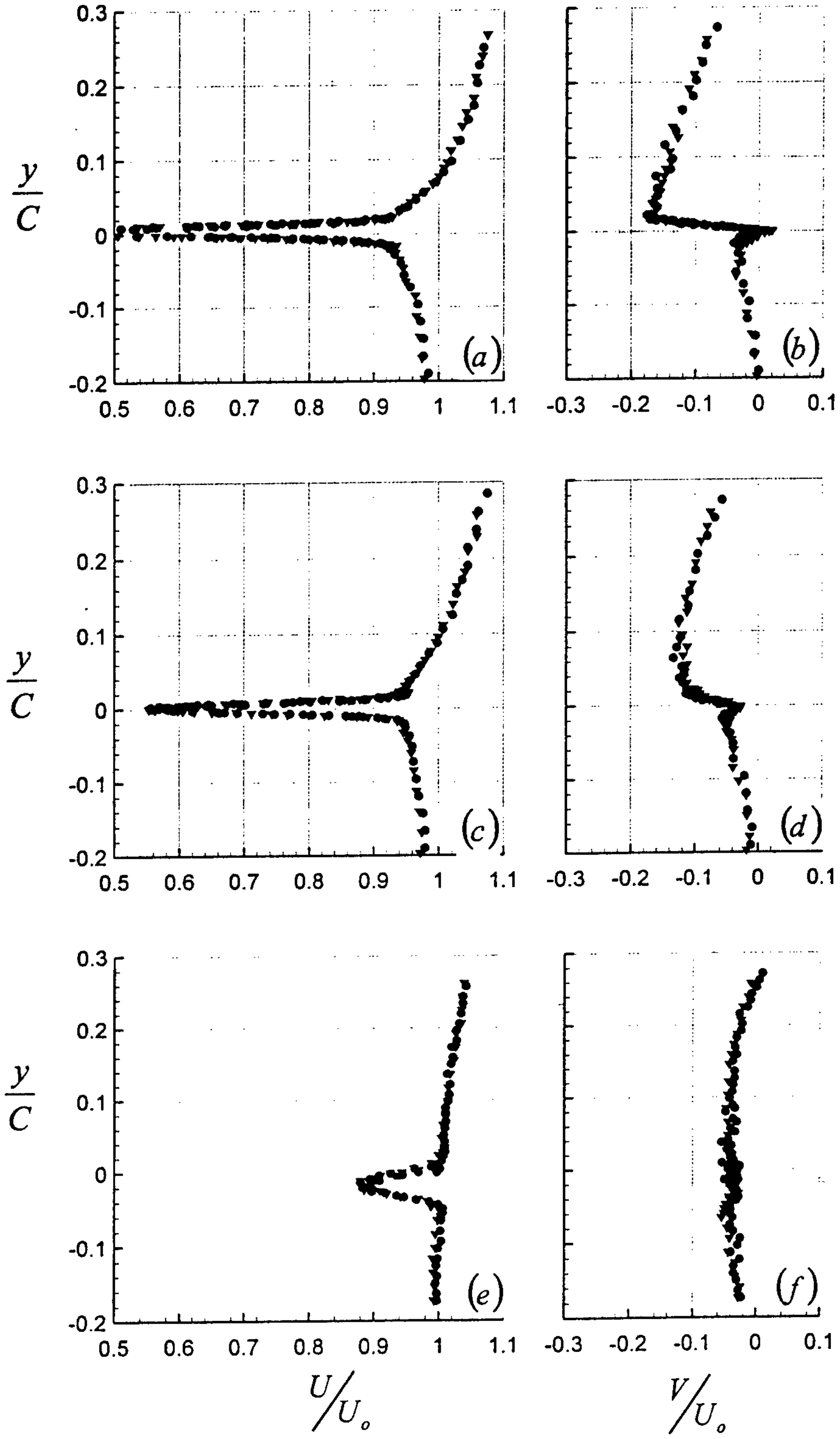

Fig. 8

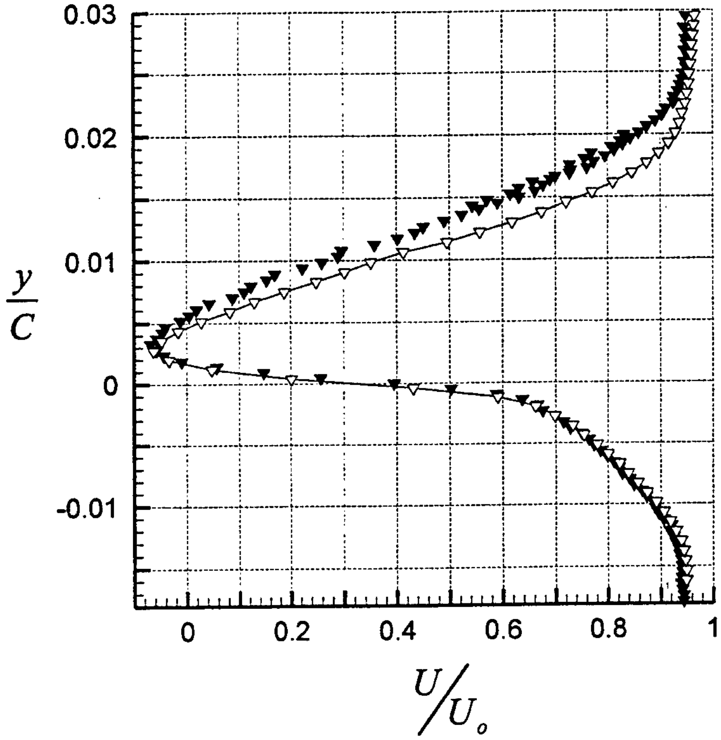

Fig. 9

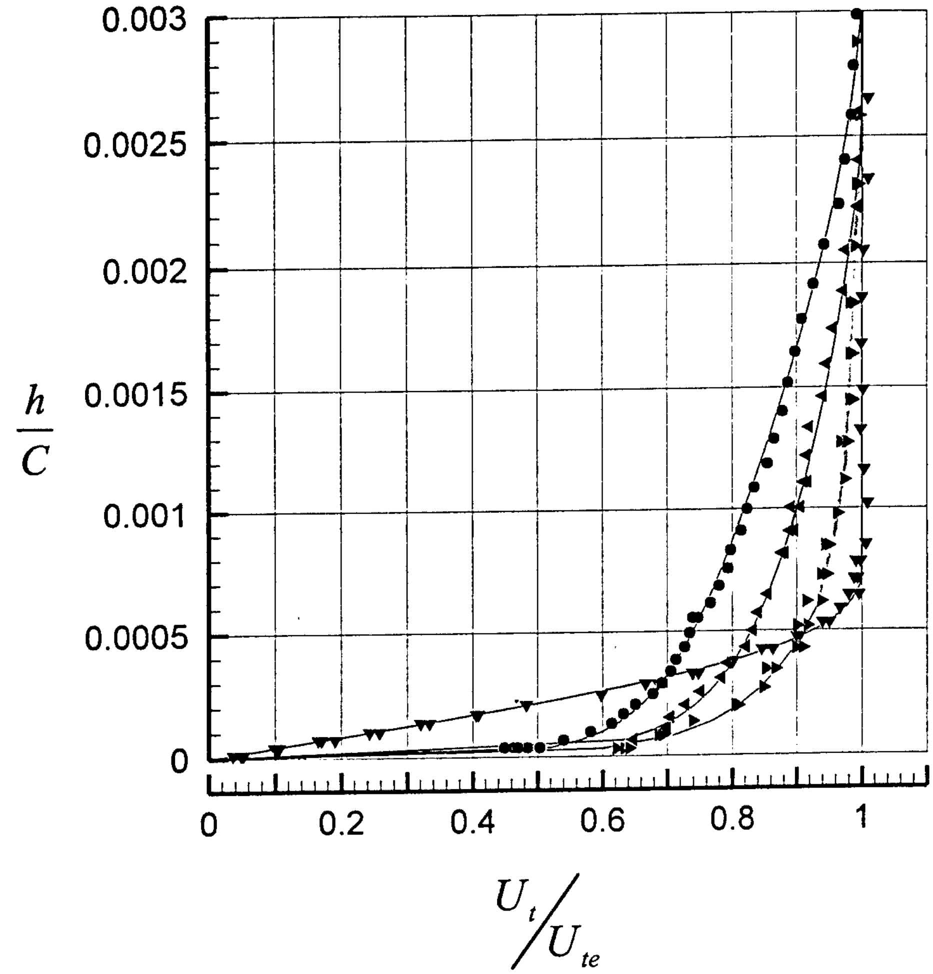

Fig. 10

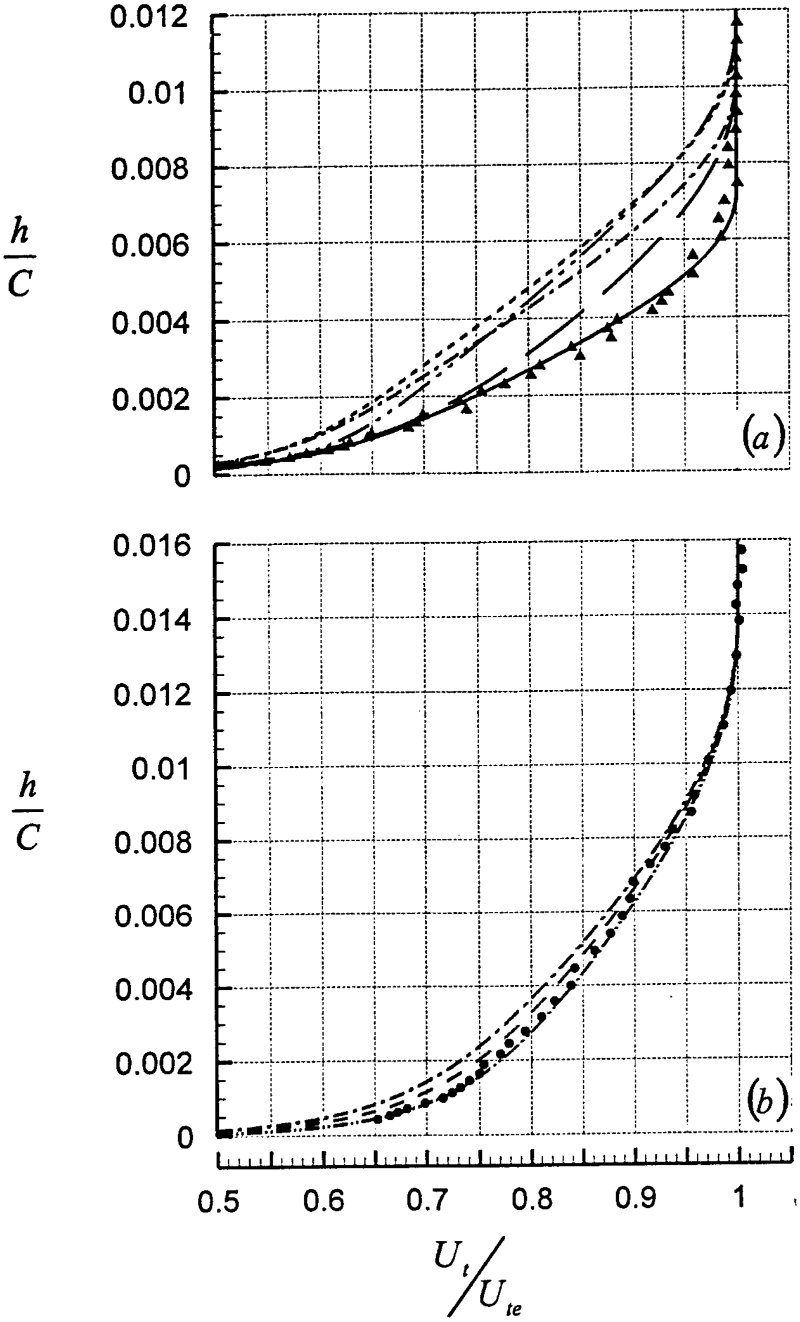
0.012
0.01
0.008
0.006
0.004
0.002
0
h/C
(a)
0.016
0.014
0.012
0.01
0.008
0.006
0.004
0.002
0
h/C
(b)
0.5
0.6
0.7
0.8
0.9
1
U_t/U_te

Fig. 11

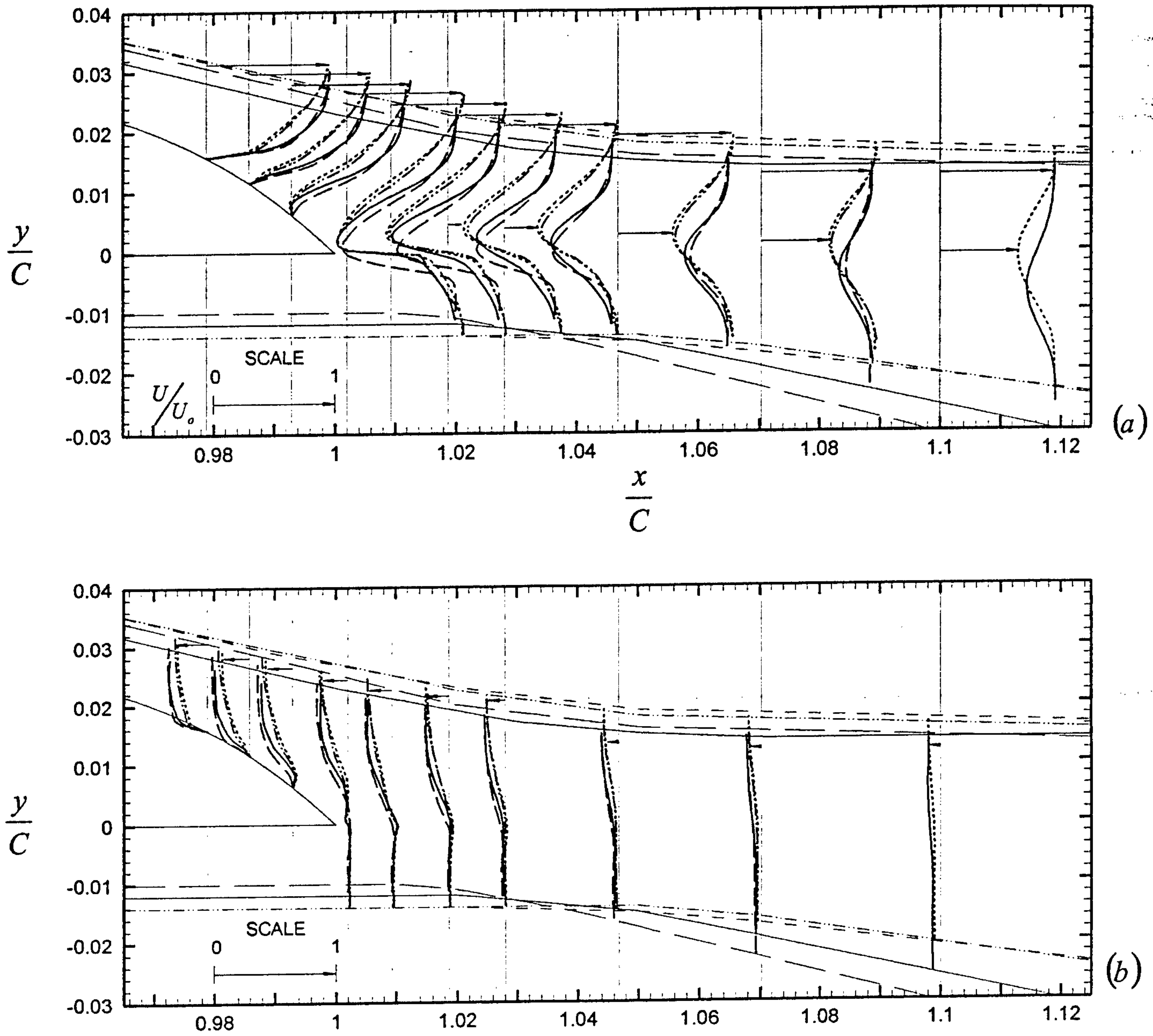
0.04
0.03
0.02
0.01
0
-0.01
-0.02
-0.03
y/C
SCALE
0
1
U/U_o
0.98
1
1.02
1.04
1.06
1.08
1.1
1.12
x/C
(a)
(b)

Fig, 12

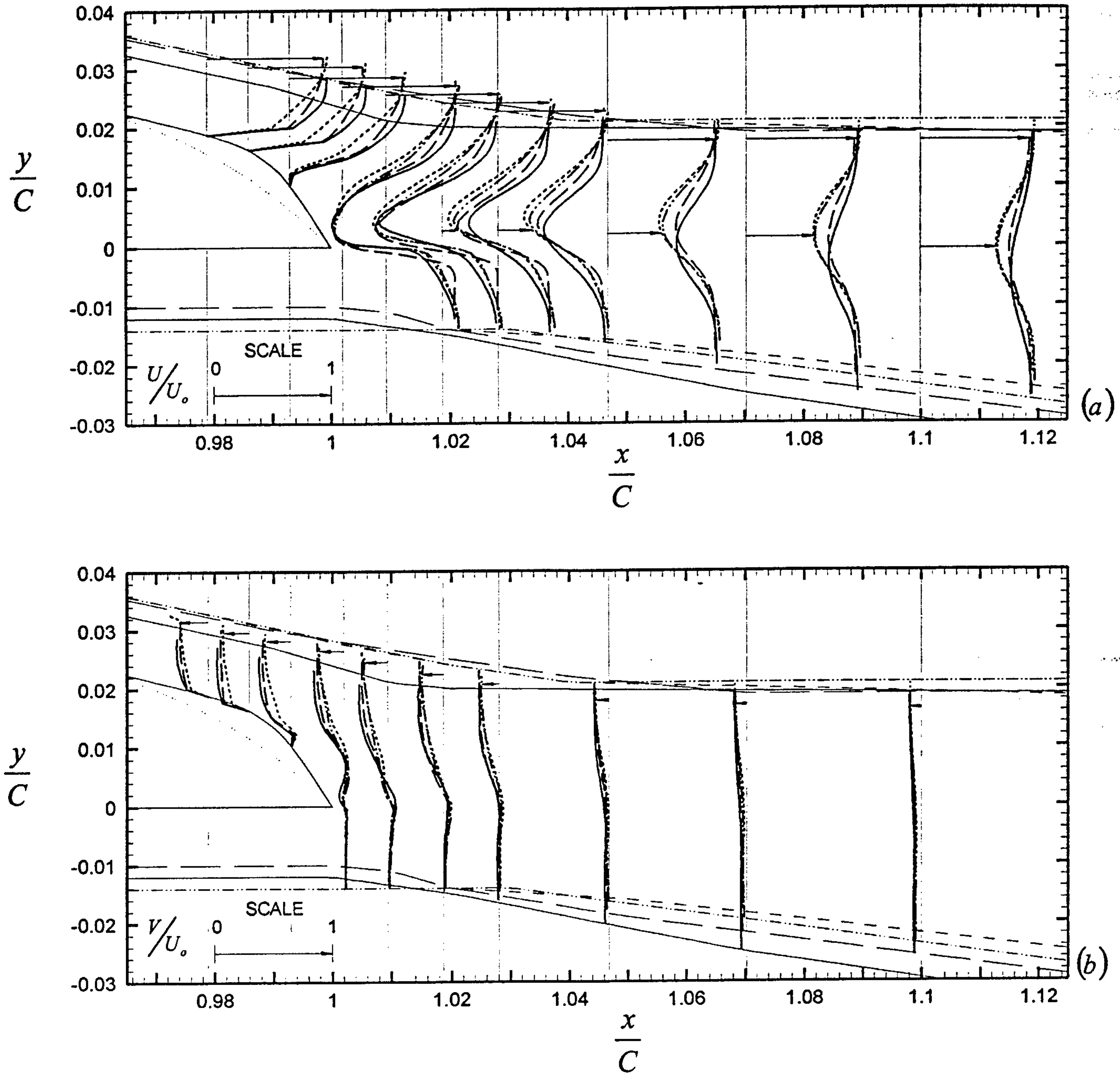0.04
0.03
0.02
0.01
0
-0.01
-0.02
-0.03
y/C
SCALE
U/U_o
0
1
0.98
1
1.02
1.04
1.06
1.08
1.1
1.12
x/C
(a)
0.04
0.03
0.02
0.01
0
-0.01
-0.02
-0.03
y/C
SCALE
V/U_o
0
1
0.98
1
1.02
1.04
1.06
1.08
1.1
1.12
x/C
(b)

Fig. 13

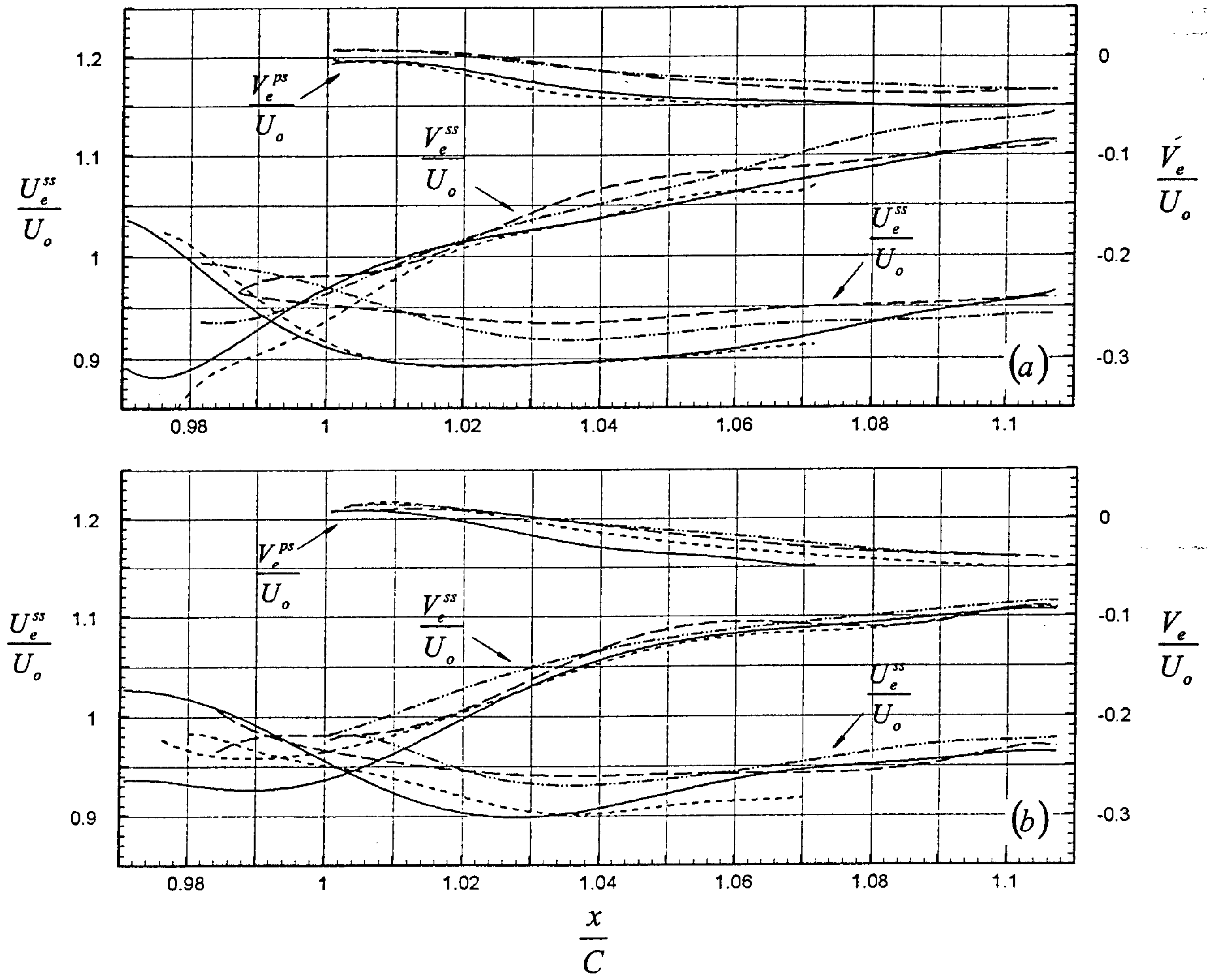
$\frac{V_e^{ps}}{U_o}$
$\frac{V_e^{ss}}{U_o}$
$\frac{U_e^{ss}}{U_o}$
$\frac{V_e}{U_o}$
1.2
1.1
1
0.9
0
-0.1
-0.2
-0.3
0.98
1
1.02
1.04
1.06
1.08
1.1
(a)
(b)
$\frac{x}{C}$

Fig. 14

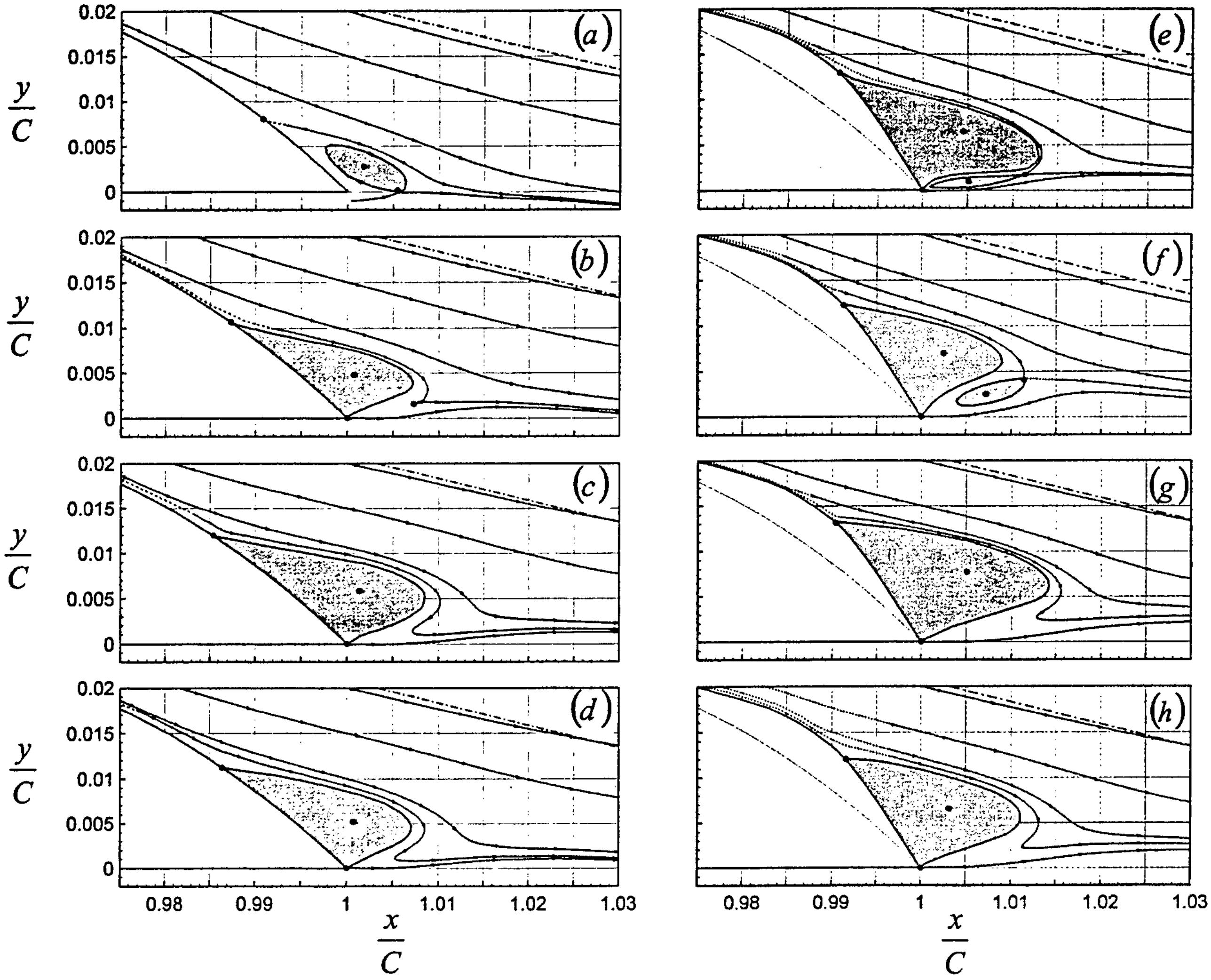

Fig. 15

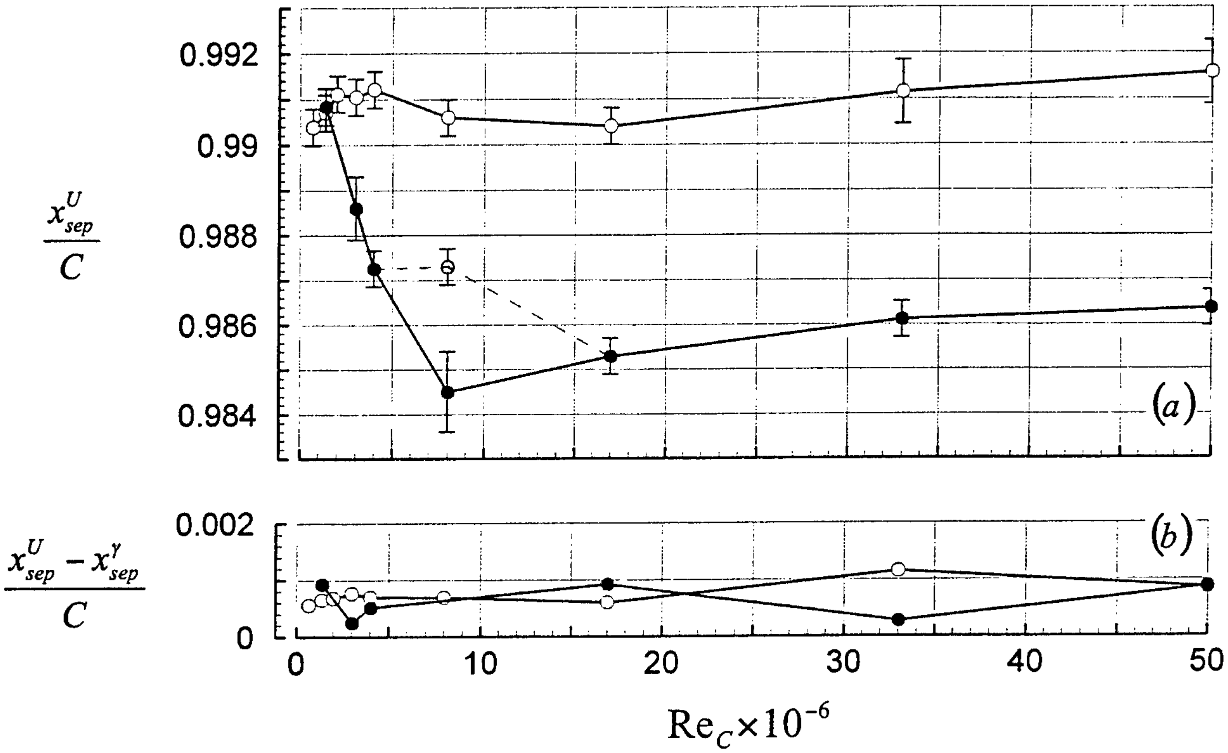
0.992
0.99
0.988
0.986
0.984
$\frac{x_{sep}^U}{C}$
(a)
0.002
0
$\frac{x_{sep}^U - x_{sep}^\gamma}{C}$
(b)
0
10
20
30
40
50
$\mathrm{Re}_C \times 10^{-6}$

Fig. 16

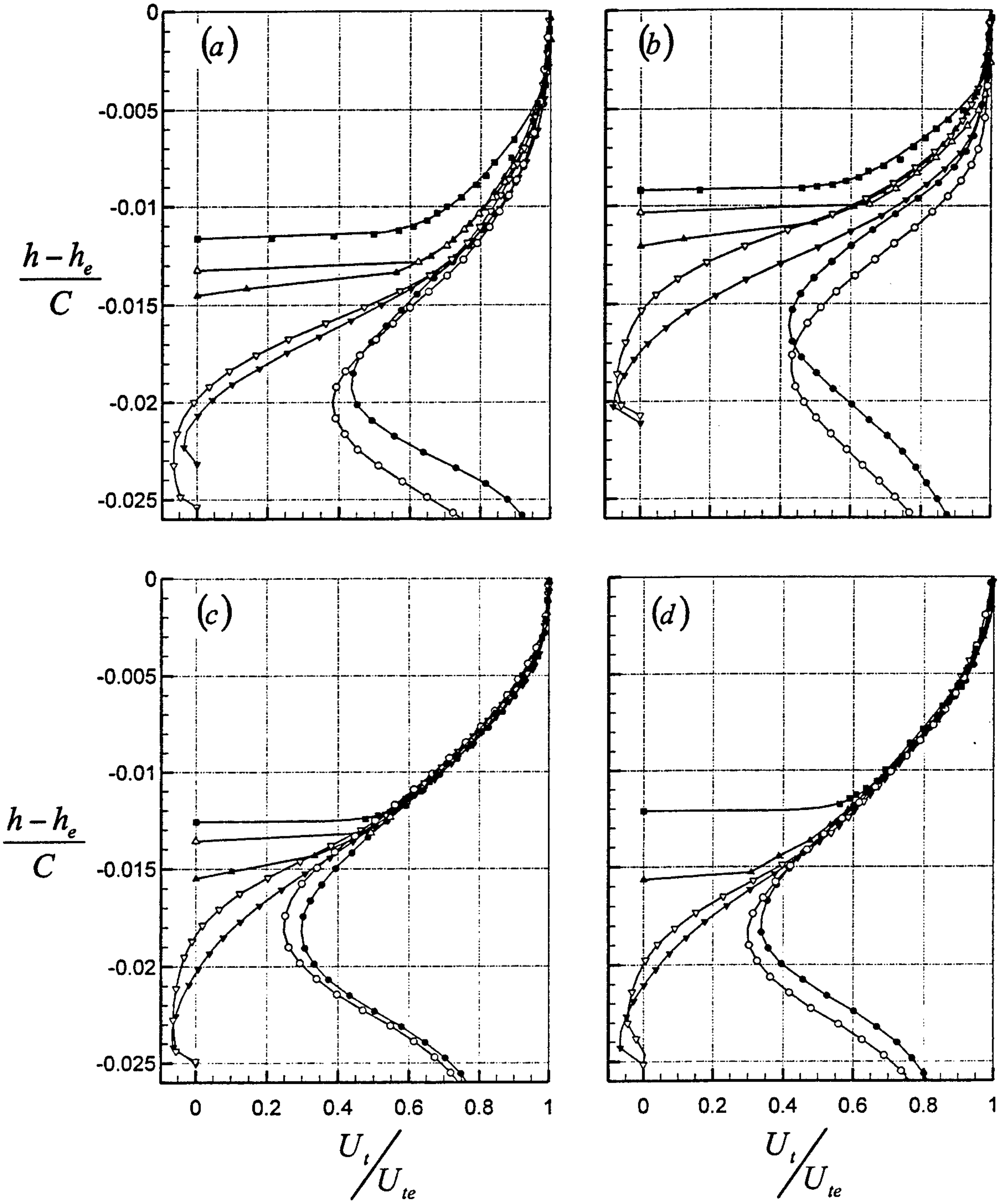

Fig. 17

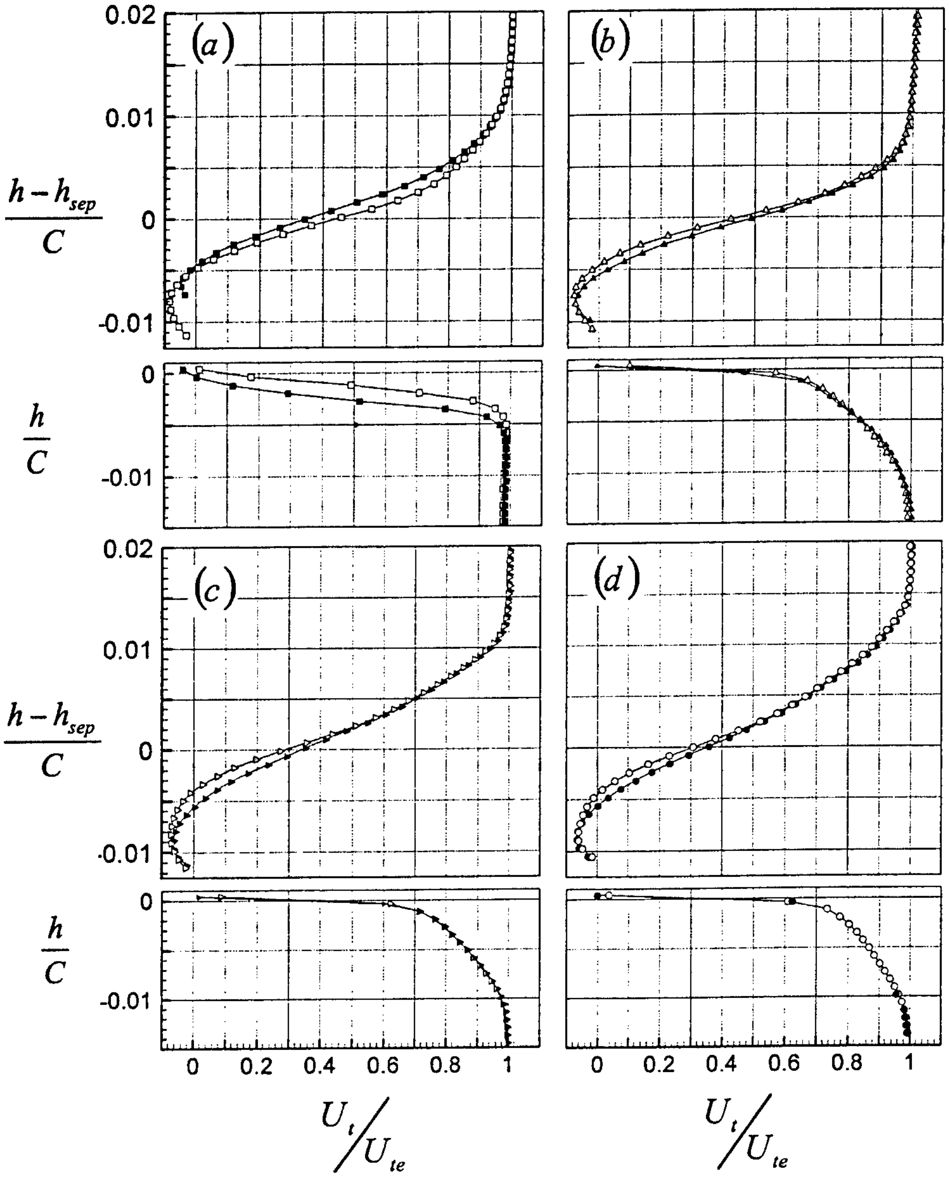

Fig. 18

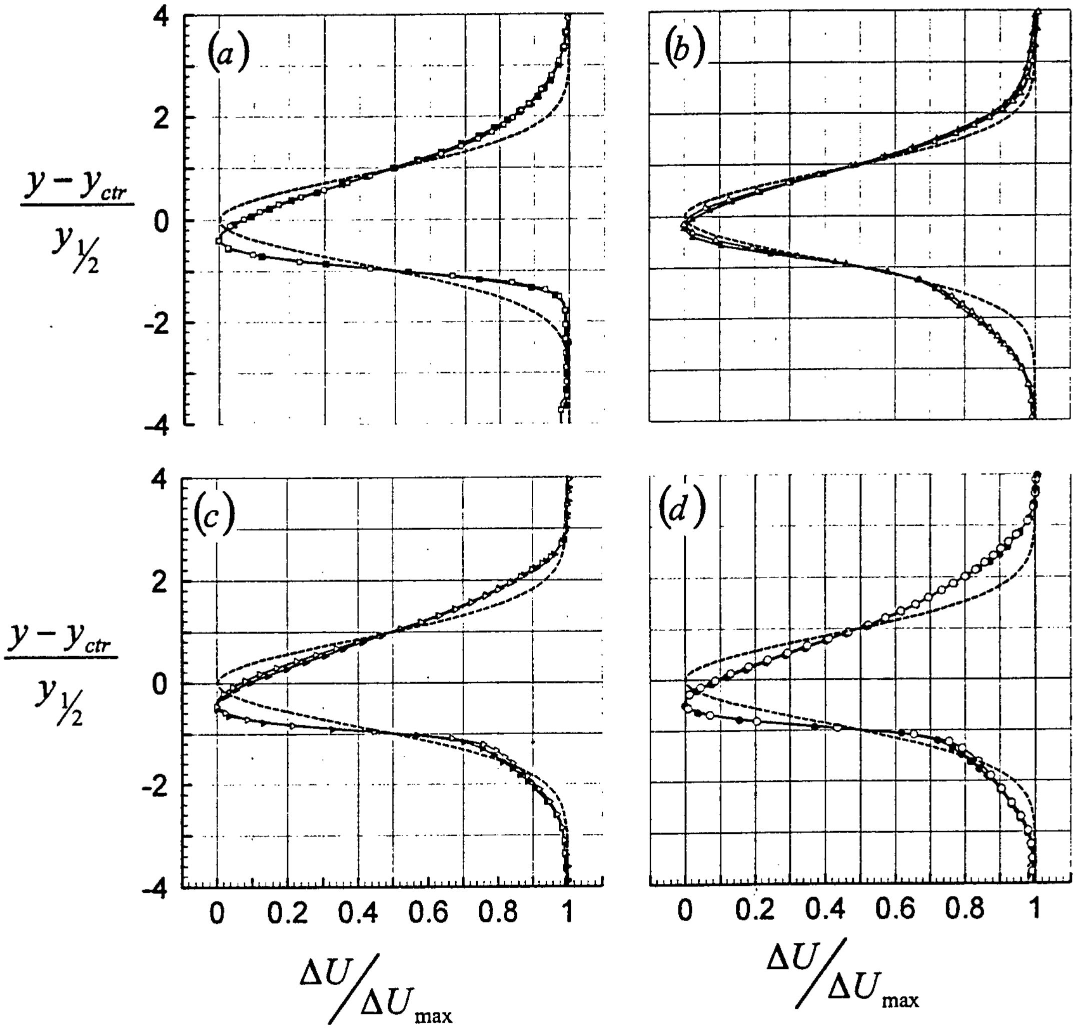

Fig. 19

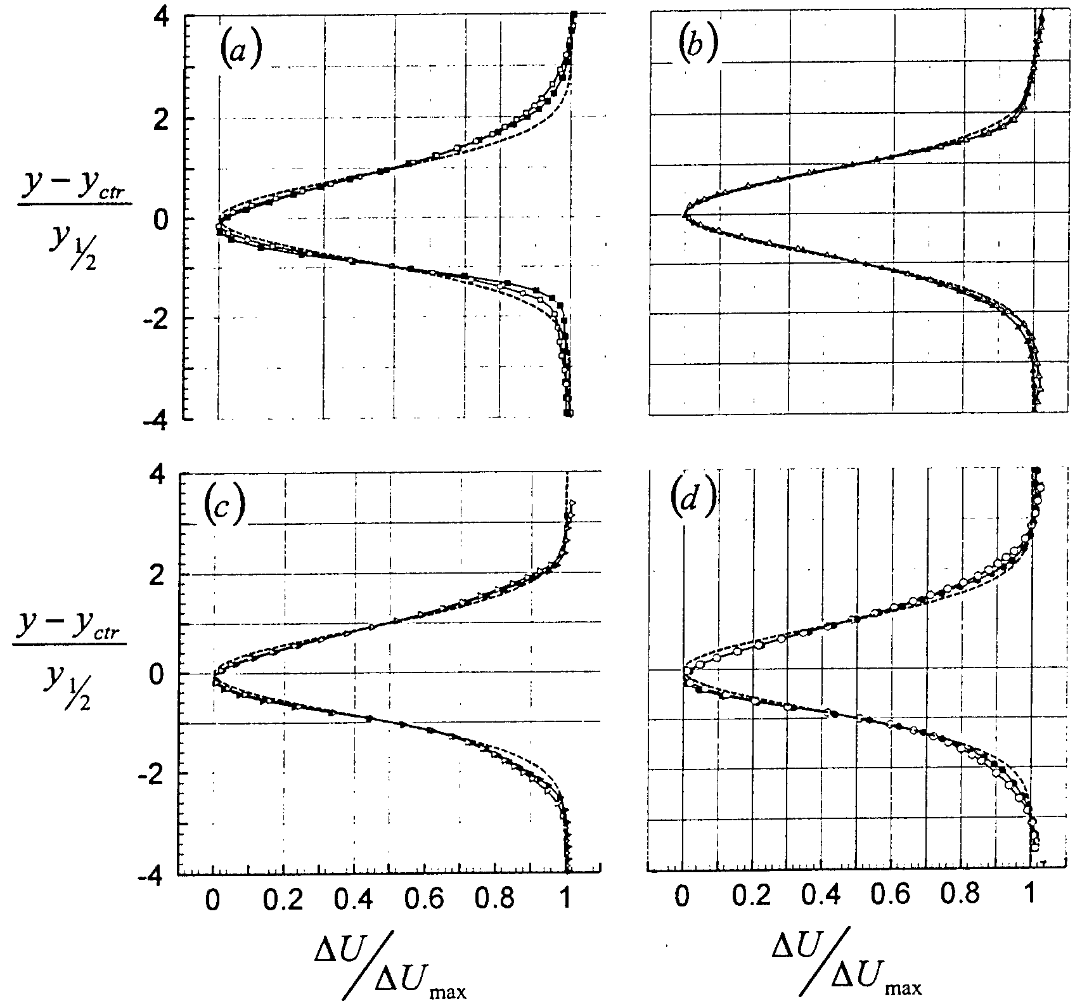

Fig. 20

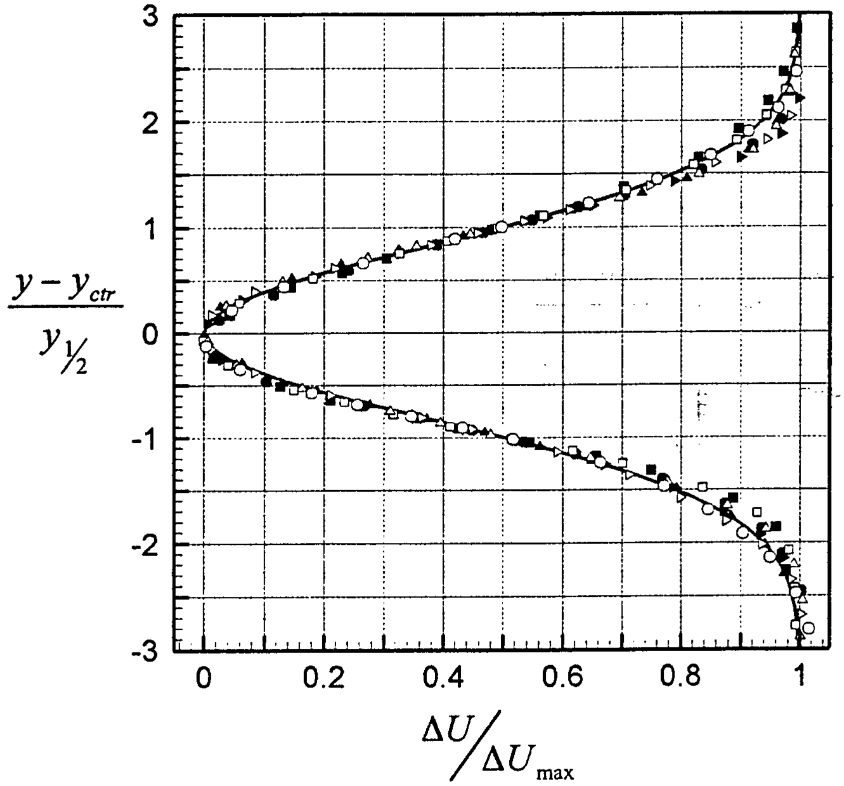

Fig. 21

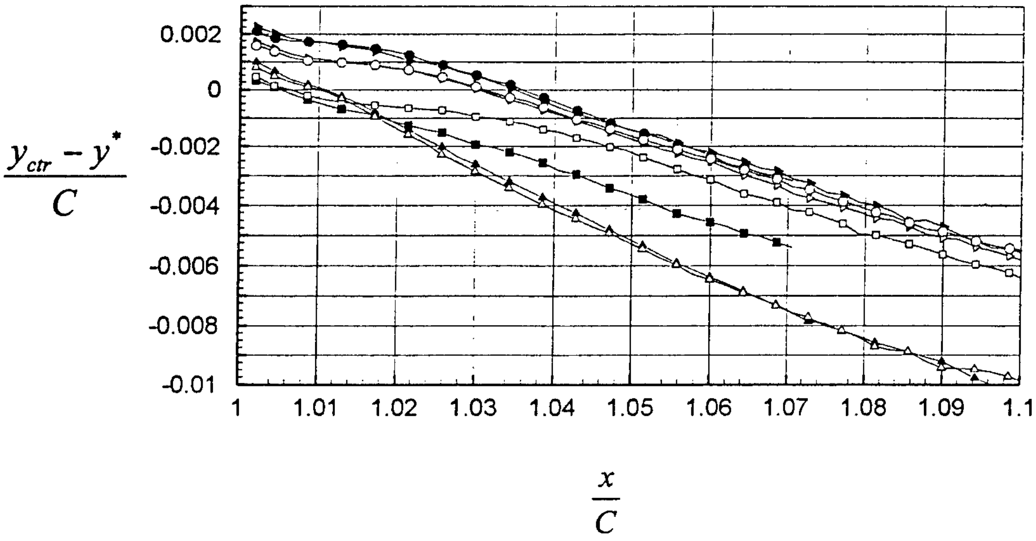

0.002
0
-0.002
-0.004
-0.006
-0.008
-0.01
1
1.01
1.02
1.03
1.04
1.05
1.06
1.07
1.08
1.09
1.1
$\frac{y_{ctr} - y^*}{C}$
$\frac{x}{C}$

Fig. 22

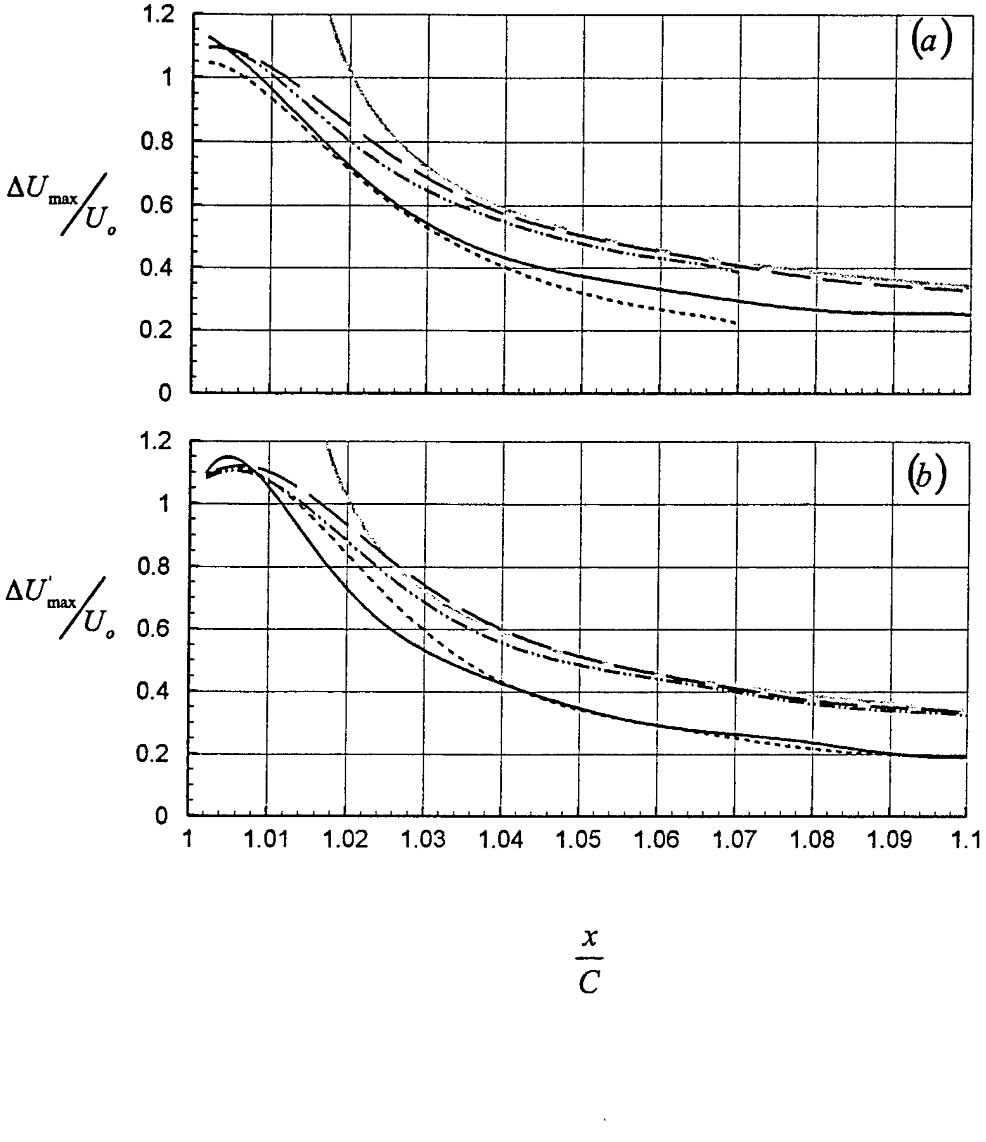
(a)
(b)
$\Delta U_{max}/U_o$
$\Delta U'_{max}/U_o$
0
0.2
0.4
0.6
0.8
1
1.2
1
1.01
1.02
1.03
1.04
1.05
1.06
1.07
1.08
1.09
1.1
$\frac{x}{C}$

Fig. 23

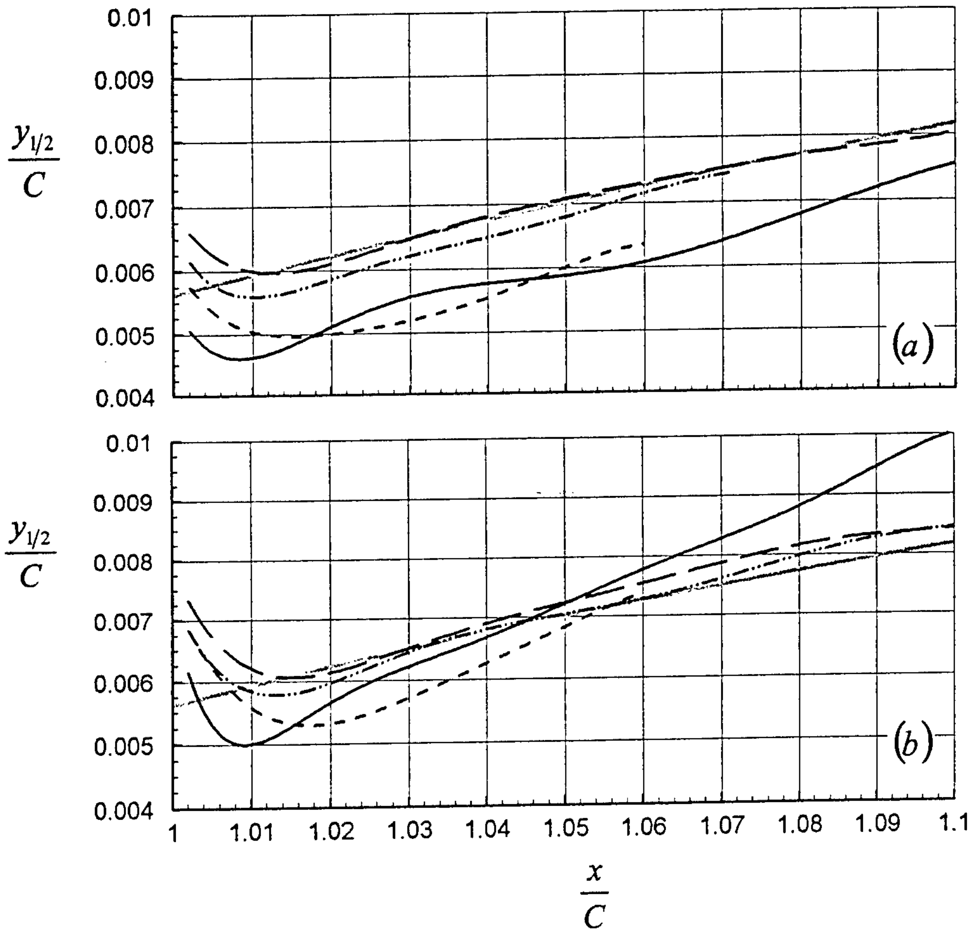

$\frac{y_{1/2}}{C}$
0.01
0.009
0.008
0.007
0.006
0.005
0.004
(a)
(b)
1
1.01
1.02
1.03
1.04
1.05
1.06
1.07
1.08
1.09
1.1
$\frac{x}{C}$

Fig. 24

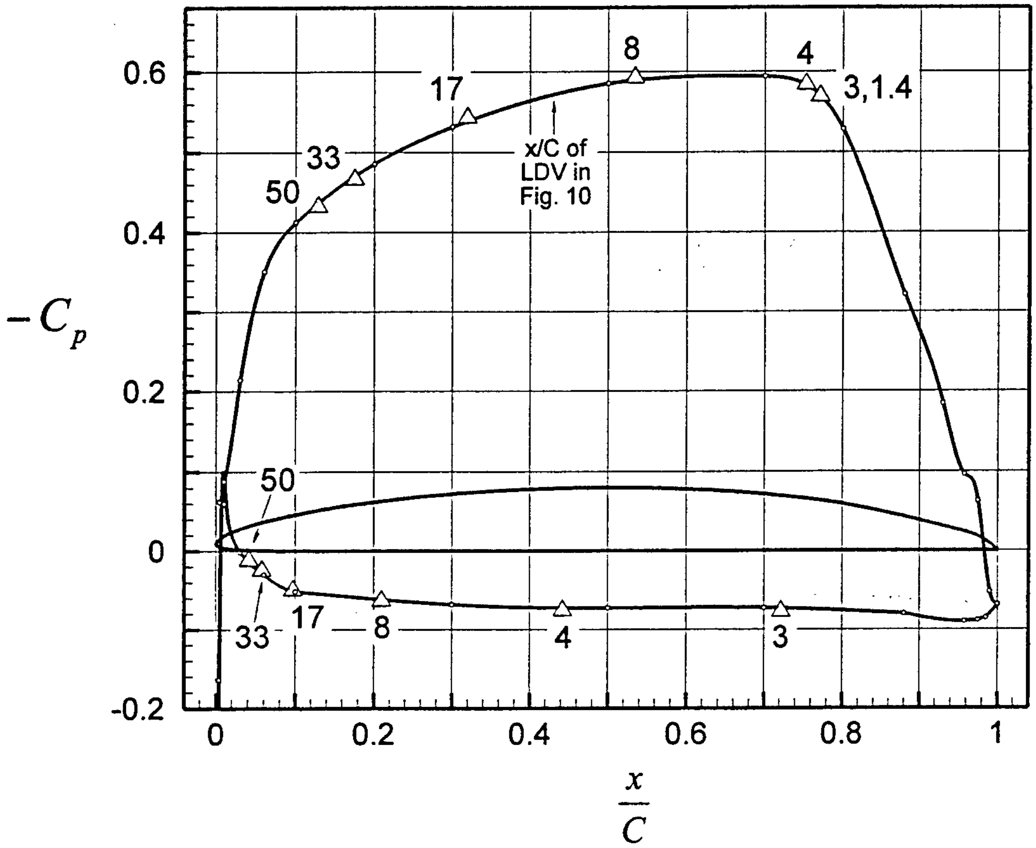
8
4
3,1.4
17
33
50
x/C of
LDV in
Fig. 10
50
33
17
8
4
3
0.6
0.4
0.2
0
-0.2
$-C_p$
0
0.2
0.4
0.6
0.8
1
$\frac{x}{C}$

Fig. 25

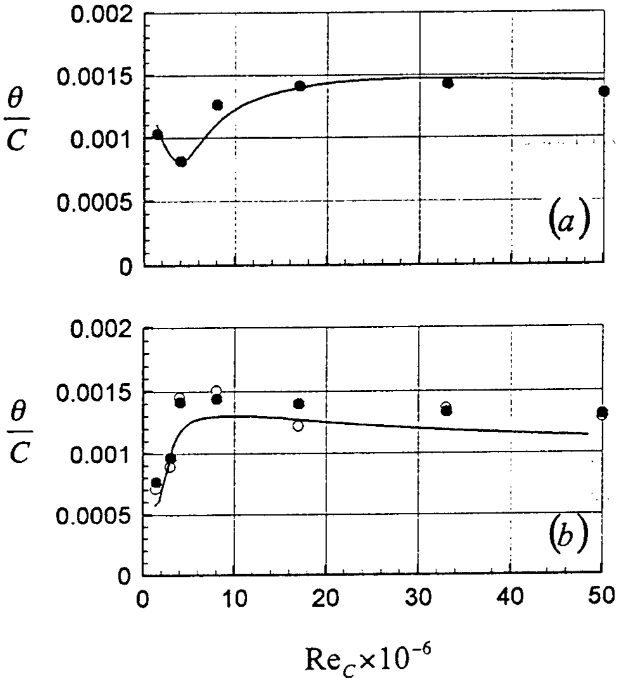
0.002
0.0015
0.001
0.0005
0
$\frac{\theta}{C}$
(a)
0.002
0.0015
0.001
0.0005
0
$\frac{\theta}{C}$
(b)
0
10
20
30
40
50
$\mathrm{Re}_C \times 10^{-6}$

Fig. 26

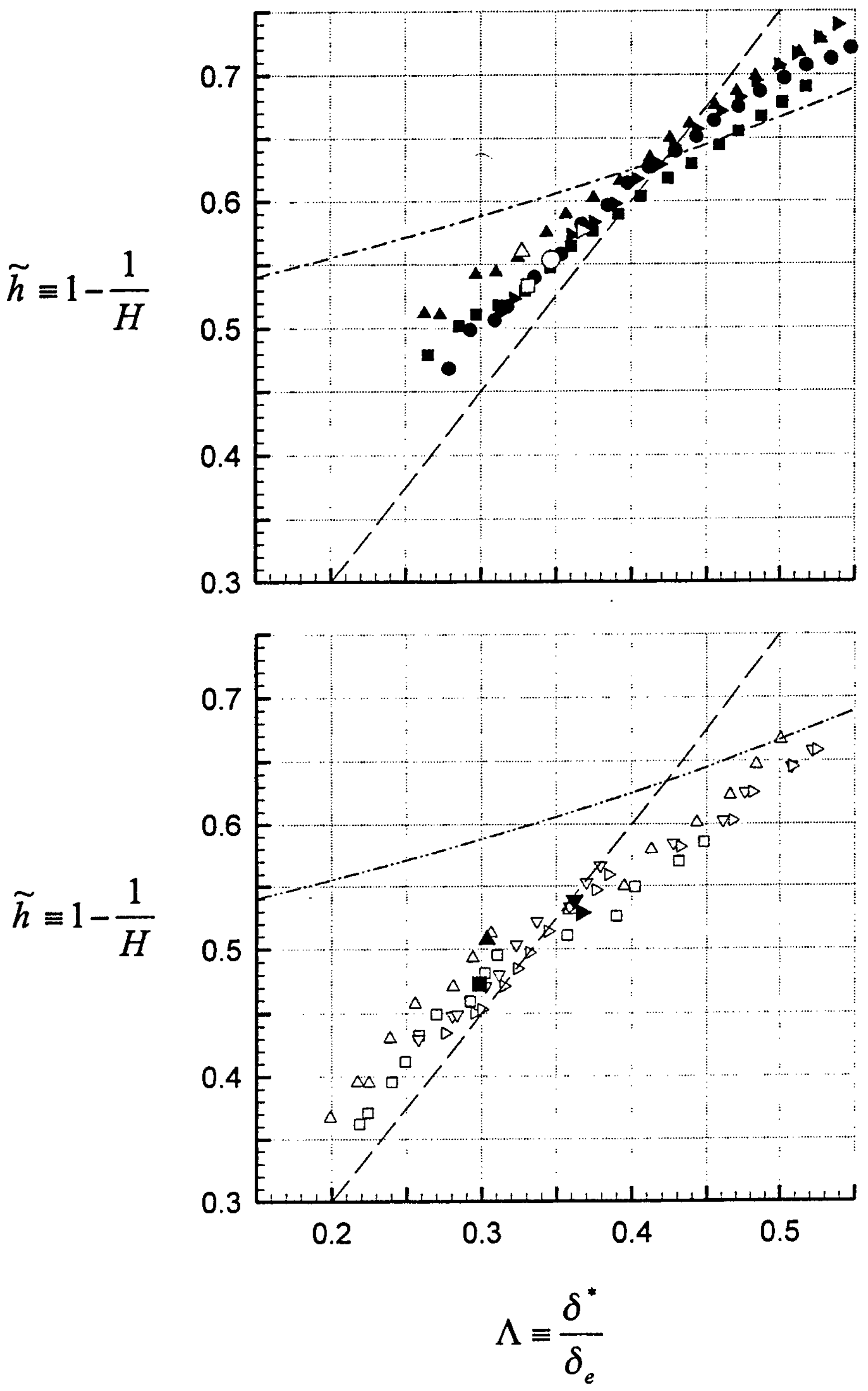

0.7
0.6
0.5
0.4
0.3
$\tilde{h} \equiv 1 - \frac{1}{H}$
0.2
0.3
0.4
0.5
$\Lambda \equiv \frac{\delta^*}{\delta_e}$

Fig. 27

DYNAMIC FLOW OVER A HYDROFOIL AT HIGH REYNOLDS NUMBER

(Submitted to the *Journal of Fluid Mechanics*, July 2003)

DWAYNE A. BOURGOYNE, STEVEN L. CECCIO AND DAVID R. DOWLING

Department of Mechanical Engineering
University of Michigan, Ann Arbor, MI 48109, USA

ABSTRACT

High Reynolds number (Re) wall-bounded turbulent flows occur in many aero- and hydrodynamic applications. However, the relative dearth of high-Re experimental data has hampered the development and validation of scaling laws and modeling techniques applicable to such flows. This paper presents measurements of the Re-dependent turbulent flow features found near the trailing edge of a two-dimensional lifting surface at chord-based Reynolds numbers, Re_C, typical of heavy-lift aircraft wings and full-scale ship propellers. The experiments were conducted in the William B. Morgan Large Cavitation Channel at flow speeds from 0.25 to 18.3 m/s with a cambered hydrofoil having a 3.05 meter span and a 2.13 m chord that generated 60 metric tons of lift at the highest flow speed, $Re_C \geq 50$ million (50M). The dynamic flow field and surface pressure measurements reported here were made near the foil's trailing edge which could be altered to have an apex bevel angle of either 44° or 56°. Although generic turbulent boundary layer and wake characteristics were found at any fixed Re_C in the trailing edge region, the flow field characteristics were found to be Re-dependent because of the variable strength of near wake vortex shedding. Analysis of planar particle-imaging-velocimetry flow-field measurements suggests that near wake vortex shedding is strongest when boundary layer vorticity shed at the trailing edge from the pressure side of the foil is most effectively rolled-up by the suction-side shear layer which separates upstream of the trailing edge. A scaling law for this phenomenon based on Biot-Savart induction concepts for suction-side shear-layer vorticity collapses vortex shedding strength measurements for $1.4\text{M} \leq Re_C \leq 50\text{M}$ from both trailing edges and from prior measurements on minimally-lifting struts at $Re_C \sim 2\text{M}$.

1. INTRODUCTION

High Reynolds number (Re) flows of both human and natural origin are commonly turbulent and the characteristics of the turbulence may depend on Re, particularly if the flow is wall-bounded as is the case in many aero- and hydrodynamic applications. Here the disparate phenomena associated with near-wall viscous flow and nearly-inviscid outer-flow fluctuations may compete with each other to cause subtle variations as Re increases. Two examples of such mild Re variation at high Re are the gradual decay of the skin-friction coefficient as the downstream-distance-based Re increases on a smooth flat plate, and the decline of the friction factor as the bulk-flow Re increases inside a smooth-wall pipe. These mild wall-bounded-flow variations with increasing Re may influence fluctuation levels in downstream free turbulent flows that form when the wall-bounded flow separates from the bounding surface. In particular, shear layers and wakes formed downstream of separation points on bluff or slender bodies may develop strong localized vortices that augment measured turbulence intensity levels when they are present. The relative presence or absence, and geometrical arrangement of such strong vortices may sometimes be linked to the characteristics of the upstream wall bounded flow.

This paper presents an experimental study of this phenomenon at high Re. It documents how mild Re-induced variations in the boundary layers on a two-dimensional hydrofoil govern the strength of near wake vortex shedding at chord-based Reynolds numbers, $Re_C = U_o C/\nu$ (where U_o is the flow speed far upstream of the body, C is the chord length of the surface, and ν is the kinematic viscosity of the fluid) from near 1 million (1M) to more than 50 million (50M). These experiments span the Re-gap between prior research studies (Re_C up to 2M or so) and full-scale applications, heavy-lift aircraft wings or ship propellers (30M $\leq Re_C \leq$ 100M). In particular, the *dynamic* flow-field and surface-pressure measurements reported here were collected in the trailing edge region of the hydrofoil at low Mach number (Ma). Here, the term *dynamic* is intended to include all unsteady features of the flow field whether they occur at large-scale with some organization (vortex shedding) or involve a wide range of length scales with less apparent organization (turbulence). Our companion paper (Bourgoyne et al. 2003, hereafter referred to as Part I) reports time-averaged flow-field measurements for the same hydrofoil.

Vortex shedding in the near wake of hydrofoils, airfoils, and turbine blades may cause unwanted hydroacoustic or aeroacoustic noise. Reduction, elimination or control of such noise has motivated much prior research – and the current study – into the fluid mechanics leading to vortex shedding. For hydrofoils, Blake (1986) provides a comprehensive review of work prior to the early 1980's. Included is a summary of experiments that shows trailing-edge vortex shedding to be pronounced on symmetric and blunt trailing edge geometries. Similar results are also found in Blake and Gershfeld (1989). Vortex shedding downstream of a blunt vibrating trailing edge is reported by Lotfy and Rockwell (1993) where additional contributions to shedding research are listed. Prasad & Williamson (1997) review of the vortex dynamics pertaining to the wakes of bluff bodies. Some studies attribute vortex shedding to absolute instability of wake flows. Overviews of global flow instabilities and blunt-body wake flows are provided by Huerre and Monkewitz (1990) and Oertel (1990), respectively

The aeroacoustics of a variety of lifting surfaces has recently received both experimental (Swales and Lowson 1997, Minniti and Mueller 1998, Luire et al. 1998, and Roger and Moreau 2002) and numerical (Ho and Lakshminarayana 1997, Knight and Peltier 1997, Howe 1999, 2000, Manoha, et. al. 2000 , and Wang and Moin 2000, 2002) attention. The most recent of these computational studies applies large eddy simulation to predict sound generated by a minimally-lifting strut (Blake 1975). However, the vast majority of this aeroacoustic work is for minimally lifting bodies at Re_C of less than several million, below the Re_C range of full-scale applications.

Similar studies of vortex shedding and wake turbulence have also been conducted to understand the performance of compressor and turbine blades, and airfoil cascades. Part I lists prior studies in this area that include mean flow results, but these prior studies include dynamic flow results as well. Literature reviews of unsteady wakes from turbomachinery blades are given in Cicatelli and Sieverding (1995), and Ubaldi et al. (1996). Although many studies of this type involve significant Ma flow, such studies still offer some insight into the behavior of equivalent incompressible flows. For example, Sieverding and Heinemann (1990) report that the Strouhal number (*St*) is not strongly dependent on Ma in the subsonic regime, but instead depends more on Re and boundary layer state. The more recent experimental work in this area (Cicatelli and Sieverding 1996, Rowe et al. 2001, Ubaldi & Zunino 2000) places a greater emphasis on determining the frequency of shedding rather than on parameterizing its strength, a primary objective of the present study.

The prior studies having the greatest significance for the findings presented herein involve extended (or streamlined) bodies at low Ma. Greenway and Wood (1973) conducted an experimental study of vortex shedding behind two-dimensional minimally-lifting struts with beveled trailing edges at $Re_C \sim$ 1M, and report that *i*) vortex shedding can be altered with variations in the trailing edge apex angle, and *ii*) the state of the separating boundary layers at the trailing edge and their size relative to their vertical spacing are important factors for vortex shedding. They attribute this second observation to a number of prior investigations including that of Gerrard (1966). Trailing edge bevel angle changes and variable boundary layer characteristics are also included in the present study. Boldman et al (1976) showed how vortex shedding from a blunt trailing edge can be reduced by unequal freestream velocities on either side of a splitter plate. A similar ratio of freestream velocities appears in the proposed scaling parameter for vortex shedding strength in the present study [see Eq. (4)] but was not directly investigated. Blake (1984) examined the flow over and downstream of two-dimensional minimally-lifting struts with trailing edges very similar to those in the present study, and found that shedding strength, as measured by wake velocity spectra, is affected by trailing edge bevel geometry. More recently, Sieverding and Heinemann (1990) observed that trailing edge geometry and Re_C can have similar effects on St in the flow over a strut at low Ma, and proposed that the state of the separated boundary layers determines the shedding process. The present study echoes these results at higher Re_C on a foil with significant lift.

All of this prior work indicates that vortex shedding is highly sensitive to the properties of trailing-edge boundary layers and shear layers. Unfortunately, this sensitivity limits the generality of results for a given geometry and Re_C. For example, results for bluff bodies cannot be fully applied to streamlined bodies because the interaction between the leading-edge stagnation point and trailing edge flow dynamics is more subdued in for streamline bodies. Furthermore, vortex shedding results for minimally-lifting streamlined bodies cannot be directly applied to lifting surfaces because the sensitivity of vortex shedding to trailing-edge boundary layer state confers an importance to the pressure gradients associated with lift that modulate boundary layer development upstream of the trailing edge. Even among lifting surfaces, important differences arise from variations in trailing edge geometry, such as the effect of a suction-side trailing-edge bevel, a geometrical feature commonly implemented on propeller blades to ensure structural integrity during severe off-design conditions. However, even beyond issues of geometry, there is also potential for Re-dependence in aspects of boundary layer growth, separation, and shear layer development (see Part I).

To address these issues, the present experimental study employs a large two-dimensional hydrofoil in a large high-speed water tunnel and achieves Re_C values which bridge the gap between prior work and many full-scale applications. The model incorporates an application-relevant suction side surface, with a variable-angle trailing-edge bevel, that leads to section lift coefficients of 0.52 to 0.55 (see Part I). This paper documents the dynamic flow over the hydrofoil – including turbulence statistics and vortex shedding characteristics – from just upstream of suction side boundary layer separation through the development of the near wake for Re_C = 1.4M to 50M. In addition, a simple scaling relationship, which may be generally applicable to trailing-edge near-wake flows, is deduced from the experimental measurements. This relationship successfully collapses the available shedding strength measurements and may provide a means for assessing the likely strength of vortex shedding based on foil geometry and time-averaged flow parameters alone.

The remainder of this paper is divided into five sections. The next section (§2) covers the experimental setup and techniques. The third section presents the flow-field measurements that document how variation in Re_C or trailing-edge geometry may increase or decrease the prominence of trailing edge vortex shedding. The fourth section describes our attempt to extract and quantify the mechanism(s) underlying vortex shedding. The fifth section explains the construction of a scaling relationship that may have predictive capabilities. The final section (§6) summarizes this research effort and presents the conclusions drawn from it.

2. EXPERIMENTAL SETUP AND TECHNIQUES

The test facility, test model, instrumentation, calibration, and estimates of uncertainty in the mean flow measurements are fully described in Part I. This section provides a brief summary of that material along with additional experimental details relevant to the measurements of flow dynamics near the trailing edge of the hydrofoil.

The hydrofoil was tested in the William B. Morgan Large Cavitation Channel (LCC), a low-turbulence recirculating water tunnel with a 3.05 m by 3.05 m by 13 m test section capable of steady flow speeds (U_o) from 0.25 m/s to 18.3 m/s. The hydrofoil ($C = 2.134$ m chord, 0.171 m maximum thickness, depicted in Fig. 1) was centered in and spanned the LCC test section for a 6% blockage ratio. Its cross section was a modified NACA-16 suction side that ended in a trailing edge bevel with a 44° (Geometry I) or 56° (Geometry II) apex angle. The pressure side of the hydrofoil was flat aft of 28% chord. The foil's surface was polished to a nominal roughness of 0.25 μm, and neither the suction nor pressure side boundary layers were tripped. The foil's angle of attack (measured with respect to the flat pressure side) for these tests was 0°. The foil generated 590 kN (60 metric tons) of lift with U_o = 18.3 m/s. The LCC water temperature varied from 24 °C to 40 °C during these tests so the Re_C values quoted herein are for the average water temperature of (32 °C) and have a nominal ±10% variation.

Single-point two-component Laser-Doppler velocimetry (LDV) and planar two-component particle-imaging velocimetry (PIV) were used to measure fluid velocity in the vicinity of the foil's trailing edge. Seed particles for the LDV system were silicon carbide with a nominal diameter of 2 μm. Seed particles for the PIV system were 16 μm silver-coated glass spheres. The LCC was flood seeded with both types of particles. The LDV system (built by Dantec) produced a long narrow focal volume (170 μm diameter, 6 mm length) oriented parallel to the foil span. The PIV system used two side-by-side LaVision Flowmaster 1024 x 1280 digital cameras, LaVision software, and two Spectra-Physics flash-lamp-pumped Nd-YAG lasers delivering 800 mJ at 532 nm. The laser sheet thickness was masked to 3 mm. The imaging ratio of 0.1 mm to 1 pixel and the 32 by 32 interrogation window – typically capturing ten particle pairs – set the PIV resolution at one fluid velocity vector for a cube 3 mm on a side. The image capture rate was ~1 Hz and 500 to 2000 images were acquired at each flow condition.

Uncertainties in the LDV-acquired and PIV-acquired velocity fluctuations include both bias and random error. While bias error in the LDV velocity fluctuations is negligible, the fluctuations are presented as normalized quantities, and bias enters through the normalization value, U_o. This bias is estimated to be ±0.2% of the freestream velocity. Random error is negligible by comparison. Uncertainty in the instantaneous velocity vectors from the PIV, and the spatial location of these velocities, is discussed in Part I. Convergence of the turbulence statistics is addressed in Section 3.3 of this paper.

In the present study, the two-component LDV was used to acquire temporal velocity spectra at fixed points in the foil's near wake. Dantec software (*BSA Flow*) was used to estimate the power spectrum from uncorrelated particle bursts having random arrival times. This software employs sample-hold re-sampling, Hanning windowing, and Fast Fourier Transform (FFT) spectrum calculations. The data re-sampling has the effect of a low-pass filter. No high-pass filtering was employed, but the maximum re-sampling frequency was maintained at 2-3 times the mean data rate as a compromise between frequency resolution and high-frequency aliasing.

In addition to the velocity measurements, dynamic surface pressure measurements were made with an array of fifteen flush-mounted pressure transducers (PCB 138M101) located at the PIV measuring plane and in the vicinity of the hydrofoil trailing edge. These sensors were arrayed in an L-shape with lines of transducers set parallel and perpendicular to the flow direction. The results presented in this paper are from a single transducer located on the foil's pressure side nearest the trailing edge (x/C, y/C, z/S) = (0.990, 0, 0.36), where the *x* and *y* coordinates are defined in Fig. 1 and *z* completes a right-handed set of Cartesian axes. The dynamic pressure signals were analog band-pass filtered from 2 Hz to 5 kHz and sampled at 10 kHz.

Although the model and its mounting scheme were design to be as rigid (and durable) as possible, some model vibration did occur and was monitored with an array of eight accelerometers. A careful comparison of fluctuation spectra recorded by the trailing edge pressure transducers and the nearest accelerometer(s) did not reveal any significant correlations in the frequency range of interest. Furthermore, when the measured acceleration fluctuations were converted to root-mean-square (rms) surface velocities, their normalized levels (0.01%, worst case) were found to be well below that of the nominal peak freestream turbulence level of the tunnel (0.5%), and two or more orders of magnitude below the turbulent velocity fluctuations measured near the foil surface (~ 4 to 7%). Thus, the measurements reported here are believed to be free of model vibration contamination.

3. RESULTS

Experimental data were collected for both trailing edge geometries at the flow speeds and Reynolds numbers listed in Table 1. This table also includes the symbols and line types used to designate results at the various Re_C values. Geometry I (44° trailing edge apex angle) and Geometry II (56° trailing edge apex angle) results are reported filled and open symbols, respectively.

Fluid velocity measurements could be made with either the LDV or PIV systems (or both), and the relative advantages of each were exploited to optimize test time utilization. The PIV system provided instantaneous two-dimensional velocity fields from which spatial correlations, velocity gradients (vorticity), spatial spectra, and time-averaged results could be obtained. However, the PIV frame rate was insufficient to measure the temporal evolution of the flow, and its modest spatial resolution suppressed small-scale velocity fluctuations. The LDV system complemented the PIV system, and provided single-point measurements with higher spatial and temporal resolution from which turbulence statistics, temporal spectra, and time-averaged results could be obtained. The agreement between the time-averaged velocity measurements from each system was good. In addition, dynamic surface pressure was measured made near the foil's trailing edge.

The main goal of this paper is to present the Re and geometry dependence of the dynamic flow features in the vicinity of the foil's trailing edge. The following subsections cover the attached boundary layers approaching the trailing edge region (§3.1), separating boundary layers and the near wake (§3.2), comparison of LDV and PIV results (§3.3), near wake velocity fluctuations (§3.4), near-wake velocity spectra (§3.5), trailing edge surface pressure spectra (§3.6), and vortical flow features related to wake velocity fluctuations (§3.7).

3.1 Attached boundary layers approaching the trailing edge region

LDV-measured characteristics of the attached boundary layers approaching the trailing edge region (x/C=0.93) are presented in Fig. 2, for the (a) suction side and (b) pressure side of the Geometry I hydrofoil at Re_C = 1.4M, 4M, 17M, and 50M. Here, U and V are the x- and y-direction mean velocities, u' and v' are the x- and y-direction velocity fluctuations, y_o represents the foil surface in Fig. 2a, and U_e is the local horizontal flow speed at the outer edge of each boundary layer. All profiles represent turbulent boundary layers. The suction side boundary layer has higher fluctuation levels at the lower two Reynolds numbers. The differences in the fluctuation levels are believed to originate in the differing lengths of laminar, transitional, and turbulent boundary layer flow on the suction side of the foil at each Re. The pressure side boundary layer measurements at $x/C = 0.93$ are consistent with flat plate results. Pressure side boundary layer LDV measurements were not made at the lower two Re_Cs

3.2 Separating boundary layers and the near wake

An overview of LDV-measured velocity fluctuation levels with Geometry I is provided in Fig. 3. The three panels show multiple profiles of the normalized turbulent stresses, $\overline{u'^2}/U_o^2$, $\overline{v'^2}/U_o^2$, and $\overline{u'v'}/U_o^2$, upstream and downstream of the trailing edge, shown in the left half of each panel. The gray vertical lines indicate the positions at which the profiles were measured. A relative scale for the levels is given at the lower left of each panel. The smoothly-bending more-nearly-horizontal curves on each panel indicate the outer edges of the suction-side and pressure-side boundary layers and of the foil's wake, defined as the locations at which the streamwise velocity fluctuations fall below the noise level of the LDV measurements. In all cases, this noise level (approx. 1% of the freestream speed) was incoherently subtracted from the reported u' and v' variances. These fluctuation profiles have been minimally smoothed to improve graphical clarity using a three-data-point sliding window. Results from Re_C = 8M and 50M are shown and display a mild Re-dependence consistent with later downstream separation of the suction side boundary layer at Re_C = 50M. Results for Re_C = 17M and 33M (not shown) follow a monotonic trend between the plotted results at Re_C = 8M and 50M.

Similar overviews of the PIV-measured velocity fluctuation levels at Re_C = 1.4M, 4M, and 50M for Geometry I and Geometry II are provided in Figs. 4 and 5, respectively. The presentation format is the same as Fig. 3, including the x/C locations at which the data are presented, with one exception. Shadowing by the hydrofoil prevented PIV data acquisition on the foil's pressure side and compromises the very-near-wake data at $x/C < 1.002$ and $y/C < 0$, so the profiles plotted are from $x/C=1.002$ instead of $x/C=1.000$. For Geometry I, PIV data are not available at $Re_C = 1.4$M at the downstream station. For Geometry II, data are not available at $Re_C = 50$M at three upstream stations and at $x/C = 1.002$ and $y/C < 0$.

As with the LDV results shown on Fig. 2, differences exist in the data and are most evident when comparing the lower and higher Re_C measurements. The results most different from the others are those from $Re_C = 1.4$M with Geometry I, and $Re_C = 1.4$M and 4M with Geometry II. As discussed in Section 3.4 of Part I, the pressure side boundary layer on Geometry I appears to separate upstream of the trailing edge at $Re_C = 1.4$M; at all other conditions the pressure boundary layer separates at the trailing edge. Such early separation could lead to the unique downward shift of the $Re_C = 1.4$M Geometry-I pressure-side fluctuation profiles. For Geometry II, the elevated turbulence levels at the lower two Re_C arise from strong vortex shedding at these conditions. In particular, Fig. 5b shows $\overline{v'^2}/U_o^2$ to be much higher at these two conditions, particularly in the region downstream of the trailing edge near $y = 0$. Such elevated vertical velocity fluctuations figure prominently in a simple scaling analysis of vortex shedding presented in §5.1. At $Re_C \geq 17$M, the PIV-measured fluctuation profiles show the same mild Re-dependence found in the LDV data (see Fig. 2). However, the PIV-data at $Re_C = 17$M and 33M are so similar to those at 50M that they were omitted from Figs. 4 and 5 for graphical clarity

3.3 Comparison of LDV and PIV results

A comparison of the Geometry I LDV and PIV results at $\mathrm{Re}_C = 50$M (see Figs. 2 and 4) reveals similar trends and profile shapes but disagreements in magnitude. The differences are attributed to differing levels of statistical convergence, processing artifacts in the PIV measurements, and the superior spatial resolution of the LDV measurements. The statistical convergence of each measurement was set by a compromise between test time at each condition and the total number of conditions tested. Here, the longest fluctuation time scale in the foil's near wake flow is the vortex shedding period, $T = 1/f_p \approx 2\pi\Delta_y^{nom}/U_o$ (Blake 1986) where Δ_y^{nom} is the nominal near wake thickness. Single-point LDV measurements typically involved 500 to 12,000 particle bursts in a sampling period of 0.6 min., approximately $600T$ to $3{,}600T$ at Re_C = 8M and 50M, respectively. For the PIV measurements, 1,000 to 2,000 images were recorded at each test condition in multiple runs of 80 images each over a test time of 30 to 60 minutes, a sampling period of $\sim 10^5 T$. Figure 6 shows sample convergence histories for the PIV measurements at Re_C = 50M, and these results indicate that 2,000 PIV images yield well converged mean values (Fig. 6a) and adequately converged turbulence statistics (Fig. 6b).

The poorest agreement between the LDV and PIV flow fluctuation measurements occurred at Re_C = 50M in the profiles at x/C = 1.0094 (see Fig. 7). In general, the PIV measurements fall below the LDV results because of the additional spatial filtering associated with the larger PIV interrogation volumes. However, the peak pressure-side PIV results for $\overline{u'^2}/U_o^2$ and $\overline{u'v'}/U_o^2$ do occasionally exceed the LDV values. This occurs at this location because the PIV interrogation volume spans a region of high streamwise-velocity gradient. A random distribution of particles in such an interrogation volume and the recursive PIV image-processing software tend to produce extreme – as opposed to spatially averaged – instantaneous horizontal velocities, thus raising the fluctuation levels at this location. Fortunately, this problem appears to be confined to $1.00 < x/C \leq 1.01$ and $y \approx 0$. Figure 8 provides a further quantitative comparison between the LDV and PIV results. Here, the ratios of LDV-measured fluctuations divided by PIV-measured fluctuations are provided vs. Re_C for the peak suction-side values of $\overline{u'^2}/U_o^2$, $\overline{v'^2}/U_o^2$, and $\overline{u'v'}/U_o^2$ at $x/C = 1.0094$. For these suction side ratios, the LDV measurements produce consistently higher fluctuation levels and PIV-measurement spatial averaging in both the streamwise and vertical directions must be considered in order to quantitatively account for the differences shown on Fig. 8. Nevertheless, the agreement between LDV and PIV measurements improves with decreasing Re_C, as would be expected if their differences are related to varying resolution of the energy-containing flow scales.

The remainder of this paper relies on the PIV measurements for which more conditions were measured and from which the spatial characteristics of the instantaneous flow fields can be deduced. However, these results must be interpreted in light of the spatial averaging inherent in the PIV measurements.

3.4 Near-wake velocity fluctuations

The Re and geometry-dependence of the near wake shown in Figs. 4b and 5b may be illustrated concisely by plotting the curves of the y-location at which the fluctuation levels are maximum for a given x-coordinate, and the fluctuation levels recorded along such curves. The results for the normalized vertical velocity variance, $\overline{v'^2}/U_o^2$, are given in Figs. 9 and 10 for Geometry I and II, respectively. Values for $1.000 < x/C < 1.005$ are not plotted because the suction and pressure sides peaks of $\overline{v'^2}/U_o^2$ are comparable and consistent selection of a single peak is problematic. In Fig. 9a, the $Re_C = 1.4$M case is clearly different, and this is again attributed to pressure side boundary layer separation prior to the trailing edge. Results at the other Re_Cs are more similar, though close examination of Fig. 9b reveals some Re-variation in the downstream location of the maximum fluctuations. By comparison, dramatic Re-variation in the location of maximum fluctuations is shown for Geometry II in Fig. 10. Here, the point of maximum fluctuations resides near x/C=1.03 at $Re_C = 1.4$M, progresses upstream towards the trailing edge as Re_C is increased to 4M, and then progresses downstream again when Re increases to 17M or higher. A comparison of Figs. 9b and 10b also shows enhanced vertical velocity fluctuations occur with Geometry II.

Figures 11 and 12 follow the same format as Figs. 9 and 10, but give the downstream evolution of the normalized Reynolds shear stress, $-\overline{u'v'}/U_o^2$, taken from Figs. 4c and 5c. The stress profiles have two extremes of opposite signs, and the coordinates and values of both are plotted. Since the locations of peak Reynolds stress mark the shear layers centers, Figs. 11a and 12a give an indication of the evolution of the wake thickness. As found by other researchers (Blake 1986), the vertical separation of the shear layers initially decreases but then increases, and the location of closest approach coincides with the downstream location of the Reynolds shear stress extremes. As with Fig. 9a, Fig. 11a shows Geometry I at $Re_C = 1.4$M as a distinguished case. The initiation of the peak pressure-side Reynolds shear stress curve at $y/C = -0.002$ is consistent with early pressure side separation. In Fig. 12 for Geometry II, as in Fig. 10, the downstream distance at which the peak stresses are encountered vary significantly with Re_C. And again, comparison of Figs. 11b and 12b shows enhanced shear stress occurs in the pressure side shear layer with Geometry II.

Figures 13, 14 and 15 show the near wake evolution using velocity profiles at x/C = 1.002, 1.009, 1.028, and 1.047 for $Re_C = 1.4$M, 4M, 17M, and 50M. The data are replotted from

Figs. 4 and 5, but here have been scaled as a plane wake: the horizontal axes are normalized by $\Delta U_{\max}$ where $\Delta U = U(y) - U_e^{ss}$, ($U_e^{ss}$ is the suction side wake-exterior horizontal velocity) and the vertical axes are $(y - y_{ctr})/y_{1/2}$, where y_{ctr} denotes the average of the vertical coordinates where $\Delta U = \Delta U_{\max}/2$. The full wake width, $2y_{1/2}$, is that measured at $\Delta U = \Delta U_{\max}/2$. These same coordinates were used for the mean flow profiles presented in Part I, wherein the values for y_{ctr}, $\Delta U_{\max}$, and $y_{1/2}$ are provided. On the right-most frames of Figs. 13 and 15, fluctuation profiles for the self-similar wake of a symmetric airfoil at $\mathrm{Re}_C \sim 10^4$ (Wygnanski et al. 1986) are plotted for comparison. The plane wake coordinates are effective in collapsing the fluctuation results between the two trailing edge geometries at $x/C = 1.002$ except for $\overline{u'^2}$ at $Re_C = 4$M (Fig. 13b). However, as the wakes evolve downstream, fluctuation profile variations between the two trailing edge geometries begin to increase, particularly at the lower two Re_C. Most striking is $Re_C = 4$M, for which the fluctuations associated with the pressure side shear layer grow more rapidly on Geometry II than on Geometry I. This is noteworthy because the normalized pressure side boundary layers are nearly independent of Re_C. and trailing edge geometry above $Re_C = 4$M. This unusual near wake behavior at $Re_C = 4$M with Geometry II is caused by increased vortex shedding in the near wake, a phenomenon linked to trailing-edge geometry and suction side shear rate in §5.1.

Use of wake coordinates in Figs. 13-15 also serves to emphasize Re-dependence in the foil's near wake evolution. Most notably at x/C=1.047, the normalized strength of the fluctuations decreases by more than a factor of two with increasing Re_C. While some of this variation is undoubtedly due to Re-dependence in the PIV spatial averaging (see §3.3, and Fig. 8), the remainder appears to be a genuine Re-effect. Furthermore, the present results at the lowest Re_C of this study (1.4M) are the best match with the prior measurements in a foil wake at

$Re_C \sim 10^4$. However, in all cases, the velocity-fluctuation and Reynolds-stress profiles have not achieved self-similar form by $x/C = 1.047$ (the furthest downstream location presented on Figs. 13-15) nor by $x/C = 1.11$ (the furthest downstream location at which such measurements were made, not presented here).

3.5 Near-wake velocity spectra

Based on the turbulence fluctuation results, vertical velocity spectra were measured in the foil's near wake to aid in identifying the relative contributions of nearly-periodic flow oscillations (vortex shedding) and more-nearly-random fluctuations (turbulence). Temporal spectra of v' were acquired at two downstream positions in the near wake using the LDV system. Spatial spectra of v' were computed from the PIV measurements along a line segment that passes through or near the temporal-spectra measurement points.

Figures 16 and 17 present the LDV-measured vertical velocity spectra in the foil's near wake at x/C=1.009 and 1.070, respectively, for Geometry I (Figs. 16a, 17a) and Geometry II (Figs. 16b, 17b) at Re_C = 1.4M, 4M, 17M, and 50M. The y-coordinate for each spectral measurement was chosen by searching for the maximum spectra peak height, at the given x/C, over the range $-0.025 < y/C < +0.025$. In all cases, the maximum spectral peak height, and maximum spectral peak area, were found in the immediate proximity of the pressure side shear layer with lesser spectral peaks typically associated with the suction side shear layer. The coordinates of the peak spectral activity are provided in Table 2 and are nearly coincident with the loci of maximum $\overline{v'^2}/U_o^2$, shown in Figs. 9 and 10. The temporal spectra, $\Phi_v(f)$, were normalized so that $\overline{v'^2}/U_o^2 \equiv \left(\Delta_y^{nom}/U_o\right)\int_{-\infty}^{+\infty}\tilde{\Phi}_v df$, where Δ_y^{nom} is a constant nominal wake thickness of $0.01C$, $\tilde{\Phi}_v(f)$ is the normalized spectra, and f is frequency in Hz. The dimensionless frequency on the horizontal axes on Figs. 16 and 17 may also be interpreted as a normalized wavenumber, $k\Delta_y^{nom} \equiv f\Delta_y^{nom}/U_o$. Only spectral values below the effective Nyquist frequency set by the LDV data rate are plotted. The data from Re_C = 50M was not as fully converged and was smoothed for graphical clarity. This smoothing had negligible effect on peak characteristics.

Figure 18 presents the PIV-measured vertical velocity spectra in the foil's near wake measured on the line segment from (*x*/*C*, *y*/*C*) = (1.000, 0.009) to (1.100, –0.005) for Geometry I (Fig. 18a) and Geometry II (Fig. 18b) at Re_C = 1.4M, 4M, 17M, and 50M. These spatial spectra, $\Phi_v(k)$, were computed from between 500 and 1000 PIV fields, and were normalized so that $\overline{v'^2}/U_o^2 \equiv \Delta_y^{nom}\int_{-\infty}^{+\infty}\tilde{\Phi}_v dk$, where $\tilde{\Phi}_v(k)$ is the normalized spatial spectrum, and *k* is the wavenumber in cycles/m^{-1}. Unfortunately, these spatial spectra are potentially contaminated at low wavenumbers by two factors that do not influence the low frequency portion of the temporal spectra. First, the foil's near wake lacks a statistically homogeneous direction in which to compute spatial spectra. And second, the limited spatial extent of the PIV data prevents adequate spectral estimation at the wavelengths typical of vortex shedding. Although these factors limit the utility of these spatial spectra in the study of vortex shedding, the spectra should be unbiased above $k\Delta_y^{nom} = 10^{-1}$ or so. The downward sloping lines on Figs. 16-18 have a slope of –5/3 and are provided for reference.

The vertical velocity spectra show several common features. At low frequencies ($f\Delta_y^{nom}/U_o$ less than ~0.1) both trailing edges produce flat spectral levels as *f* decreases. And, at high frequencies and wavenumbers ($f\Delta_y^{nom}/U_o$ and $k\Delta_y^{nom}$ greater than ~0.5) the expected power-law form for turbulent fluctuations is recovered within the limitations of the measurements. In between, every spectrum displays a peak – to greater or lesser degree – that is associated with the strength of vortex shedding. In the temporal spectral, these peaks occur at different normalized frequencies, with differing heights and widths, but always near the anticipated Strouhal number,

$St = f_p \Delta_y^{nom} / U_o \approx 1/2\pi$, for near-wake vortex shedding from foils and struts (Blake 1986). In particular, Geometry II produces higher spectral peaks than Geometry I at every Re_C, with the highest spectral peaks occurring at Re_C = 4M for both trailing edge geometries.

For graphical clarity, Figs. 16-18 show results from only four of the seven Re_Cs of this study. Using the parameters defined in Fig. 19, vortex-shedding-peak results from the temporal spectra at all seven Re_Cs are presented in Figs. 20 and 21 for x/C = 1.009 and 1.070, respectively. The last panel on these figures gives the frequency of the spectral peak, f_p, in the dimensionless form $2\pi St$. Some of the weaker spectral peaks lack a distinctive maximum so the frequency of the centroid of the peak was substituted for f_p in these cases. To ease comparisons between conditions, the normalized frequency $\tilde{f} \equiv f / f_p$ was used in all calculations leading to Figs. 20 and 21, so that $\overline{v'^2} / U_o^2 \equiv \int_{-\infty}^{+\infty} \tilde{\Phi}_v(\tilde{f}) d\tilde{f}$.

The Re_C and geometry dependencies noted on Figs. 16-18 are further evident in Figs. 20 and 21. The spectral peak for Re_C = 4M with Geometry II has the greatest magnitude and the minimum width. Comparison of Figs. 20 and 21 also reveals aspects of the downstream evolution of the wake. The peak height expressed in terms of the energy in the upstream velocity (the normalization depicted) is reduced at x/C = 1.070 in comparison to x/C = 1.009. However, peak height compared to the energy at all frequencies, obtained by dividing the peak values of panels (b) by the variance given in panel (a), is actually increased at x/C = 1.070 in comparison to x/C=1.009. This indicates that a greater fraction of the total fluctuations occur at the shedding frequency as the flow evolves downstream. This trend and the diminished fluctuation level suggests that smaller vortical structures are dissipated or progressively grouped into larger – and more slowly moving – wake-scale structures in the manner expected for a developing two-dimensional vortex street.

3.6 Trailing edge surface pressure spectra

The shedding trends in the wake velocity spectra agree with the independently measured temporal spectra, $\Phi_p(f)$, of surface pressure fluctuations on the trailing edge. Figure 22 presents results from a flush mounted dynamic pressure transducer located on the foil's pressure side at $x/C = 0.99$. These spectra are normalized in a manner similar to the velocity spectra: $\overline{p'^2}/Q_o^2 \equiv \Delta_y^{nom}/U_o \int_{-\infty}^{+\infty} \tilde{\Phi}_p df$, where $\tilde{\Phi}_p$ is the normalized spectrum, $Q_o \equiv \rho U_o^2/2$, and ρ is the density of water at 32 °C. The normalized variances computed from the integral of the power spectra are less than 0.0001 for $Re_C > 3M$ for both trailing edges. Each plotted spectrum on Fig. 22 was calculated from approximately 3 million data points, partitioned with 50% overlap to provide 376 spectral windows of 2^{14} (16,384) data points, with an estimated spectral amplitude uncertainty of +/-12% (Vetterling, *et. al.*, 1992). A linear least-squares fit was subtracted from each partition to remove any drift and to zero the partition mean. Neither acceleration contamination nor noise contributions have been removed from these spectra, and a 1/100th decade filter has been applied to clarify the high-frequency portion of these spectra (with negligible effect on peak magnitudes). The upward translation of the curves on Fig. 22 as Re_C falls below 8M reflects the increasing fraction of the transducer output resulting from noise that does not scale with Q_o. The diagonal lines below the data on Fig. 22 have slope of -1.

Two fluid dynamic phenomena are evident in the plotted pressure spectra. The surface pressure fluctuations produced by an attached turbulent boundary layer (TBL) lead to broadband unpeaked spectra (see Willmarth 1975, or Farabee and Casserella 1991) having a shallow spectral slope slightly above -1 (Goody 2002), and such a spectral signature is clearly evident in all the results on Fig. 22. In addition, pressure fluctuations induced by organized near wake vortex shedding lead to narrow spectral peaks at $f = f_p$, and such peaks are evident in the spectra measured for Geometry II. To be apparent, the vortex-shedding component must be stronger than the TBL fluctuations at the same frequency. The pressure spectra for Geometry I in Fig. 22a lack significant peaks, indicating that vortex shedding was not detectable above the TBL fluctuations. However, peaks in the pressure spectra are found with Geometry II for $Re_C \leq 8$M (see Fig. 22b), with a maximum detected shedding condition at $Re_C = 4$M. Even though the curve for $Re_C = 3$M on Fig. 22b is compromised by poor signal-to-noise and suffers from a strong noise peak near $f\Delta_y^{nom}/U_o = 0.06$, it does indicate a vortex shedding peak near the correct frequency. Pressure fluctuation data from speeds below $Re_C = 3$M are dominated by noise and are not presented. Overall, given the threshold effect of the TBL pressure fluctuations, these pressure spectra are fully consistent with the vertical velocity spectral results reported on Figs. 16-21.

3.7 Vortical flow features related to the velocity fluctuations

The spatial PIV velocity measurements allow the size, strength, and spacing of vortices in the foil's near wake to be investigated. Visualization of vortices and regions of shear flow may be achieved directly from computations of vorticity. However, for this presentation of results, the *swirling strength* (Zhou et al. 1996, 1999, Adrian et al. 2000) is used as a more selective method for visualization of vortices alone. Swirling strength, χ (with units of t^{-1}like vorticity), is the absolute value of the imaginary part of the eigenvalues of the two-dimensional velocity gradient tensor. It specifies the orbital rotation rate of a fluid element centered on the point of interest, but is zero in pure shear flow.

Figure 23 presents grayscale images of normalized swirling strength computed from selected instantaneous velocity fields for Geometry I at $Re_C = 4$M and for Geometry II at $Re_C =$ 1.4M, 4M, 17M, and 50M. Here clockwise rotation has been treated as positive (white). The requisite velocity derivatives are computed on a 1.6 mm grid from a central difference stencil of width 3.2 mm (the length scale of the PIV interrogation area). The swirling strength is then computed, spatially smoothed with a box-car filter of 3.2 mm x 3.2 mm, and thresholded to remove low-level values. To better visualize the weaker suction side swirling strength, the gray levels used in Fig. 23 are not symmetric about zero. In addition, the instantaneous fields chosen best illustrate the prevailing differences between the five test conditions shown. Only $Re_C = 4M$ is presented for Geometry I (Fig. 23a) because results at other Re_C for this geometry are similar in appearance. The instantaneous velocity field used to compute the swirling strength in Fig. 23c was also used to compute the vorticity of the field shown in Fig. 24a; note the similarity of these two fields for $x/C > 1.02$.

In Fig. 23 the frequency of the most energetic velocity fluctuations is apparent in the spacing of the largest pressure side vortices. For example, observe the three largest pressure side vortices for $Re_C = 4M$ with Geometry II in Fig. 23c. The streamwise spacing of the vortices at $x/C = 1.045$ and $x/C = 1.10$ is approximately $6\Delta_y^{nom}$, which gives the expected Strouhal number of approximately $1/2\pi$. The greater degree of organization at $Re_C = 4M$ for Geometry II (c) compared to Geometry I (a) at the same Re_C reflects the geometry dependence seen in the spectra of Figs. 16–18.

The Re-dependence of the Geometry II flow seen in the velocity spectra (Figs. 17b, 18b) is also evident in the swirling strength fields, Fig. 23b-e. Most obvious is the variation with Re in the streamwise spacing of the strongest pressure side vortices, a feature clearly linked to Re variation in St. The pressure side vortex spacing at $Re_C = 4M$ matches $2\pi St \sim 1$, while the other Re have more closely spaced vortices implying a $2\pi St > 1$. In particular, the $Re_C = 50M$ condition in panel (e) shows two predominant values of vortex spacing. Here, three groups of vortices have a spacing of several wake thicknesses, while vortices within these groups are spaced more closely. This closer spacing may reflect vortex roll-up on a length scale determined by the pressure side boundary layer instead of the larger wake length scale.

In addition, Fig. 23 shows near wake conditions for which the pressure-side time-averaged shear layers (Part I, Fig. 18) are very similar at the trailing edge but then go on to develop into different wake vortex distributions. For example at Re_C = 8M and 50M for Geometry II, the flow characteristic that differs most between these two conditions is the state of the suction-side shear layer at the trailing edge, which varies with Re_C because of Re-dependent suction-side boundary layer development. As a second example, the flows with Geometry I (Fig. 23a) and Geometry II (Fig. 23c) at Re_C = 4M have nearly identical pressure-side shear layers at the trailing edge and very similar suction side shear layers, yet these conditions also differ in pressure-side vortex distribution. In this case, the flow characteristic that differs most between the conditions is the wake thickness, as set by the different trailing edge geometries. These observations suggest that the suction side shear layer and the wake thickness both affect the roll-up of the pressure side shear layer into wake vortices.

4. Discussion: Analysis of Vortex Fields

The turbulence fluctuation profiles of the evolving wake display both Re and geometry dependencies, particularly in the vertical velocity fluctuations at the lower two Re_C. The spectra of the vertical velocity and of the trailing edge surface pressure fluctuations link this Re and geometry dependence to vortex shedding. PIV-acquired instantaneous swirling-strength fields confirm this connection. These facts motivate an analysis of the Re and geometry-dependence of the vorticity distributions in the wake and the relationship between identifiable vortices and velocity fluctuations. Specifically, the analysis presented here attempts to separate the near-wake dynamic contribution of strong large-scale vortices from the background of weaker smaller-scale turbulence. The goal of this effort is develop a physical model of vortex shedding that can indicate, or even predict, when near-wake vortex shedding will be strong. This analysis is based on: assessing of the mean flux of vorticity into the wake (§4.1), identifying vortices in the wake (§4.2), determining vortex characteristics (§4.3), establishing vortex locations (§4.4), and reconstructing velocity fluctuations from the identified vortices alone (§4.5). The physical model and the scaling laws derived from it are presented in §5.

4.1 Mean flux of vorticity into the wake

The vorticity in the wake comes from the foil's suction and pressure side boundary layers. Assuming a negligible correlation between instantaneous vorticity fluctuations and instantaneous foil-surface-tangent velocity fluctuations, the time-averaged circulation flux into the near wake may be computed from the time-averaged boundary layer profiles (see Fig. 2, and Part I Fig. 18). Here, the time-averaged flux of circulation is defined as $\dot{\Gamma} \equiv \int_0^{h_e} U_t \Omega dh$, where $\Omega = \partial U_t / \partial h$; Fig. 1 defines the surface-normal, h, and surface-tangent, t, coordinates; h_e specifies is the edge of the boundary layer; and U_t is the mean tangent velocity. The computed circulation fluxes are presented in Table 3 as ratios of the non-dimensional circulation flux, $\dot{\Gamma}^* / U_o^2$, at a given condition, normalized by the circulation flux value, $\dot{\Gamma}^* \equiv \left(\dot{\Gamma}^{ps} / U_o^2\right)_{Re_C = 4\text{M}}$, from the pressure side boundary layer for Geometry II at $Re_C = 4\text{M}$. The value of $\dot{\Gamma}^*$ is given at the bottom of Table 3. Unfortunately, the measured data were insufficient to estimate suction side circulations fluxes with Geometry II. Mismatch in the pressure and suction side circulation fluxes with Geometry I are presumed to be caused by the neglected velocity-vorticity fluctuation correlations and the fact that the suction side flux was calculated at x/C =0.93, well upstream of the foil's trailing edge.

Surprisingly, the strongest vortex shedding (Re_C = 4M) occurs with the lowest normalized pressure-side circulation flux for both trailing edges. For Geometry I, where suction-side data are available, the Re_C = 4M case does not have the lowest or the highest circulation flux. From these observations, it is concluded that circulation flux from the attached boundary layers is not by itself a predictor of the strength of vortex shedding. This conclusion holds even when the local external velocity, U_e, is used in lieu of U_o for normalization. This conclusion is reasonable because the magnitude of $\dot{\Gamma}$ accounts only for the amount of circulation entering the wake without addressing the distribution of that circulation. In the near wake, the circulation distribution will be determined by the characteristics of individual vortices and their spatial organization.

4.2 Vortex identification

Extracting vortex characteristics from the PIV field measurements involved several processing steps. First the PIV fields were sifted for strong vortices by computing the vorticity, ω, via centered spatial first differences (see §3.7), thresholding the computed vorticity magnitudes, identifying the remaining vorticity peaks as candidate vortices, and ranking these candidate vortices from highest to lowest vorticity magnitude. Then, starting with the strongest vorticity peak, each candidate vortex was assigned a radius by starting from its peak-vorticity location and repetitively computing the spatially-averaged vorticity within circles of increasing radius until the peak-divided-by-average vorticity ratio reached 1.77. When applied to an idealized vortex with a Gaussian vorticity distribution, $\omega(r) \equiv \omega_{\max} e^{-(r/\sigma)^2}$ and $\Gamma(r) = \omega_{\max}\pi\sigma^2(1-e^{-(r/\sigma)^2})$ with r as a radial coordinate, this method yields a core radius of

1.121σ, which is the radius at which the vorticity-induced velocity is maximum. After this core sizing was completed, the candidate vorticity peak was idealized as a Gaussian vortex having the same core diameter and far-field circulation. Before continuing on to the next candidate vortex, the vorticity put into the new idealized Gaussian vortex was subtracted from the PIV vorticity field and the threshold was reapplied to the remaining candidate vortices. In this way, field vorticity was not double-counted and multiple vorticity peaks in close proximity were absorbed into a single idealized vortex. For this procedure, the vorticity threshold was chosen to extract approximately 33% of the spatially-averaged vorticity magnitude at each flow condition. This threshold typically identified 15 to 20 vortices in a given PIV field.

Figure 24 illustrates this process. It shows an example of a raw vorticity field (a) and the results of the vortex identification scheme, presented as an idealized vorticity field (b). Comparison of Fig. 24a and b confirms that the strongest vortices have been appropriately located and sized. In the following section the statistics of the identified vortices will be used to explore the variations in the field vorticity distribution and its connection to the vertical velocity fluctuations.

4.3 Characteristics of individual vortices

The convection of vortices across the flow field will induce velocity fluctuations at any fixed point in the field. In two spatial dimensions, the magnitude of the induced velocity, $|\vec{u}|$, from a point vortex is given by the Biot-Savart law,

$$|\vec{u}| = \Gamma/(2\pi R), \tag{1}$$

where Γ is the circulation in the vortex, and R is the distance between the vortex center and the point of interest. Thus, the variables that control the induced velocity from a field of vortices include the size and strength of the each vortex and its location relative to the point of interest.

For the strong vortices identified by the procedure outlined in §4.2, the far-field circulation, Γ, and core diameter, $d = 2\sigma$, are shown as functions of downstream distance in Fig. 25 for Geometry I at $Re_C = 4\text{M}$ (a panel) and Geometry II at $Re_C = 1.4\text{M}$, 4M, 17M, and 50M (panels b-e). On both Figs. 25 and 26, a vertical dashed line indicates the location of the maximum vertical velocity fluctuations taken from Figs. 9a and 10a.

For all conditions, the vortices are largest in terms of both circulation and diameter nearest the trailing edge and reduce in strength and size downstream. Recall, however, that the vorticity within $1.00 < x/C < 1.02$ may be due both the swirling and shear flow, so vortex statistics there may be biased upward by the shear component. If the calculations leading to Fig. 25 are redone after excluding identified vortices with low swirling strength within their cores, the curves are shifted downward slightly at the trailing edge, but the trends remain the same. Beyond these common trends, two conditions in Figure 25 are distinctive. The flow at $Re_C = 1.4\text{M}$ with Geometry II (Fig. 25b) shows the greatest asymmetry in both vortex strength and size. This asymmetry is due to the transitional state of the pressure side boundary layer and fully turbulent state of the suction side boundary layer at this Re_C. All other conditions, which represent fully turbulent boundary layers from both sides of the foil, have greater symmetry. Interestingly at $Re_C = 4\text{M}$, vortex circulation for Geometry II exceeds that of Geometry I by a greater factor than that suggested by the ratios of mean circulation fluxes of Table 3.

Figure 26 presents the average location, and vertical separation, of the centers of the suction and pressure side vortices as a function of x/C along with the location of the maximum vertical velocity fluctuations taken from Figs. 9a and 10a (the panel layout on Fig. 26 is identical to that of Fig. 25). The vortex-center curves are not a path lines for individual vortices but they do indicate likely vortex trajectories. For all conditions, these vortex-center curves correspond well to the location of peak Reynolds shear stress shown in Figs. 11b and 12b. Here, both trailing edge geometries at $Re_C = 4$M display a greater downward slope in the vortex-center curves (Fig. 26a and c) than is seen at the other conditions.

In addition, the maximum vertical velocity fluctuations track the pressure-side vortex-center curves for all conditions except those at $Re_C = 4$M. The distance from the vortex-center curves to the location of maximum velocity fluctuations gives an indication of the relative contribution of the suction and pressure side vortices to the peak velocity fluctuations. Thus, it can be concluded from Fig. 26 that the pressure side vortices dominate the velocity field fluctuations away from the shedding condition, but that suction and pressure side vortices contribute more equally to the velocity fluctuations when shedding occurs. However, closest to the foil, $1.00 < x/C \leq 1.01$, the pressure side vortices are found to dominate for all conditions tested. Figure 26 also shows that the location of maximum vertical velocity fluctuations is typically found at the downstream location where the vertical vortex separation (or wake thickness) is smallest. This finding is consistent with the interpretation of this x-location as the vortex *street* formation length, where the vortices become well staggered and move into closer vertical proximity. Thus, in the remainder of this paper, the downstream distance from the trailing edge to the peak in vertical velocity fluctuations is referred to as the vortex street *formation length.*

4.4 Vortex street organization

From simple geometric considerations, the vertical velocity fluctuations in the middle of the near wake caused by suction and pressure side vortices are enhanced when these vortices are staggered – as in the classical Von Karman vortex street – and suppressed when they are vertically aligned. Thus, fields with the identical individual vortices may develop very different net vertical velocity fluctuations based on the arrangement or organization of the wake vortices.

Here vortex street organization was determined by conditionally averaging instantaneous vorticity fields based on the presence or absence of a pressure side vortex near $x/C = 1.05$. First, instantaneous vorticity fields with no pressure side vortex centered within a search window of $1.045 < x/C < 1.055$ were discarded, leaving typically half of the original field measurements. Then, the remaining fields were then shifted along the streamwise axis so that the pressure side vortex of greatest peak vorticity within the search window was centered on $x/C = 1.050$. Finally, these shifted fields were ensemble averaged. This conditional averaging technique, which is meant to mimic conventional phase averaging, relies solely on pressure side vortex identification, so any suction side structure found is indicative of vortex street organization.

Figure 27 displays the conditionally-averaged PIV-field results as normalized swirling strength using the same panel layout as Fig. 25. The black central feature in each panel of this figure represents the conditionally-selected (or reference) pressure-side vortex. The result in Fig. 27a for Geometry I at Re_C = 4M are similar to those at the other Re_C with this trailing edge geometry. Based on a comparison Fig. 27b-e, Geometry II at Re_C = 4M (Fig. 27c) produces the most clearly structured vortex street with a staggered arrangement of vortices. The pressure-side vorticity at Re_C = 1.4M (Fig. 27b) is almost as structured as that at Re_C = 4M, but the suction side vorticity is less coherent at the lower Re_C. Results at both of the higher Re_Cs (Fig. 27d and e) indicate little geometric coherence between pressure- and suction-side vorticity. The results shown in Fig. 27 objectively confirm the subjective assessments of relative organization made from the individual fields of Fig. 23. In addition, the vortex street at Re_C = 4M becomes well organized at the shedding frequency immediately downstream of the trailing edge so that it provides the most constant *St* with increasing downstream distance (see Figs. 20e and 21e).

4.5 Reconstruction of vortex-induced velocity fluctuations

To determine the extent to which the large vortices determine the vertical velocity fluctuations, an idealized velocity field was constructed from the Biot-Savart law (1) and the idealized vortices identified by the scheme described in §4.2. A sample vertical velocity field is shown on Fig. 24c, presented as the instantaneous vertical velocity minus the average. Just below it, Fig. 24d, is the reconstructed idealized vertical velocity for the same field. Working from the identified vortices, vertical velocity results similar to Fig. 24d may be generated separately for pressure (v_p) and suction (v_s) side vortices.

Using a combined Reynolds and vortex decomposition, $v = \bar{v} + v' = v_p + v_s$, the mean-square vertical velocity fluctuation can be determined in terms of suction and pressure side vortical velocity components.

$$\overline{v'^2} = \overline{v'^2_s} + \overline{v'^2_p} + 2\left(\overline{v_s v_p} - \bar{v}_s \bar{v}_p\right). \tag{2}$$

The last term in (2) gives the contribution from correlation of the suction and pressure side vortices and quantifies the impact of vortex street stagger or alignment. The results of the decomposition suggested in (2) are shown in Fig. 28 with the same panel layout as Fig. 25. The separate contributions are from the suction side vortices (solid line), pressure side vortices (dashed line), and the correlation term (dotted line). Total vortex-induced fluctuations are also shown (dash-dot-dot line). The symbols denote the PIV-measured vertical velocity fluctuations (from Figs. 9b and 10b). A comparison of the total idealized fluctuations to the actual fluctuations for Geometry II shows the relative contribution of the identified vortices to the overall fluctuation levels. The peak fluctuation levels are well-matched, and the trends with downstream distance are similar. This confirms that the induced velocities from the largest vortices are the primary factor in setting near-wake vertical-velocity fluctuation levels. This type of field reconstruction is less effective with Geometry I where the measured vorticity is less coherent.

The qualitative trend with Re and trailing-edge geometry in the location of maximum fluctuations (formation length) is captured by the reconstructed fields. The formation length is shortest for Geometry II at $Re_C = 4$M (c) and increases for the other conditions. In all cases, the agreement between the actual and reconstructed fluctuations is improved by lowering the vortex peak threshold, thereby increasing the fraction of field vorticity included in the identified vortices. A lower vorticity threshold is of particular benefit for the $Re_C = 1.4$M case which has the greatest asymmetry between the suction and pressure side vorticity. Here, as the threshold is reduced, more suction side vorticity is captured with little change to the identified pressure side vorticity. The net effect of the added vorticity is an increase in the formation length in the reconstructed fields.

The vortex decomposition shown on Fig. 28 also confirms that the pressure side vortices are the main contributors at the vertical velocity fluctuation maximum. The x/C location of peak vertical velocity fluctuations coincides in all cases with the peak in the contribution of the pressure side vortices, and in no cases corresponds to the peak in suction side contributions. However, for $Re_C = 4$M, the suction side contributions and their correlation with the pressure vortices side do play a secondary but significant role. The highest total fluctuations occur at $Re_C = 4$M with Geometry II, even though the highest pressure side fluctuations occur at $Re_C = 1.4$M.

5. Discussion: Prediction and Scaling of Vortex shedding

The prior analysis of PIV fields shows that vertical velocity fluctuations near the trailing edge are primarily due to the pressure side vortices. The distribution of the pressure side vortices appears connected to the suction side shear layer properties and the wake thickness. In this section this connection is put on a quantitative footing. The vertical velocity induced at the trailing edge by the suction side vortices is presumed to drive perturbations of the unstable pressure side shear layer and influence its roll-up on the wake-thickness scale. The pertinent properties of the suction side vortices are tied to parameters from the suction-side mean flow. The physical model and the proposed scaling law are presented in the next subsection (§5.1), which is followed by short discussions of the roles of suction (§5.2) and pressure (§5.3) side mean shear rate, predictive application of the proposed scaling law (§5.4), and the potential for wake instability concepts to explain the findings of this study (§5.5).

5.1 Shedding strength and suction side mean shear

The measurements reported here are consistent with a physical model of vortex shedding that correlates the Biot-Savart induced vertical velocity at the trailing edge and the roll-up into vortices of the pressure side shear layer. Consider the idealized vortex street depicted in Fig. 29. The suction side flow is best expressed in streamline coordinates, which are well approximated by the *h-t* Cartesian frame (Fig. 1) aligned to the suction side surface tangent at $x/C = 0.93$. The corresponding streamline coordinates for the pressure side are simply identical to the tunnel *x-y* coordinate frame. On Fig. 29, the hydrofoil is depicted with suction and pressure side external mean velocities U_{te}^{ss} and U_{e}^{ps}. The center lines of the suction and pressure side shear layers are indicated with dashed lines and the characteristic convection velocities of these shear layers are denoted U_{s}^{ss} and U_{s}^{ps}, respectively. The vortices of alternating sign, which form the vortex street, are shown as gray circles, and the vertical distance from the suction side vortices to the pressure side shear layer at the trailing edge is denoted Δ_y. The instant in the shedding cycle shown is the time of pressure side vortex roll-up at the trailing edge. The suction side vortex with contribution, v^{ω}, to the induced vertical velocity at the trailing edge is acting with clockwise circulation, Γ, at distance R. This vortex is presumed to dominate the flow fluctuations at the trailing edge at the instant shown. The perturbation from this vortex on the pressure side shear layer at the trailing edge is represented by the ratio of the induced vertical velocity to the streamwise velocity of the shear layer. From (1), this ratio can be approximated as:

$$\frac{v^{\omega}}{U_s^{ps}} \approx \frac{\Gamma}{2\pi R U_s^{ps}} \cos\theta \qquad (3)$$

The circulation (strength) of the suction side vortex can be approximated by the mean suction-side circulation flux passing the trailing edge in one shedding cycle, integrated over a vertical distance Δ_y and centered on the suction side shear layer: $\Gamma \approx \left[\left(dU_t/dh \right)^{ss} U_{ts}^{ss} \Delta_y \right] / f_p$. The appropriate mean velocity gradient, $\left(\partial U_t / \partial h \right)^{ss}$, and convection velocity, U_{ts}^{ss}, are those values characteristic of the center of the mean suction side shear layer. In this approximation, the correlation between instantaneous vorticity fluctuations and velocity fluctuations in the shear layer are assumed negligible in comparison to the product of their means. This circulation flux does not reflect the total flux available from the attached suction side boundary layer, but instead the lesser amount residing near the shear layer centerline at the trailing edge. For the flows of this study, $R \sim \Delta_y$ and $\theta \approx \pi/4$ for the moderately and weakly shedding conditions, though occasional instantaneous fields with zero θ were observed for the strongest shedding conditions. Overall, variation in θ between conditions was weak, so for simplicity, θ can be treated as a constant and (3) becomes:

$$\frac{v^{\omega}}{U_s^{ps}} \propto \frac{(dU_t/dh)^{ss}}{2\pi f_p}\frac{U_{ts}^{ss}}{U_s^{ps}} \tag{4}$$

When the shear layer velocity profiles are of similar shape, the external and shear layer velocities should be proportional, $U_{te}^{ss}/U_e^{ps} \approx U_s^{ss}/U_s^{ps}$. This, and the further simplification, $U_{te}^{ss} \approx U_e^{ps} \approx U_o$, allows (4) to be adjusted and cast in terms of *St*:

$$\frac{v^{\omega}}{U_o} \propto \frac{1}{2\pi St}\frac{(dU_t/dh)^{ss}}{U_o/\Delta_y}, \tag{5}$$

where $2\pi St \approx 1$ for the flows of this study. The scaling suggested by (5) relates of v^{ω}/U_o to a dimensionless suction-side shear rate, $(dU_t/dh)^{ss}/(U_o/\Delta_y)$. This parameter can be calculated from the mean velocity profiles at the foil's trailing edge (see Part I, Fig. 18). Here $(dU_t/dh)^{ss}$ was calculated as the average velocity gradient from 3.2 mm below to 3.2 mm above the vertical coordinate of peak streamwise velocity fluctuations along the line A-B shown in Fig. 29. Figure 30 shows the resulting values of $(dU_t/dh)^{ss}/(U_o/\Delta_y^{nom})$ vs. Re_C for Geometry I (a) and Geometry II (b). For both geometries, the dimensionless shear rate peaks at Re_C = 4M, the maximum shedding strength condition.

The form of right side of (5) is similar to the shedding-strength parameter b/δ^* suggested in Blake (1986), where *b* is the vertical thickness of the body and δ^* is the average of the suction and pressure side boundary-layer displacement thicknesses. Based on a review of experimental data up through the early 1980's, strong vortex shedding was found to occur when $b/\delta^* \geq 0.3$ for turbulent flow airfoils (Re_C near or above approximately 2M). The present results provide a refinement of these ideas for higher Re_C.

As the flow evolves beyond the instant shown on Fig. 28, the velocity ratio v^{ω}/U_o sets the input perturbation level to the Kelvin-Helmholtz instability of the pressure side shear layer.

Such instabilities have been found active in other separated turbulent flows (Song and Eaton, 2002). Therefore, the strength of large near-wake vortices formed at the shedding frequency should increase when this ratio increases. Here, the strength of vortex shedding is quantified from the measured peaks in the LDV-acquired near-wake velocity spectra at x/C=1.009 (see Figs. 16, 17 and 19-21). The advantage of this choice for shedding strength is that it allows comparisons with the results of Blake (1984) for minimally lifting struts.

The parameters of the vertical-velocity spectral shedding peaks are plotted against the dimensionless shear-rate parameter of (5) with $2\pi St = 1$ in Fig. 31. Here, the wake thickness, Δ_y (indicated on Fig. 29), is the measured vertical distance between the suction side Reynolds stress peak at x/C=1.009 and the pressure side Reynolds stress peak at $x/C = 1.002$. For this definition, the wake thicknesses for Geometry I are 0.0085C at Re_C = 3M, 0.0080C at Re_C = 4M, and 0.0090C at the remaining Re_C. The wake thicknesses for Geometry II are 0.0095C at all Re_C. The separate panels of Fig. 31 show normalized peak height (a), normalized peak width (b), and the fraction of total spectral area found under the peak (c), and the total spectral area (d). Results from Geometry I and II are shown as black and open circles, respectively, with one exception. The datum on each panel from Geometry I at Re_C = 1.4M is depicted as a black square to represent its disparity of pressure-side boundary separation upstream of the trailing edge. The gray filled triangles in Fig. 31a are data from three minimally lifting struts (Blake 1984) at $Re_C \sim$ 2M, two having rounded suction side trailing edge bevels of 25° and 45°, and a third having a sharp trailing edge bevel of 25°. In these strut studies, the boundary layers were tripped near the leading edge and spectral measurements were made with hot wire anemometry approximately 2.5Δ_y downstream of the various trailing edges (compared to ~1.0 Δ_y for this study). A zero shedding strength is presumed for the two 25° edges based on the absence of peaks in their reported surface pressure spectra. The error bars for the 25°-edge data points (plotted at the bottom of Fig. 31) are omitted for graphical clarity, but are similar to that shown for the 45° edge.

Figure 31a and c show that vortex shedding strength measurements collapse well when plotted against the dimensionless suction-side shear rate. Data from Geometry I and II, as well as minimally-lifting struts, are consistent with a single trend. The rapid increase in the shedding strength at a dimensionless shear rate of unity is due both to an increase in vortex strength and to a reduction in the formation length itself. These combined effects are nonlinear, and no physical basis is proposed for the functional forms of the curve fits given in the caption of Fig. 31.

The proposed role of the induced vertical velocity at the trailing edge is consistent with the established characteristics of vortex shedding. First, trailing edge motion, which increases the trailing edge vertical velocity ratio, has been shown to enhance vortex shedding and decrease the formation length in wind tunnel tests of a strut with a beveled trailing edge at $Re_C \sim 1\text{M}$ (Greenway and Wood 1973). Second, the use of splitter plates (Roshko 1955, Morkovin 1964, Bearman 1965) and base bleed (Bearman 1967, Wood 1967) are known to reduce vortex shedding, and modification of the vertical velocity ratio at the trailing edge may be the mechanism behind these effects. Finally, Kuethe (1972) showed for both a flat plate and a lifting surface at Re_C approaching 1M, that the diversion of a portion of the boundary layer vorticity into streamwise vortices (by a wave-like static surface feature) suppressed vortex street development in the near wake. Such streamwise vortices may disrupt vortex shedding by destroying spanwise coherence of the vertical velocity ratio at the trailing edge.

5.2 Pressure side mean shear and vortex shedding

It is surprising that the scaling embodied in (5) and illustrated in Fig. 31a and c lacks variables connected to the pressure side shear layer since trailing-edge vortex shedding might reasonably be expected to depend, in general, on the properties of both shear layers. One possible explanation involves the more downstream location of pressure side separation in the flows studied here. The roll-up of the suction side shear layer initiates well upstream of trailing edge. Thus, The more fully formed suction side vortices may dominate the interaction between the two shear layers at the trailing edge. A second explanation follows from the lack of variation in the foil's pressure-side shear layers in this study; the pressure side circulation flux only varies by 14% across all conditions, and only 3% across the conditions with $Re_C > 2$M. If the effect of the pressure side variables were weak in comparison to those of the suction side for the geometries studied, small variations caused by pressure side characteristic changes might go undetected. Only early pressure side separation at $Re_C = 1.4$M appears to have influence on the shedding characteristics shown on Fig. 31. However, pressure side variables are expected to increase in importance for more symmetric foils, or when suction and pressure side separation points and initial shear layer conditions are more similar.

5.3 Suction-side mean shear and wake frequency selection

The scaling presented by (5) suggests that near the trailing edge, there exists a negotiation between the suction and pressure side shear layers to determine whether or not the pressure side shear layer will respond at a forcing frequency set by the suction side. When the both sides agree on the frequency, there is strong shedding, such as $Re_C = 4$M with Geometry II. When the two shear layers initially disagree, vortex street formation may be delayed or even suppressed. When strong near-wake fluctuations are absent, the near-wake shear layers tend to roll up on length scales set by the separating boundary layers (Morris and Foss 2001). Such small-scale roll-up is evident in a flow visualization of Prasad and Williamson (1997) for a cylinder with vortex shedding at $Re_d = 10^4$, on which the shear layers roll up first on the smaller boundary layer scale, and then further downstream location on the larger wake scale. This phenomenon is also evident for Geometry II flow at Re_C = 50M where the preferential frequency in the initial pressure side shear layer roll up is higher than the expected vortex-shedding Strouhal frequency. However, the suction and pressure side shear layers remain so ill-matched that significant wake-scale vortex organization does not occur upstream of $x/C = 1.10$. These observations suggest that near-wake symmetry is important in setting the vortex shedding strength, and the strongest shedding case found in these studies does occur when the mean velocity profiles at $x/C = 1.002$ are most symmetric. However, both shear layers are in general turbulent so the suction side layer must have enough time to form a sufficiently strong vortex to convince the pressure side shear layer to cooperate. Strong vortex shedding cannot occur at faster rate than this because the suction side vortices cannot accumulate enough vorticity to be strong enough. Shedding does not occur at a much slower rate either because the near wake vortices must be near enough to each other to interact, but they accelerate rapidly away from the trailing edge as they leave the separated flow region and cannot interact if formed too infrequently. Thus, a fluid-dynamic compromise between suction-side shear-layer influence and pressure-side shear-layer response appears to determine the dominant roll-up frequency at the trailing edge, $St \sim 1/2\pi$.

5.4 Predictive application of the shedding-shear correlation

Of the forms investigated, the dimensionless shear rate in (5) provides the best compromise between collapse of the vortex shedding data and potential for predicting vortex shedding at untested flow conditions.

From Fig. 31a or c, vortex shedding is predicted to occur when:

$$\frac{(dU_t/dh)^{ss}}{U_o/\Delta_y} \geq 0.8 \qquad (6)$$

This equation can be used to form predictions if the mean suction side shear rate and wake thickness can be estimated from the flow speed and the foil's size and trailing edge geometry. Although potential flow and boundary layer integral calculations, or even Reynolds-averaged Navier-Stokes (RANS) computational fluid dynamics (CFD) calculations may be nearly up to this task, the main problem with using (6) in a predictive fashion is that $(dU_t/dh)^{ss}$ is influenced by the presence or absence of vortex shedding. However, vortex shedding tends to decrease $(dU_t/dh)^{ss}$ so it will tend to be overpredicted by any calculation scheme that cannot itself predict vortex shedding. Thus, any flow solution – perhaps obtained from a RANS model – that potentially captures the relevant physics of the weakly shedding cases might be used with (6) and/or Fig. 31 to estimate an upper bound on the strength of vortex shedding in the actual flow.

5.5 Wake instability

Stability theory potentially offers an alternative means to explain the importance of the suction side mean shear and the observed differences in vortex street formation length. The strongest shedding case is also the condition with wake-scale vortex organization nearest to the trailing edge. This may reflect a state of absolute instability in the underlying flow, where wake scale disturbances are able to travel upstream and attach themselves to the foil's trailing edge. However, a stability analysis starting from the trailing-edge mean-velocity profiles was beyond the scope of this work, but it is a possible next step toward elucidating the role of the suction- and pressure-side mean shear in vortex shedding.

6. Summary and Conclusions

An extensive experimental investigation of the dynamic flow in the near wake of a two-dimensional hydrofoil at low Mach number and high Reynolds number is presented in this paper. The LDV, PIV and surface dynamic pressure measurements reported here were focused on understanding the unsteady flow in the foil's trailing edge region where near wake vortex shedding occurs. Results for chord based Reynolds numbers from 1.4 million to 50 million are reported for two trailing edge shapes have 44° and 56° apex angles. This effort has lead to four main conclusions.

First of all, the profiles of turbulent fluctuations through the near wake are Reynolds number dependent because of the varying strength of structured near-wake vortex shedding, even at the Reynolds numbers of this study that reach those of full-scale aero- and hydrodynamic lifting surface applications. The relative strength of the vortex shedding was found to depend on trailing edge geometry as well. This conclusion is drawn from the statistical, spectral, and instantaneous field results shown on Figs. 2-5, 9-18, 22-24 and 27.

Second, strong vortices from both the suction and pressure side shear layers are organized into a staggered vortex street that dominates the near wake fluctuations when vortex shedding occurs. This conclusion is based on the conditionally-averaged vorticity field results and the relative success of using a finite and countable number of idealized vortices to reconstruct the measured vertical velocity fluctuations in the foil's near wake (see Figs. 24, 27 and 28). However, when shedding is weak or absent, pressure side vortices dominate the fluctuations in the foil's near wake and there is little or no prevalent geometrical structure of wake vortices.

Third, the amplitude and frequency content of vertical velocity fluctuations at the foil's trailing edge appear to control the strength of near-wake vortex shedding. This finding is consistent with the near-wake dynamics in the current measurements and with past shedding enhancement and suppression techniques.

And finally, the proposed scaling for vortex shedding strength based on the mean suction-side shear rate, the upstream velocity, and the wake thickness is successful throughout the Re_C parameter range of this study for both trailing edge geometries, and is consistent with prior studies at lower Reynolds number on minimally lifting struts with asymmetric trailing edges. Although this shedding strength scaling relies on measured parameters, it may be possible to use it with mean-flow CFD calculations to predict an upper bound on vortex shedding strength.

In summary, the experimental results presented in this paper, together with those presented in Part I, provide new insights into the relationships between the various steady and unsteady flow phenomena on a two-dimensional but application-relevant lifting surface at high Reynolds number. These experimental results also provide a unique dataset for the development and validation of scaling laws and computational models for wall-bounded high-Reynolds number flows

Acknowledgements. The authors of this paper wish to the acknowledge the contributions of Shiyao Bian, Carolyn Judge, and Kent Pruss of the University of Michigan; William Blake, Michael Cutbirth, Ken Edens, Bob Etter, Ted Farabee, Jon Gershfeld, Joe Gorski, Tom Mathews, David Schwartzenberg, Jim Valentine, Phil Yarnall, Joel Park, and the LCC technical staff from the Naval Surface Warfare Center - Carderock Division; and Pat Purtell and Candace Wark from the Office of Naval Research, Code 333, which supported this research under contract numbers N00014-99-1-0341, and N00014-99-1-0856.

References

ADRIAN, R. J., K. T. CHRISTENSEN, LIU, Z.-C. 2000 Analysis and interpretation of instantaneous turbulent velocity fields. *Exper. in Fluids* **29**, 275-290.

BEARMAN, P. W. 1967 The effect of base bleed on the flow behind a two-dimensional model with a blunt trailing edge, *The Aeronautical Quarterly*, August.

BEARMAN, P.W. 1965 Investigation of the flow behind a two-dimensional model with a blunt trailing edge fitted with splitter plates, *J. Fluid Mech.* **21**, 241-255.

BLAKE, W.K. 1975 A statistical description of the pressure and velocity fields at the trailing edges of flat struts, *Report No. 4241*, David Taylor Naval Ship Research and Development Center, Bethesda, MD.

BLAKE, W. K. 1984 Trailing Edge Flow and Aerodynamic Sound, Parts 1 and 2, *Report DTNSRDC-83/113*, David Taylor Naval Ship Research and Development Center, Bethesda, MD.

BLAKE, W.K. 1986 *Mechanics of Flow Induced Sound and Vibration, Vol. 2,* Academic Press, Orlando, Chap. 11.

BLAKE, W.K., & GERSHFELD, J.L. 1989 Aeroacoustics of trailing edges, in *Frontiers in Fluid Mechanics* edited by M. Gad-el-Hak Springer-Verlag, Berlin, 457-532.

BOLDMAN, D. R., BRINICH, P. F., & GOLDSTEIN, M. E. 1976 Vortex shedding from a blunt trailing edge with equal and unequal mean velocities, *J. Fluid Mech.* **75**, 721-735.

BOURGOYNE, D.A. HAMEL, J.A., CECCIO, S.L., AND DOWLING, D.R. 2003 Time averaged flow over a hydrofoil at high Reynolds number, in press for *J. Fluid Mech.*.

CICATELLI, G., & SIEVERDING, C. H. 1995 A review of the research on unsteady turbine blade wake characteristics, *AGARD PEP 85th Symposium on Loss Mechanisms and Unsteady Flows in Turbomachines*, Derby, UK, May 8-12.

CICATELLI, G., & SIEVERDING, C. H. 1996 The Effect of Vortex Shedding on the Unsteady Pressure Distribution Around the Trailing Edge of a Turbine Blade, *ASME Paper* 96-GT-39.

FARABEE, T.M., & CASERELLA, M. J. 1991 Spectral features of wall pressure fluctuations beneath turbulent boundary layers. *Phys. Fluids A* **3**, 2410-2420.

GERRARD, J. H. 1966 The mechanics of the formation region of vortices behind bluff bodies, *J. Fluid Mech.* **25**, part II, 401-413.

GOODY, M. 2002 An empirical spectral model for surface pressure fluctuations that includes Reynolds number effects. AIAA paper no. 2002-2565.

GREENWAY, M. E. & WOOD, C. J. 1975 The effect of a beveled trailing edge on vortex shedding and vibration. *J. Fluid Mech.* **61**, 322-335.

HO, Y.-H., & LAKSHMINARAYANA, B. 1997 Computation of unsteady flow field over a hydrofoil, including boundary layer and wake, *AIAA Journal* **35**, 40-50.

HOWE, M.S. 1999 Trailing edge noise at low Mach numbers, *J. Sound Vib.* **225**, 211-238.

HOWE, M.S. 2000 Trailing edge noise at low Mach numbers part 2: Attached and separated edge flows, *J. Sound Vib.* **234**, 761-765.

HUERRE, P. & MONKEWITZ, P. A. 1990 Local and global instabilities in spatially developing flows. *Ann. Rev. Fluid Mech.* **22**, 473-538.

KNIGHT, C. J. & PELTIER, L. J. 1997 2-D steady wake predictions for airfoil cascades with beveled trailing edges. *AIAA Paper 97-0077.*

KUETHE, A. M. 1972 Effect of streamwise vortices on wake properties associated with sound generation. *J. Aircraft* **9**, no. 10, 715-719.

LOTFY, A. & ROCKWELL, D. 1993 The near-wake of an oscillating trailing edge: mechanisms of periodic and aperiodic response. *J. Fluid Mech.* **251**, 173-201.

LURIE, E.A., KEENAN, D.P., & KERWIN, J.E. 1998 Experimental study of an unsteady separating boundary layer. *AIAA J.* **36**, 565-570.

MANOHA, E., TROFF, B., & SAGAUT, P. 2000 Trailing-edge noise prediction using large-eddy simulation and acoustic analogy. *AIAA J.* **38**, no. 4, 575-583.

MINNITI, R. J. & MUELLER, T. J. 1998 Experimental Investigation of Unsteady Aerodynamics and aeroacoustics of a thin airfoil. *AIAA J.* **36**, no. 7, 1149-1156.

MORKOVIN, M. V. 1964 Aerodynamic loads on bluff bodies at low speeds. *AIAA J.* **2,** no. 11.

MORRIS, S.C. and FOSS, J. 2001 "Turbulent boundary layer to single stream shear layer," *Bulletin of the American Physical Society* **46**, No. 10, 134.

OERTEL, H., JR. 1990 Wakes behind blunt bodies. *Ann. Rev. Fluid Mech.* **22**, 539-564.

PRASAD, A., & WILLIAMSON, H. K. 1997 The instability of the shear layer separating from a bluff body. *J. Fluid Mech.* **333**, 375-402.

ROGER, M. & MOREAU, S. 2002 Trailing edge noise measurements and predictions for subsonic loaded fan blades. *8th AIAA/CEAS Aeroacoustics Conference and Exhibit*, 17-19 June, Breckenridge, CO, *AIAA Paper 2002-2460.*

ROSHKO, A. 1955 On the wake and drag of bluff bodies. *J. Aero. Sci.*, **22**, 124-132.

ROWE, A., FRY, A. L. A., MOTALLEBI, F. 2001 Influence of boundary layer thickness on base pressure and vortex shedding frequency. *AIAA J.* **39**, no 4, Tech. Notes.

SIEVERDING, C. H., & HEINEMANN, H. 1990 The influence of boundary layer state on vortex shedding from flat plates and turbine cascades. *J. of Turbomach.* **112**, 181-187.

SONG, S. AND EATON, J.K. 2002 Reynolds number effects on a turbulent boundary layer with separation , reattachement, and recovery. Report No. TSD-146 (Mech. Eng. Dept., Stanford University, Stanford, Ca.)

SWALES, C. & LOWSON, M.V. 1997 Aero-acoustic study on a NACA 0012 airfoil. *AIAA Paper 97-0509.*

UBALDI, M., ZUNINO, P. 2000 An experimental study of the unsteady characterisitics of the turbulent near wake of a turbine blade. *Exper. Therm. Fluid Sci.* **23**, 23-33.

UBALDI, M., ZUNINO, P., CAMPORA, U., & GHIGLIONE, A. 1996 Detailed velocity and turbulence measurements of the profile boundary layer in a large scale turbine cascade. *ASME International Gas Turbine & Aerospace Congress and Exposition*, Birmingham, UK, *Paper No. 96-GT-42.*

VETTERLING, W. T., TEUKOLSKY, S. A., PRESS, W. H., & FLANNERY, B. P. 1992 In *Numerical Recipes in C*, Second Edition, Cambridge University Press, Cambridge, UK.

WANG, M. & MOIN, P. 2000 Computation of trailing-edge flow and noise using large-eddy simulation. *AIAA J.* **38**, 2201-2209.

WANG, M. & MOIN, P. 2002 Dynamic wall modeling for large-eddy simulation of complex turbulent flows. *Phys. Fluids* **14**, 2043-2051.

WILLMARTH, W.W. 1975 Pressure fluctuations beneath turbulent boundary layers. *Ann. Rev. Fluid Mech.* **7**, 13-38.

WOOD, C. J. 1967 Visualization of an incompressible wake with base bleed. *J. Fluid Mech.* **29**, part 2, 259-272.

WYGNANSKI, I., CHAMPAGNE, F., & MARASLI, B. 1986 On the large scale structures in two-dimensional small-deficit, turbulent wakes. *J. Fluid Mech.* **168**, 31-71.

ZHOU, J., ADRIAN, R. J., BALACHANDAR, S. 1996 Autogeneration of near wall vortical structures in channel flow. *Phys. Fluids* **8**, 288-290.

ZHOU, J., ADRIAN, R. J., BALACHANDAR, S., KENDALL, T.M. 1999 Mechanisms for generating coherent packets of hairpin vortices in channel flow. *J. Fluid Mech.* **387**, 353-359.

Tables

Table 1. Line and Symbol Types for Flow Speeds and Re_C Values

U_o m/s	Re_C (millions)	Symbol/Line-type
0.5	1.4	– – – – ■ – – – –
1.5	4	———▲———
3.0	8	—·—·—·▼—·—·—·—
6.0	17	- - - - - ▶ - - - - -
12.0	33	·········◀·········
18.3	50	—··—··●—··—··

Table 2. y/C Spectral Measurement Locations of the LDV Focal Volume

Re_C	$x/C = 1.0094$		$x/C = 1.0703$	
(millions)	Geometry I	Geometry II	Geometry I	Geometry II
1.4	0	0.0023	–0.0046	–0.0094
2	0	0.0023	–0.0023	–0.0046
3	0.0023	0.0023	–0.0023	–0.0023
4	0.0023	0.0023	0	–0.0023
8	0.0023	0.0023	0	0
17	0.0023	0.0023	0	0
50	0.0023	0.0023	0	0

Table 3. Boundary Layer Circulation Fluxes at Separation

Re_C	*Suction Side:* $\dot{\Gamma}^{ss}/\dot{\Gamma}^*$		*Pressure side:* $\dot{\Gamma}^{ps}/\dot{\Gamma}^*$	
(millions)	Geometry I	Geometry II	Geometry I	Geometry II
1.4	1.46	–	1.01	1.08
4	1.45	–	0.97	**1.00**
17	1.35	–	1.03	1.02
50	1.36	–	1.05	1.05

$$\dot{\Gamma}^* = \left(\dot{\Gamma}^{ps}/U_o^2\right)_{Re_c=4\mathrm{M}} = 0.400$$

Figure Captions

Figure 1. (a)The cross section of the Geometry I hydrofoil with chord and max thickness indicated. The chord length given is the idealized value, measured to the vertex of the trailing edge apex angle. This point is defined as (x/C, y/C) = (1, 0) in the tunnel coordinate system: x-axis parallel to streamwise axis of the tunnel, and *y*-axis vertical. Also depicted is the hydrofoil coordinate system, for which the *t*-axis is taken as the local surface tangent and the *h*-axis is the local surface normal. (b) Trailing edge details showing Geometry I and Geometry II. The 0.4-mm radius, applied to the trailing edge tip, is not depicted. The dashed line indicates the direction of the surface tangent at x/C=0.930.

Figure 2. LDV-measured boundary layer characteristics at $x/C = 0.93$ and $Re_C = 1.4$M, 4M, 17M, and 50M on the (a) suction and (b) pressure side surfaces of the Geometry I hydrofoil. Panels show the normalized mean velocity components, velocity fluctuation variances, and Reynolds shear stress, all in the tunnel coordinate frame. Symbols are defined in Table 1. No data are available at the lower two Re_C on the pressure side.

Figure 3. LDV-measured separating boundary layer and near-wake fluctuations for Geometry I at $Re_C = 8$M and 50M, presented as normalized (a) streamwise fluctuations $\overline{u'^2}/U_o^2$, (b) vertical fluctuations $\overline{v'^2}/U_o^2$, and (c) Reynolds shear stress, $\overline{u'v'}/U_o^2$. The trailing edge geometry is depicted in the left half of each the frame. Vertical gray lines are shown at the x/C coordinate of the measurements and provide the vertical axis for plotted profile. The scale used to set the horizontal extent of each profile is provided in the bottom-left corner of the frame. Symbols are defined in Table 1. The velocity profiles are terminated at the locations of 99% boundary layer or wake thickness(es). Results from $Re_C = 17$M and 33M are omitted for clarity but fall monotonically between the data presented.

Figure 4. PIV-measured separating boundary layer and near-wake fluctuations for Geometry I at $Re_C = 1.4$M, 4M and 50M, presented in format similar to Fig. 3. Data are presented at x/C=1.002 in lieu of x/C=1.000. Line types are defined in Table 1. Data at Re_C=1.4M were not available at the downstream station.

Figure 5. PIV-measured separating boundary layer and near-wake fluctuations for Geometry II $Re_C = 1.4$M, 4M and 50M, presented in the format of Fig. 3. Data at $Re_C = 50$M was not available at the three upstream stations.

Figure 6 Convergence history for the PIV measurements at $(x/C, y/C) = (1.0094, 0.0080)$ in the near wake with Geometry I at $Re_C = 50$M. Here, N is the number images used to compute the normalized mean velocity components (a), and velocity variances and and Reynolds shear stress (b).

Figure 7. Comparison of velocity variances and Reynolds shear stress at x/C=1.0094 with Geometry I at Re_C= 50M between LDV-measured results (●) and PIV-measured results (——).

Figure 8. Ratio of LDV-measured to PIV-measured velocity variances and Reynolds shear stresses measured by at x/C=1.0094 with Geometry I at Re_C=17M, 33M, and 50M. Data at Re_C= 8M are unavailable. Streamwise velocity variance ratio —■— $\overline{u'^2}_{LDV}/\overline{u'^2}_{PIV}$; vertical velocity variance ratio —▲— $\overline{v'^2}_{LDV}/\overline{v'^2}_{PIV}$; Reynolds shear stress ratio —●— $\overline{u'v'}_{LDV}/\overline{u'v'}_{PIV}$.

Figure 9. Loci of maximum vertical velocity variance at Re_C = 1.4M, 4M, 17M, and 50M, taken from Fig. 4 for Geometry I (a), and vertical velocity variance values at these loci (b).

Figure 10. Same as Fig. 9 except these data are for Geometry II.

Figure 11. Same as Fig. 9 except these data are for the normalized Reynolds shear stress. Data at Re_C= 17M are omitted for clarity, but are similar to Re_C= 50M.

Figure 12. Same as Fig 11 except these data are for Geometry II.

Figure 13. PIV-measured streamwise velocity variance in the near wake for Geometry I (filled symbols) and Geometry II (open symbols) at varying x/C for Re_C= 1.4M (a), 4M (b), 17M (c), and 50M (d). The data are plotted in wake coordinates and scaled by the time-averaged velocity deficit, $\Delta U_{\max}$. The x/C coordinate is indicated in each panel. The solid line in the far right panel gives the self-preserving wake profile of a symmetric airfoil at $Re_C \sim 10^4$ (Wygnanski et al., 1986).

Figure 14. Same as Fig. 13 except these data are for the normalized vertical velocity variance.

Figure 15. Same as Fig. 13 except these data are for the normalized Reynolds shear stress.

Figure 16. Near-Wake LDV-measured temporal power spectra of vertical velocity fluctuations at x/C = 1.01 at Re_C= 1.4M, 4M, 17M and 50M for Geometry I (a) and Geometry I (b). These data were taken at the location of peak vertical velocity fluctuations; Table 2 lists their y/C locations. Numerals indicate Re_C in millions. The line to the right of the data has a slope of –5/3.

Figure 17. Same as Fig. 16 except these data are from x/C=1.07.

Figure 18. PIV-measured spatial power spectra of vertical velocity fluctuations along the line segment defined by (x/C, y/C) = (1.000, 0.009) and (1.100, -0.005) at Re_C= 1.4M, 4M, 17M and 50M for Geometry I (a) and Geometry I (b). This line falls near the locus of peak vertical velocity fluctuations for 1.03< x/C <1.10. Each spectrum is computed from between 500 and 1000 vector fields. Numerals indicate Re_C in millions. The line to the right of the data has a slope of –5/3.

Figure 19. Illustration of the parameters used to quantify the LDV-measured vertical velocity spectral peaks in the near wake. Letters correspond to the panels in Figs. 20 and 21.

Figure 20. Characteristics of LDV-measured vertical-velocity near-wake spectral peaks at x/C = 1.01 vs. Re_C in millions: Geometry I —●—, and Geometry II —○—. Parameters are illustrated in Fig. 19. Panels show: the normalized vertical velocity variance, the height of the spectral peaks above the spectral background (b), the spectral background value (c), the spectral peak width (d), and the frequency of the spectral peak (e) presented as a *St* multiplied by 2π.

Figure 21. Same as Fig. 20 except these data are from x/C=1.07.

Figure 22. The power spectra of the pressure-side surface pressure fluctuations at x/C = 0.99 at various Re_C for Geometry I (a) and Geometry II (b). Numerals indicate Re_C in millions. The solid line below the data has a slope of –1.

Figure 23. Instantaneous PIV fields of normalized swirl, $\chi\Delta_y^{nom}/U_o$ for Geometry I at Re_C= 4M (a), and Geometry II at Re_C = 1.4M (b), 4M (c), 17M (d), and 50M (e).

Figure 24. Actual and idealized instantaneous velocity and vorticity fields for Geometry I at Re_C = 4M. Panels present grayscale images of measured normalized vorticity $\omega\Delta_y^{nom}/U_o$ (a), vorticity of the idealized vortices (b), measured normalized vertical velocity fluctuation, $(v-V)/U_o$ (c), and normalized vertical velocity, v/U_o, computed from the idealized vortex field of (b).

Figure 25. Vortex circulation and core size of suction side vortices (———) and pressure side vortices (– – – ·) vs. downstream distance in the near wake. The panels follow the same arrangement as Fig. 23. The thicker lines represent normalized core circulation, read from axes on the left. Thinner lines represent core diameter, read from the axes on the right. The vertical dashed line in the left part of each frame indicates the x/C location of the peak vertical velocity fluctuations from Figs. 9 and 10.

Figure 26. Vortex center locations vs. downstream distance in the near wake; suction side vortices ———; pressure side vortices — —; vertical distance between suction side and pressure side vortices ·········· (illustrated in panel a); and vertical location of maximum vertical velocity fluctuations at the given x/C – – – ·. The panels follow the same arrangement as Fig. 23

Figure 27. Conditionally-averaged PIV fields of normalized mean swirl, $\chi\Delta_y^{nom}/U_o$, rendered as grayscale images. The panels follow the same arrangement as Fig. 23.

Figure 28. Measured and reconstructed vertical velocity fluctuations vs. downstream distance in the near wake; fluctuations induced by suction side vortices $\overline{v_s'^2}/U_o^2$ ———; fluctuations induced by pressure side vortices $\overline{v_p'^2}/U_o^2$ — — ; contribution of correlation between suction and pressure side induced fluctuations

$2(\overline{v_s v_p} - \bar{v}_s \bar{v}_p)/U_o^2$ ·········· ; total fluctuations from identified vortices, $\overline{v'^2}/U_o^2$ — · · – ; and PIV-measured variance of the vertical velocity fluctuations $\overline{v'^2}/U_o^2$ ●. The panels follow the same arrangement as Fig. 23.

Figure 29. Illustration of the vertical velocity induced at the trailing edge by a suction side vortex. Here the induced velocity is assumed to influence the formation of a pressure-side vortex. The suction side vortex strength may be related to the suction side circulation flux across surface A-B.

Figure 30. The normalized mean suction side shear rate at the trailing edge vs. Re_C from Geometry I (○) and Geometry I (●).

Figure 31. Vortex shedding characteristics for the trailing edge flows of this study and for a minimally lifting strut (Blake, 1984) vs. the dimensionless shear rate parameter, $(dU_t/dh)^{ss}/(U_o/\Delta_y)$. Shedding parameters (*y*-axes) are extracted from the LDV temporal spectra at $x/C = 1.01$ (see Figs. 16, 19, and 20). The mean suction side shear rate is from Fig. 30 but is scaled by the measured wake thickness, Δ_y, given in the text to form the *x*-axes in this figure. The grey triangles indicate strut data: strut with 45° rounded trailing edge ▲; 25° rounded trailing edge ▼; and strut with 25° sharp trailing edge ◀. The solid lines indicate curve fits in each panel: $y=0.001+10^{-9}e^{18x}$ (a), $y=1.02-0.77x$ (b), $y=0.023+0.29x^6$ (c), and $y=-0.039+0.076x$ (d).

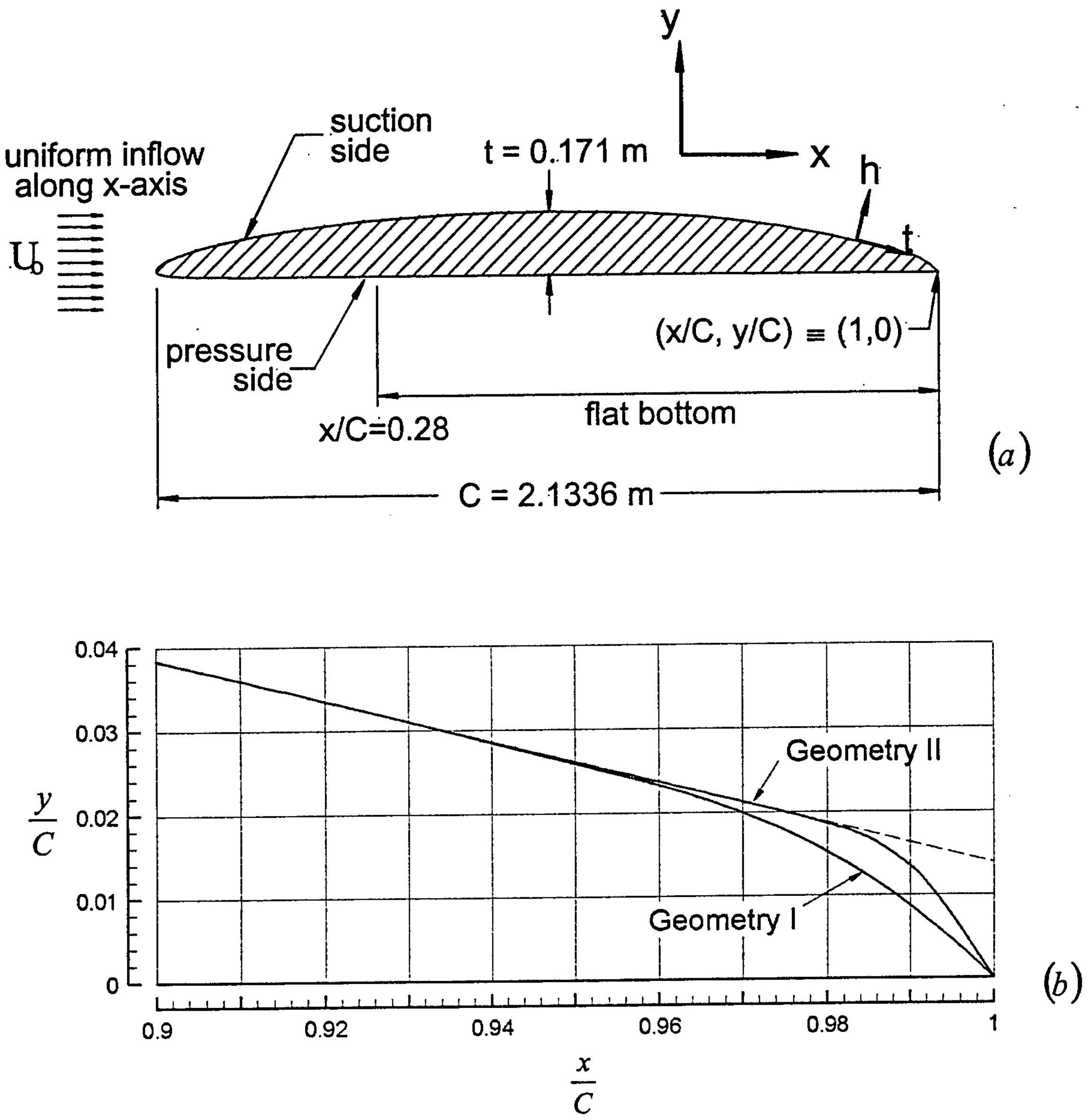
y
x
suction side
uniform inflow along x-axis
U_o
t = 0.171 m
h
t
pressure side
(x/C, y/C) ≡ (1,0)
x/C=0.28
flat bottom
(a)
C = 2.1336 m
0.04
0.03
0.02
0.01
0
y/C
Geometry II
Geometry I
0.9
0.92
0.94
0.96
0.98
1
x/C
(b)

Fig. 1

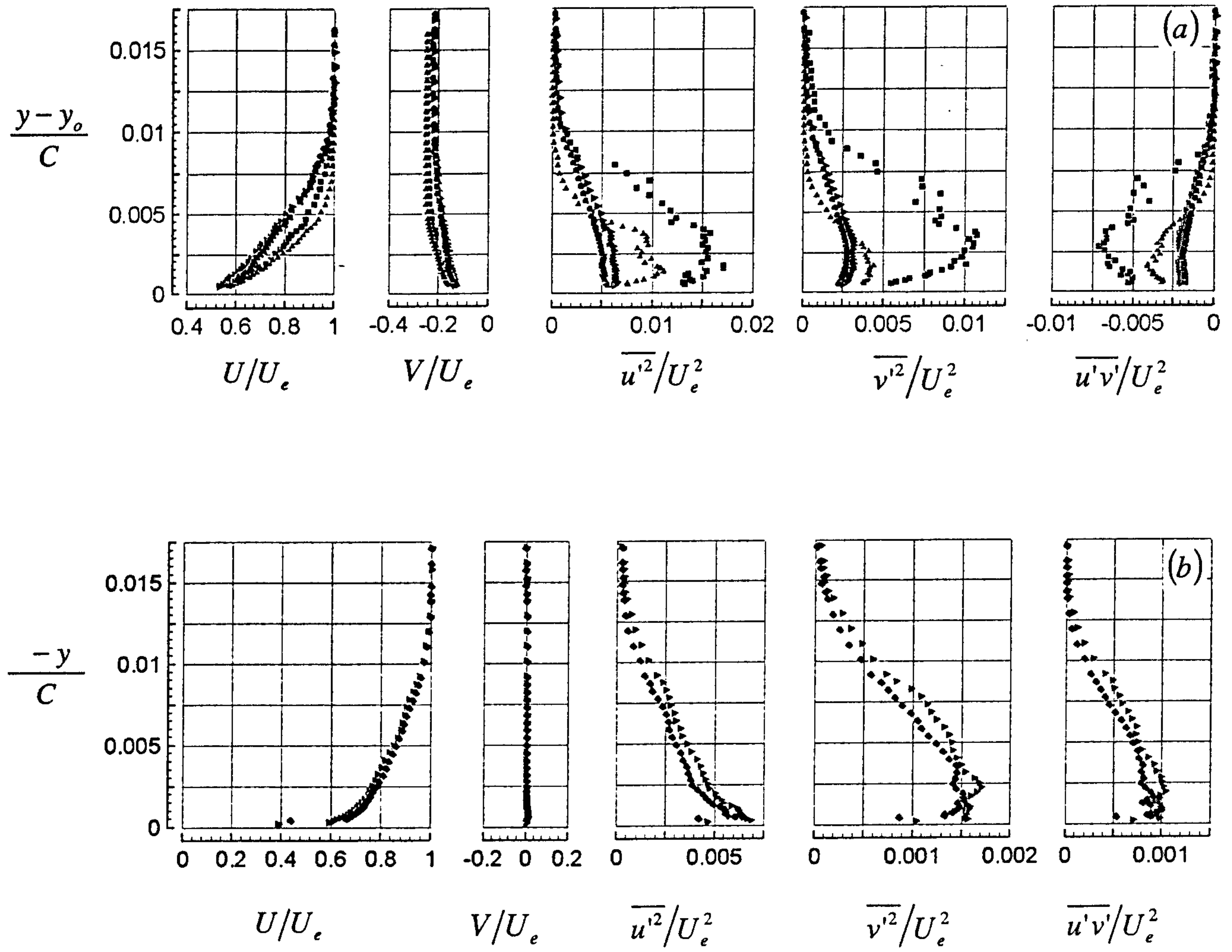
(a)
$\frac{y-y_o}{C}$
0.015
0.01
0.005
0
0.4 0.6 0.8 1
U/U_e
-0.4 -0.2 0
V/U_e
0 0.01 0.02
$\overline{u'^2}/U_e^2$
0 0.005 0.01
$\overline{v'^2}/U_e^2$
-0.01 -0.005 0
$\overline{u'v'}/U_e^2$
(b)
$\frac{-y}{C}$
0.015
0.01
0.005
0
0 0.2 0.4 0.6 0.8 1
U/U_e
-0.2 0 0.2
V/U_e
0 0.005
$\overline{u'^2}/U_e^2$
0 0.001 0.002
$\overline{v'^2}/U_e^2$
0 0.001
$\overline{u'v'}/U_e^2$

Fig. 2

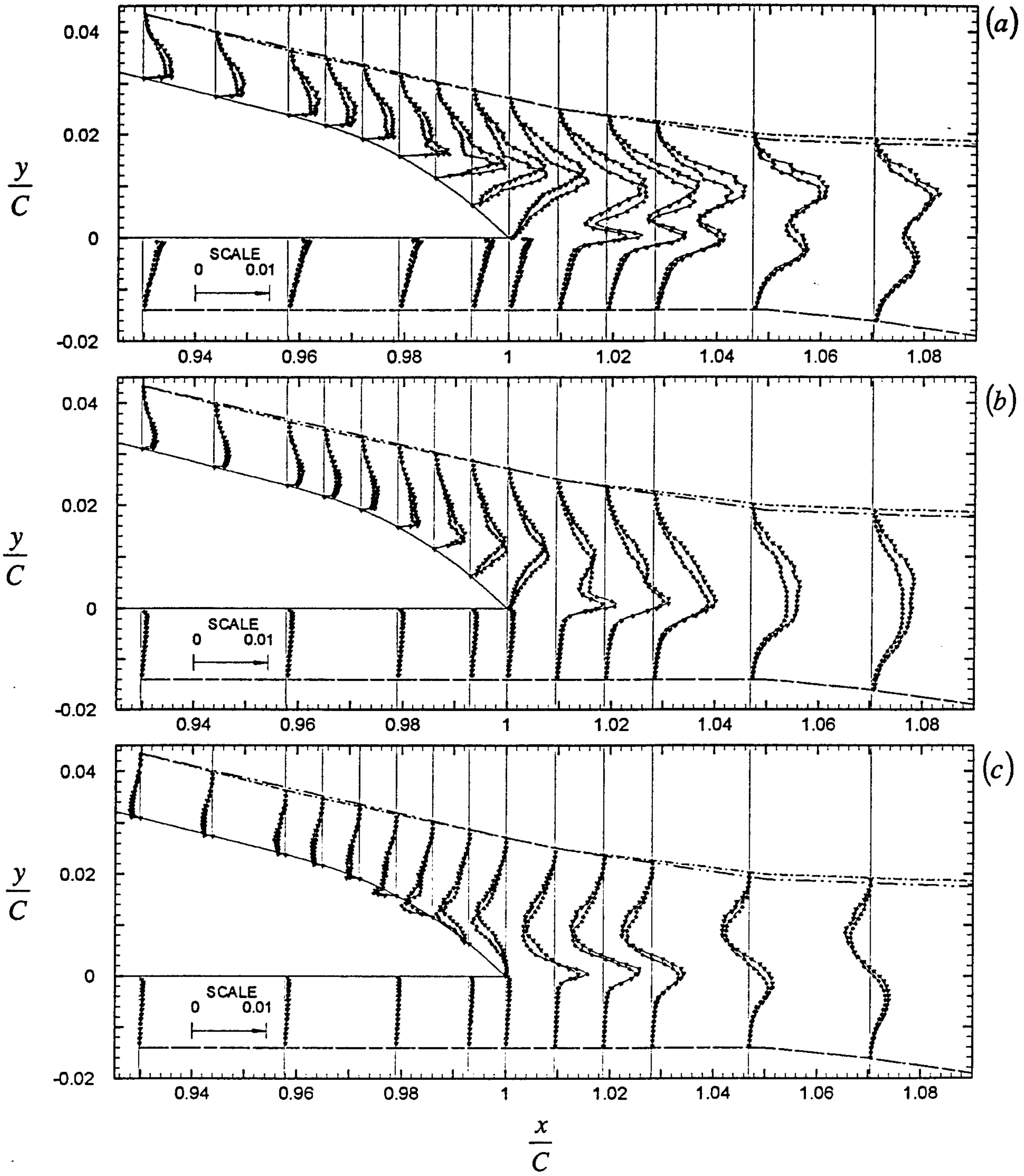

Fig. 3

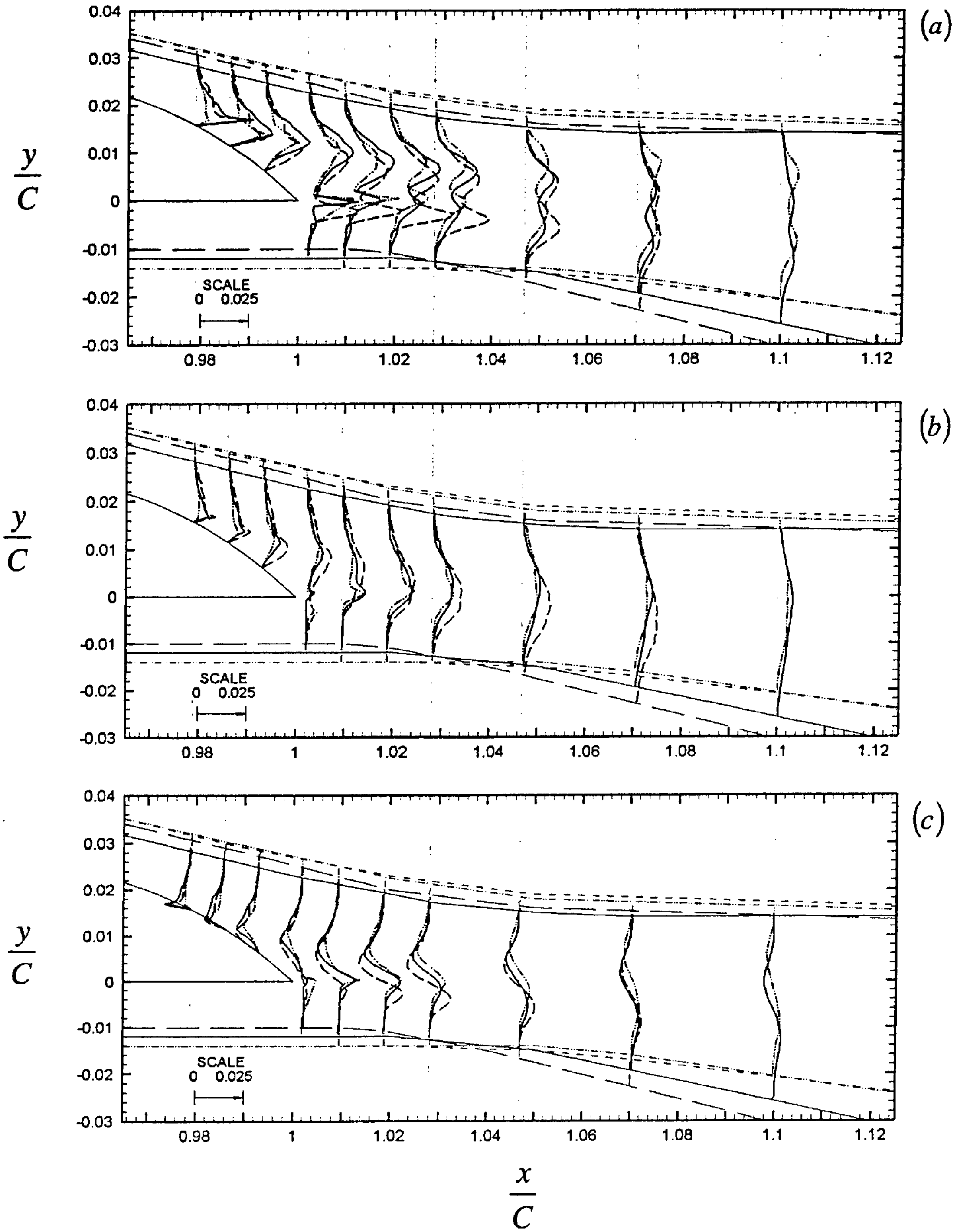
(a)
(b)
(c)
y/C
x/C
SCALE
0 0.025
0.04
0.03
0.02
0.01
0
-0.01
-0.02
-0.03
0.98
1
1.02
1.04
1.06
1.08
1.1
1.12

Fig. 4

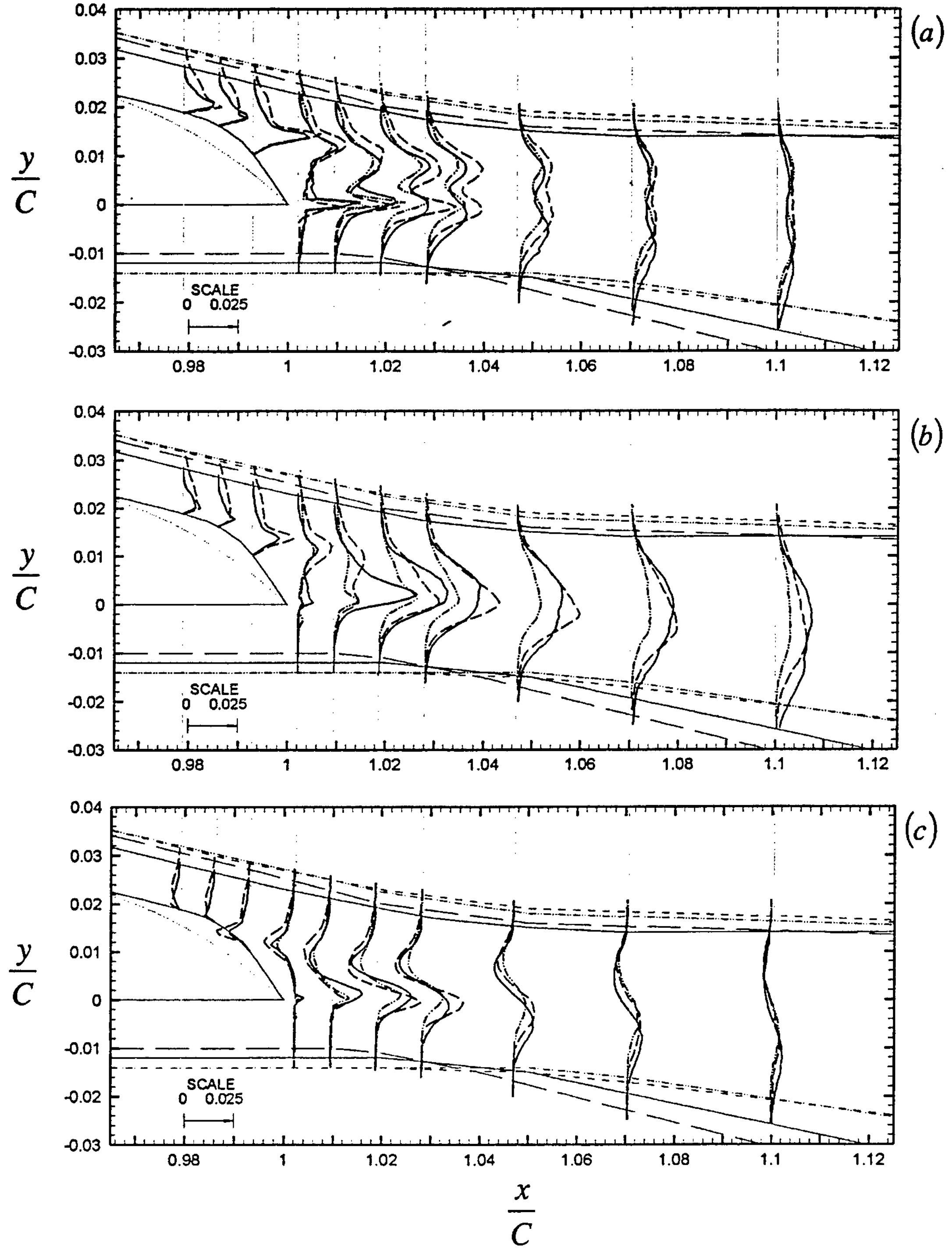
(a)
(b)
(c)
0.04
0.03
0.02
0.01
0
-0.01
-0.02
-0.03
y/C
SCALE
0 0.025
0.98
1
1.02
1.04
1.06
1.08
1.1
1.12
x/C

Fig. 5

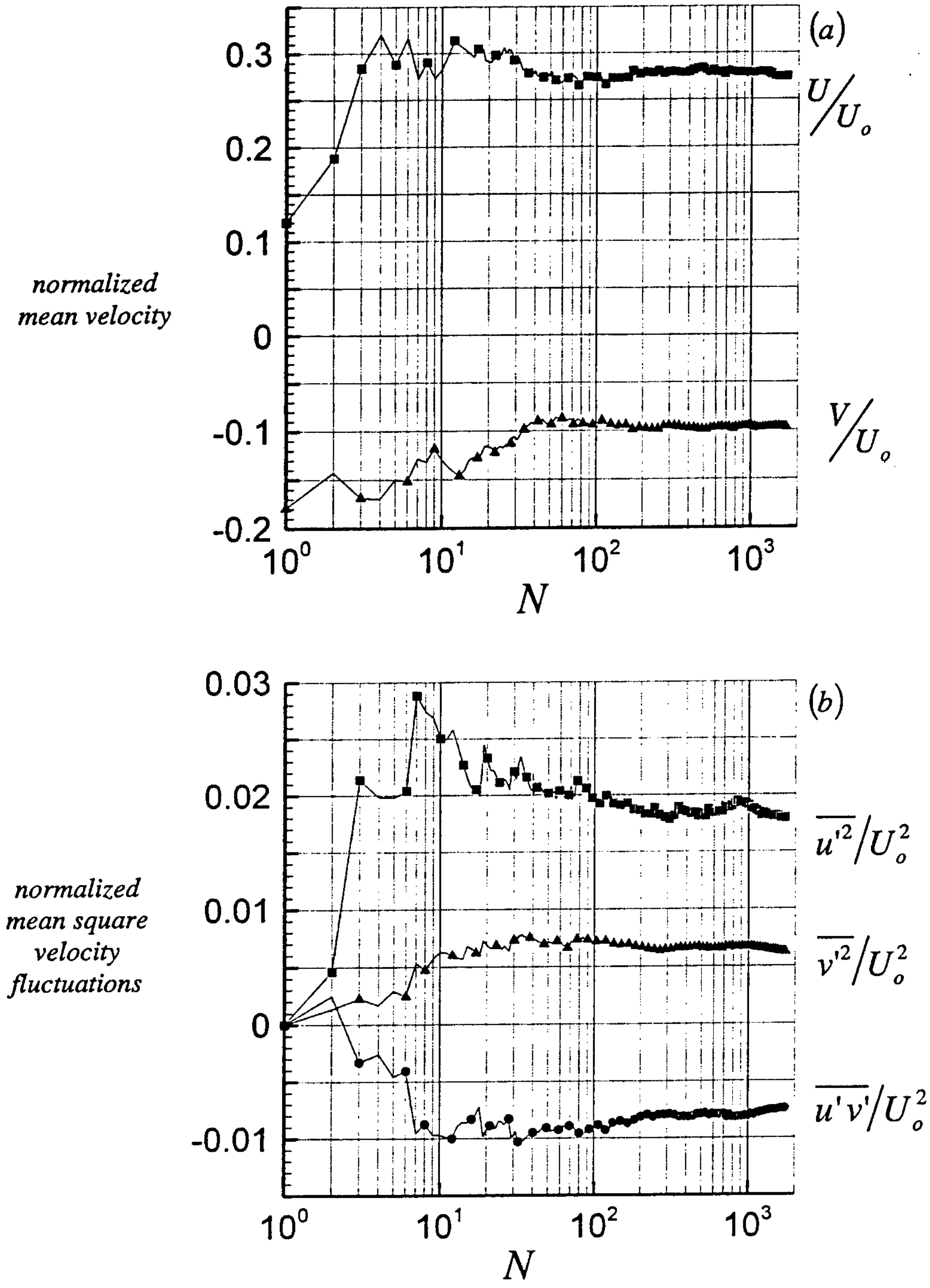
(a)
normalized mean velocity
0.3
0.2
0.1
0
-0.1
-0.2
U/U_o
V/U_o
10^0
10^1
10^2
10^3
N
(b)
normalized mean square velocity fluctuations
0.03
0.02
0.01
0
-0.01
$\overline{u'^2}/U_o^2$
$\overline{v'^2}/U_o^2$
$\overline{u'v'}/U_o^2$
10^0
10^1
10^2
10^3
N

Fig. 6

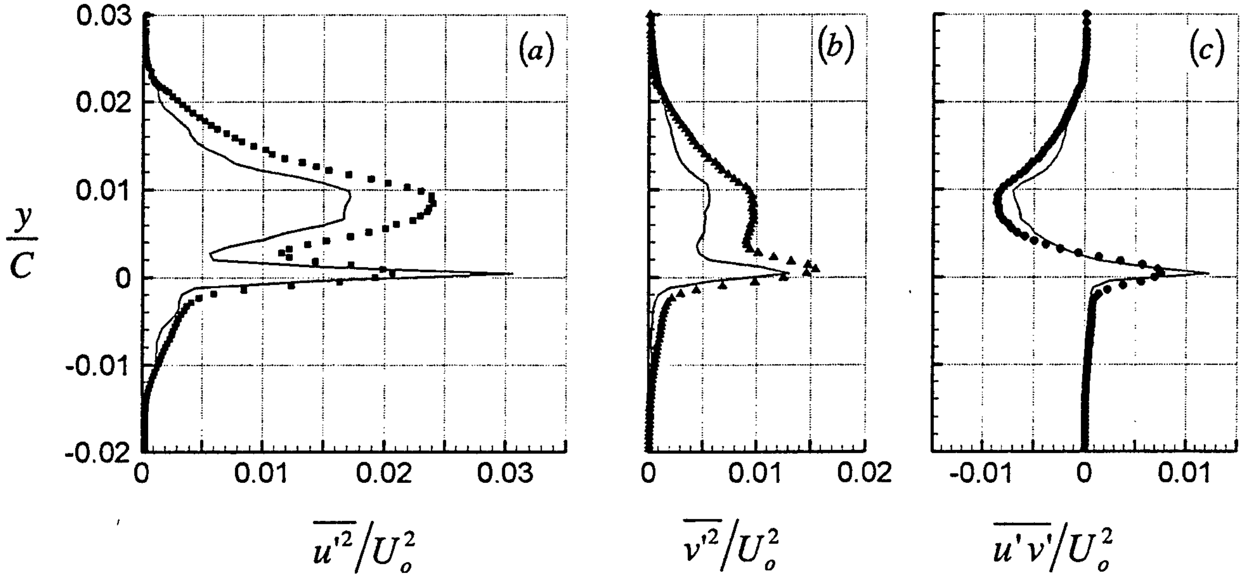

0.03
0.02
0.01
0
-0.01
-0.02
$\frac{y}{C}$
(a)
(b)
(c)
0
0.01
0.02
0.03
$\overline{u'^2}/U_o^2$
0
0.01
0.02
$\overline{v'^2}/U_o^2$
-0.01
0
0.01
$\overline{u'v'}/U_o^2$

Fig. 7

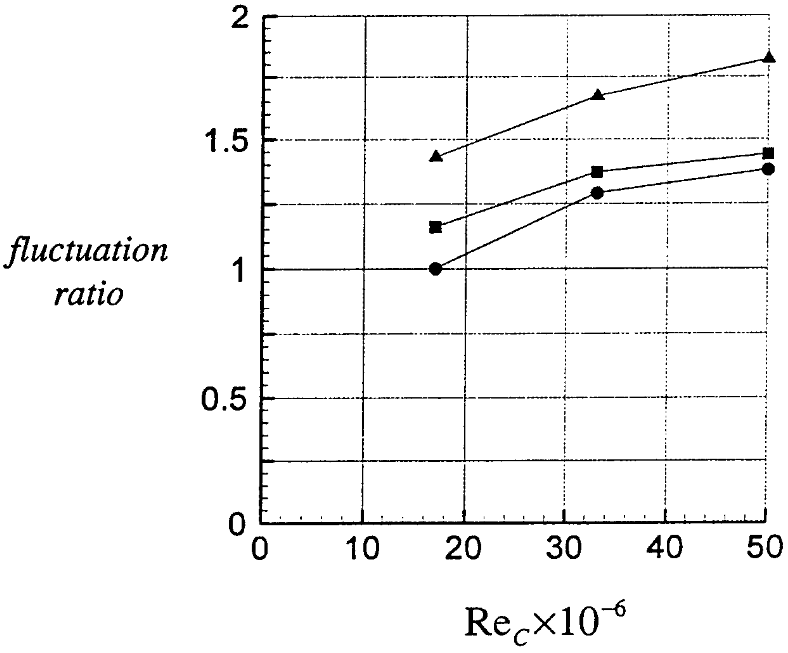

Fig. 8

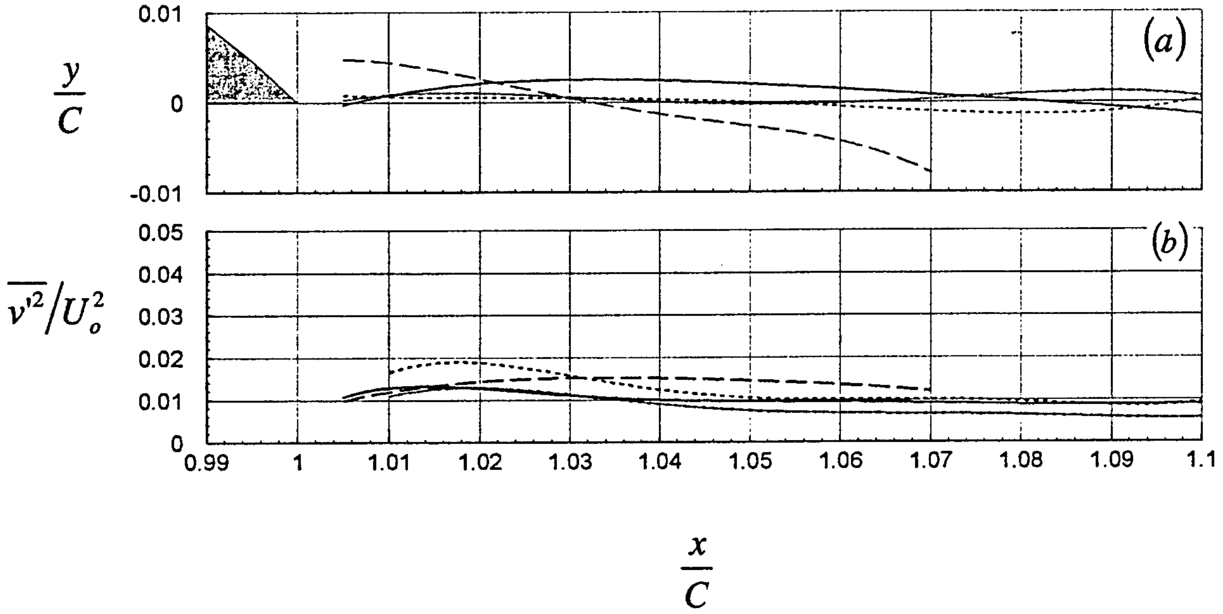
0.01
$\frac{y}{C}$
0
-0.01
(a)
0.05
0.04
$\overline{v'^2}/U_o^2$
0.03
0.02
0.01
0
(b)
0.99
1
1.01
1.02
1.03
1.04
1.05
1.06
1.07
1.08
1.09
1.1
$\frac{x}{C}$

Fig. 9

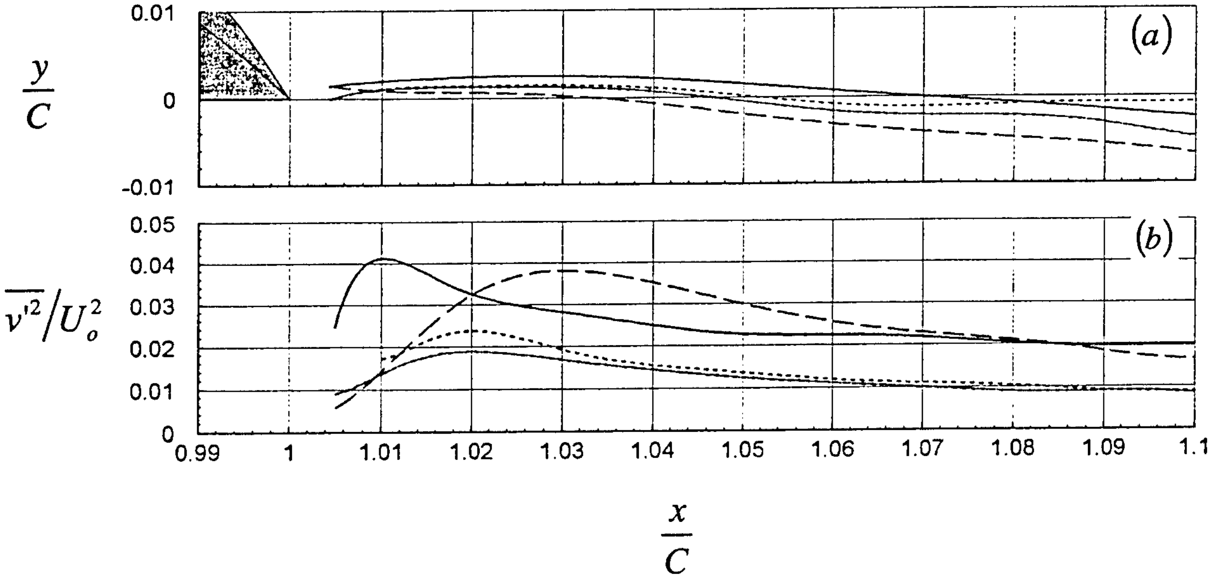
0.01
y/C
0
-0.01
(a)
0.05
0.04
$\overline{v'^2}/U_o^2$
0.03
0.02
0.01
0
(b)
0.99
1
1.01
1.02
1.03
1.04
1.05
1.06
1.07
1.08
1.09
1.1
x/C

Fig. 10

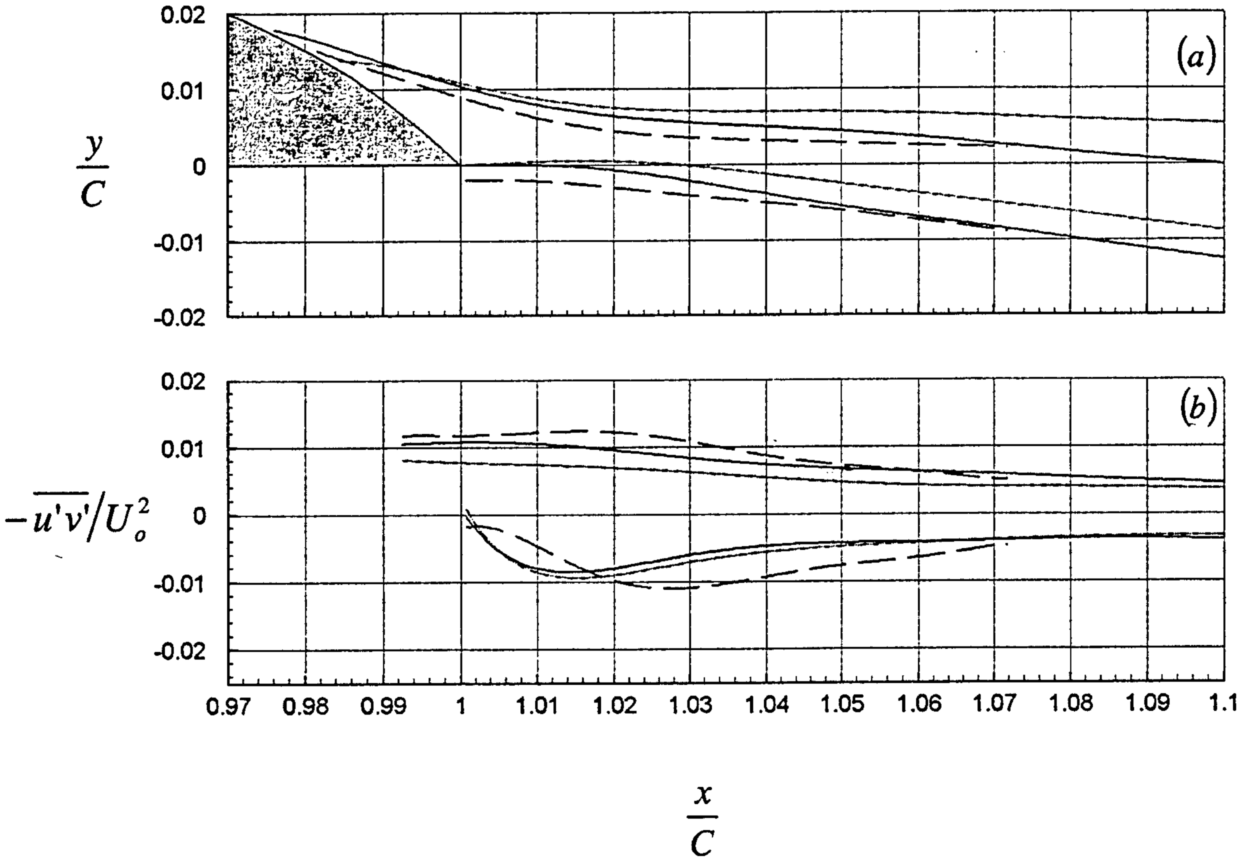
0.02
0.01
0
-0.01
-0.02
$\frac{y}{C}$
(a)
0.02
0.01
0
-0.01
-0.02
$-\overline{u'v'}/U_o^2$
(b)
0.97
0.98
0.99
1
1.01
1.02
1.03
1.04
1.05
1.06
1.07
1.08
1.09
1.1
$\frac{x}{C}$

Fig. 11

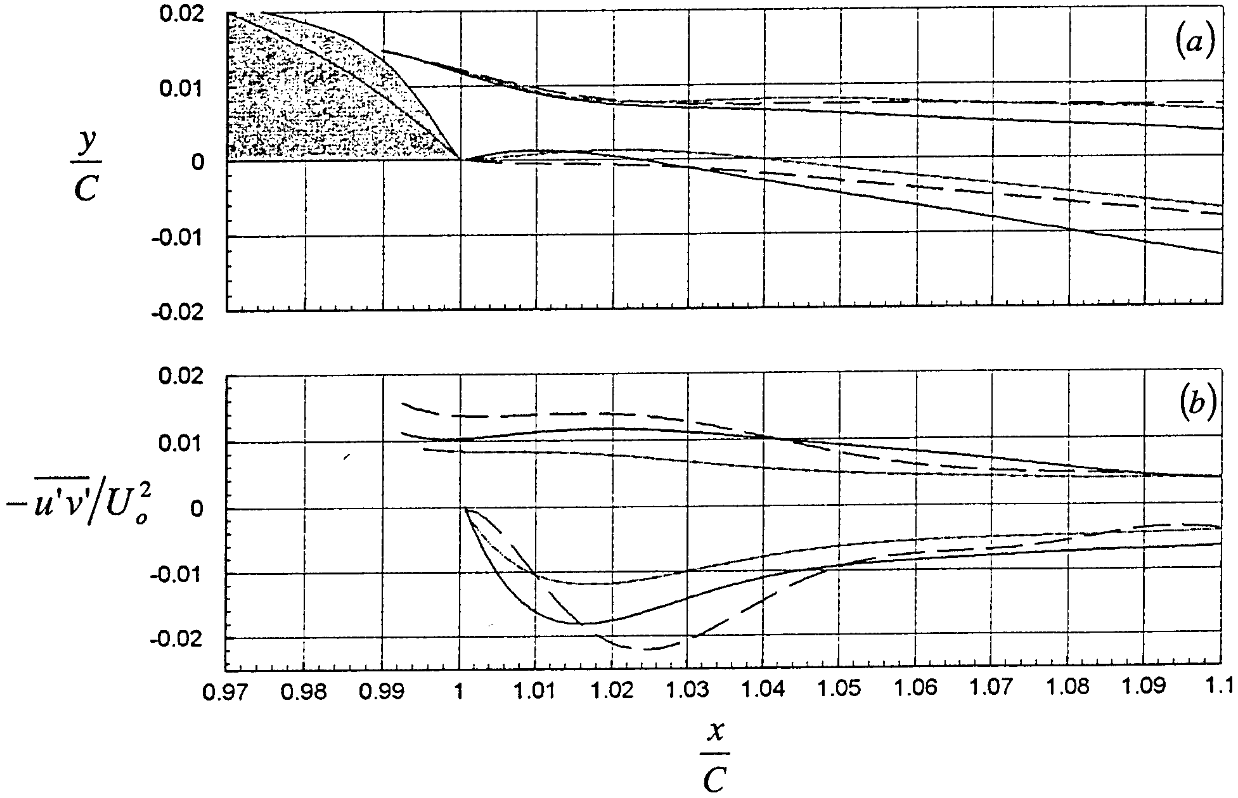
0.02
0.01
0
-0.01
-0.02
(a)
$\frac{y}{C}$
(b)
$-\overline{u'v'}/U_o^2$
0.97
0.98
0.99
1
1.01
1.02
1.03
1.04
1.05
1.06
1.07
1.08
1.09
1.1
$\frac{x}{C}$

Fig. 12

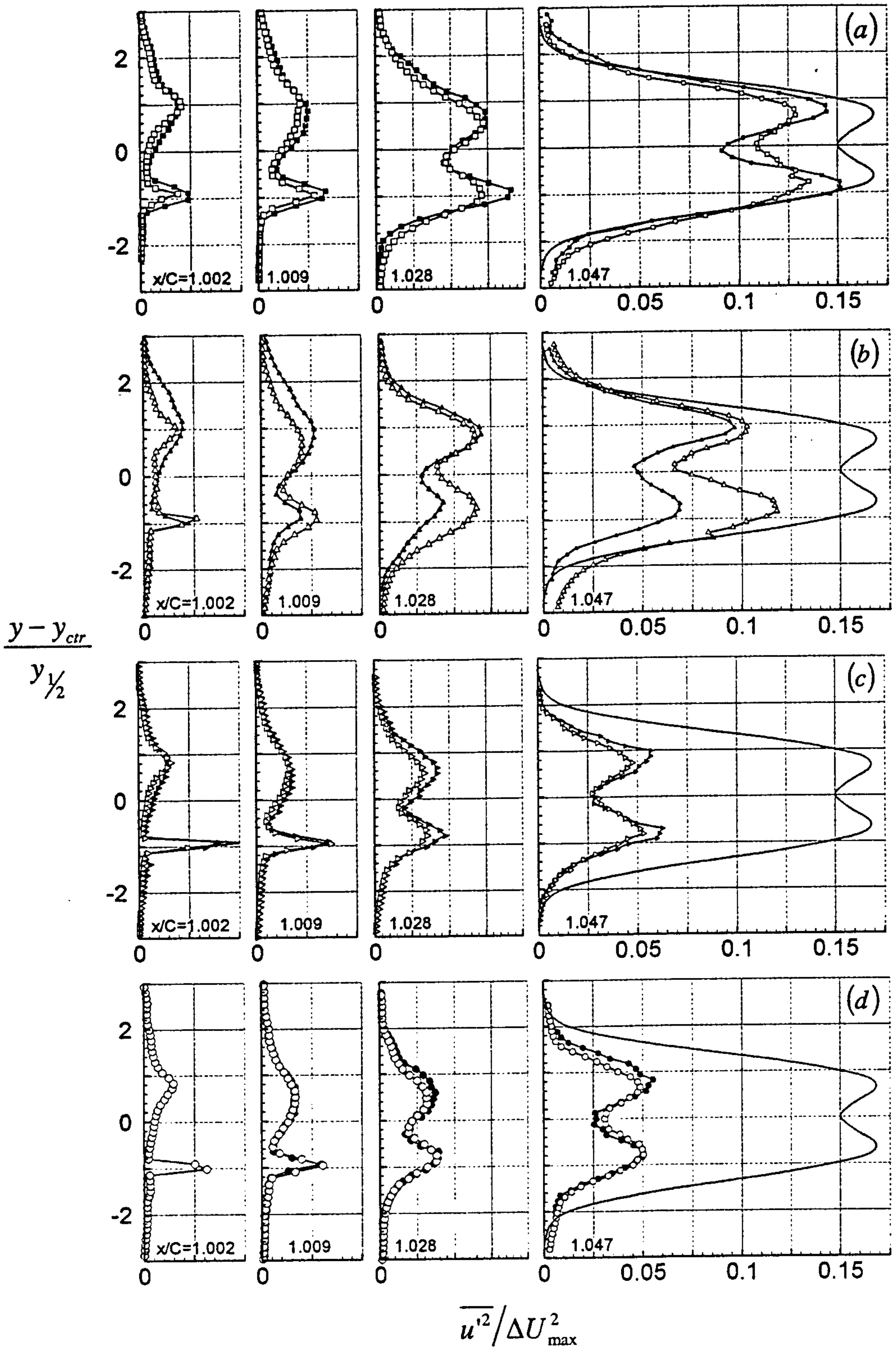
(a)
(b)
(c)
(d)
x/C=1.002
1.009
1.028
1.047
2
0
-2
0
0.05
0.1
0.15
$\frac{y - y_{ctr}}{y_{1/2}}$
$\overline{u'^2}/\Delta U_{\max}^2$

Fig. 13

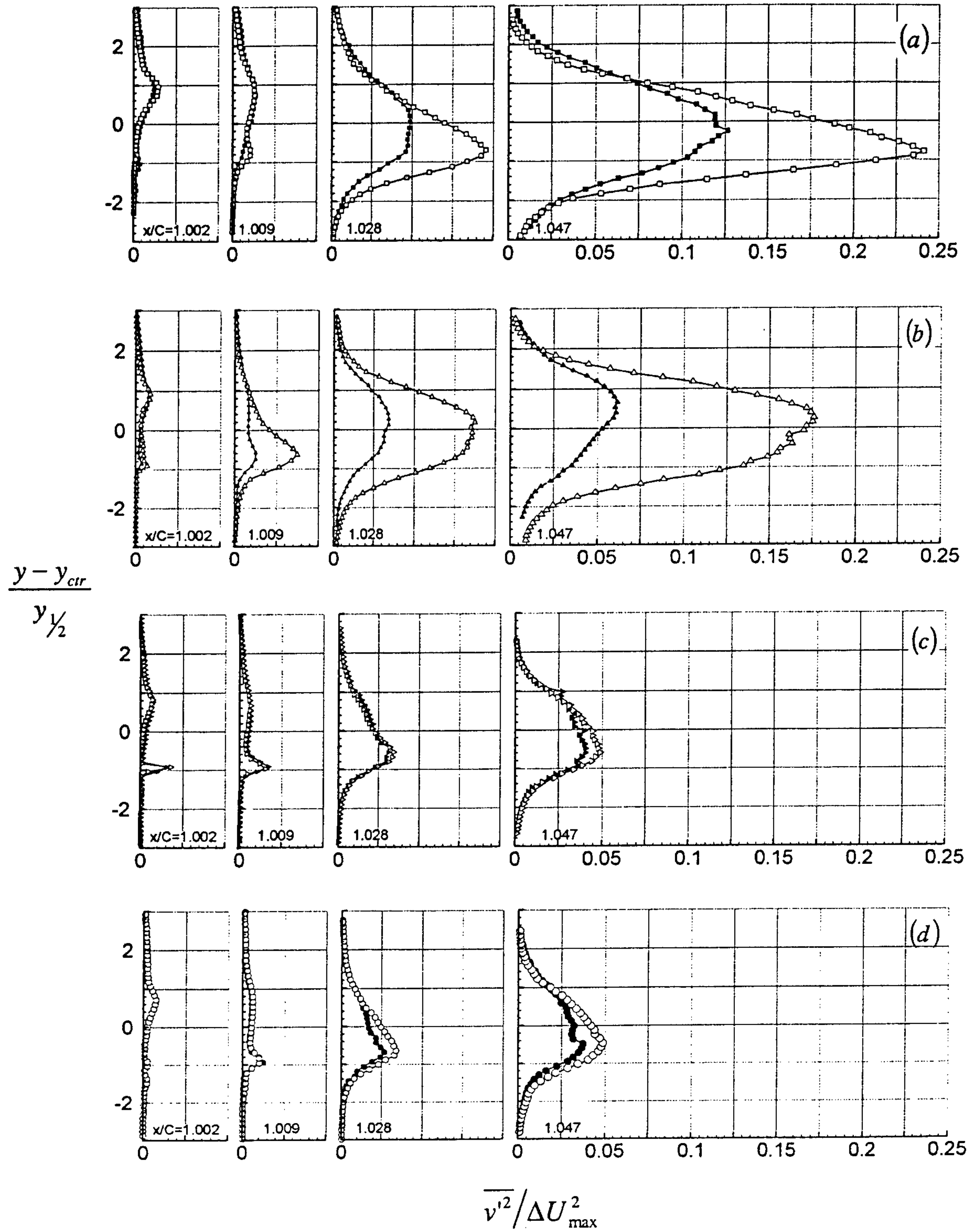
(a)
(b)
(c)
(d)
x/C=1.002
1.009
1.028
1.047
2
0
-2
0
0.05
0.1
0.15
0.2
0.25
$\frac{y - y_{ctr}}{y_{1/2}}$
$\overline{v'^2}/\Delta U_{\max}^2$

Fig. 14

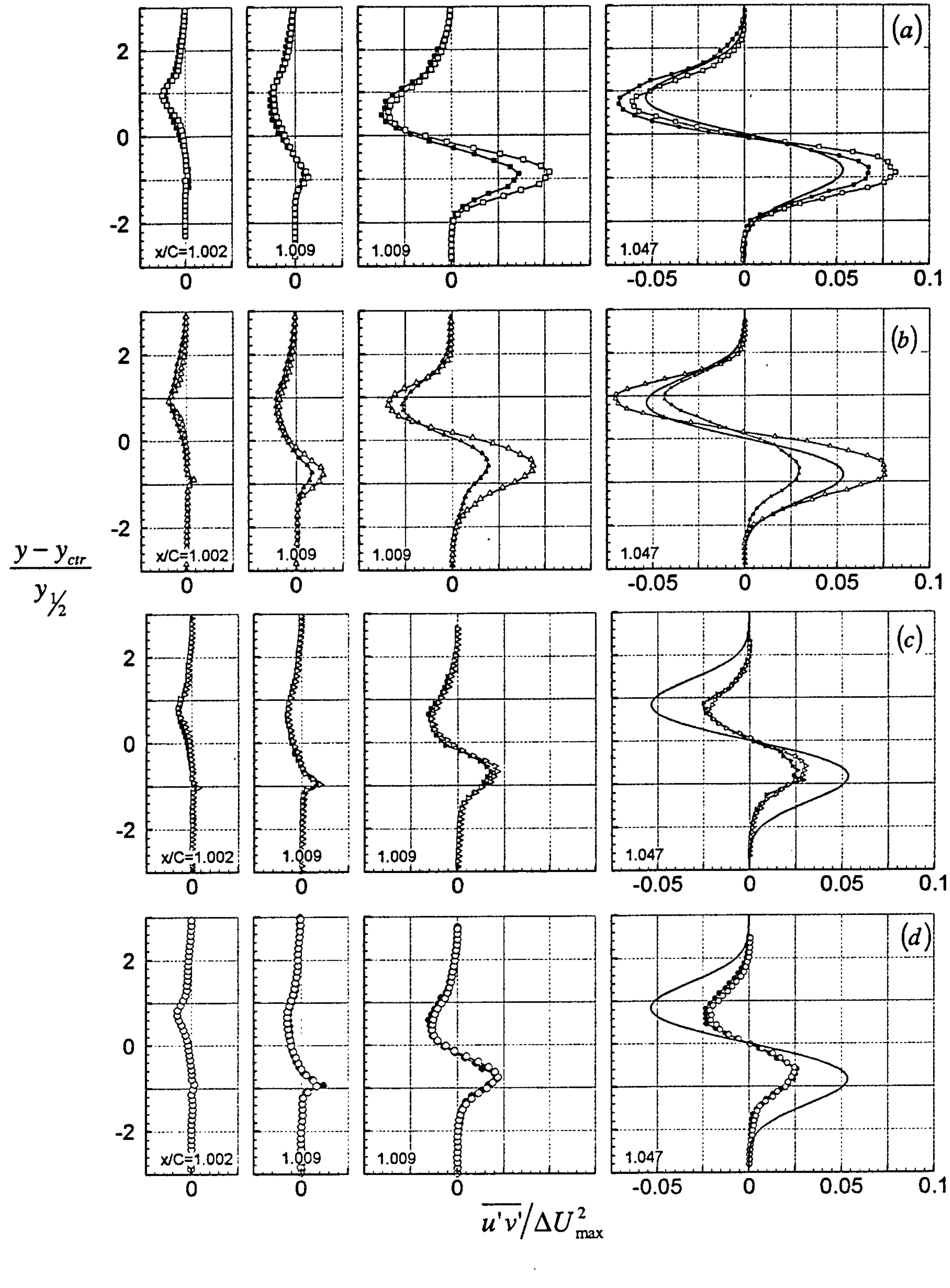
(a)
(b)
(c)
(d)
x/C=1.002
1.009
1.009
1.047
2
0
-2
0
-0.05
0.05
0.1
$\frac{y - y_{ctr}}{y_{1/2}}$
$\overline{u'v'}/\Delta U^2_{\max}$

Fig. 15

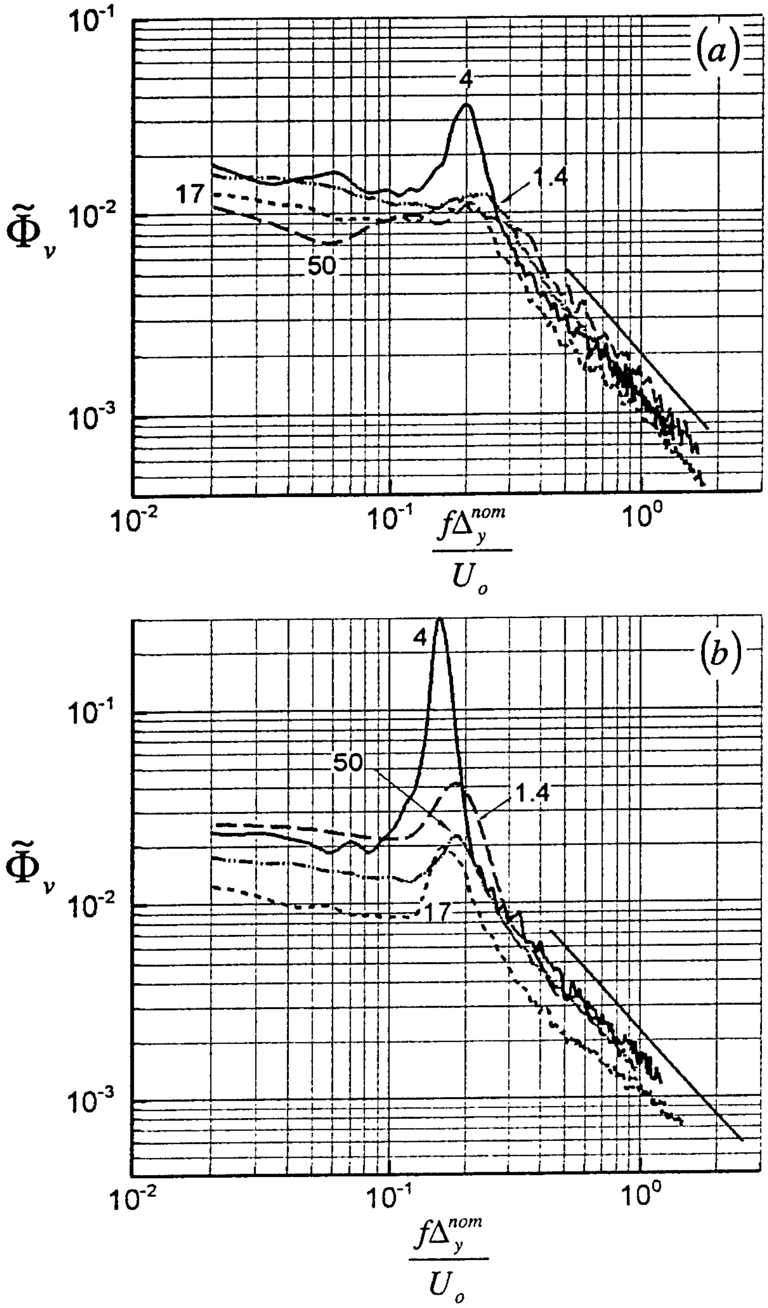

(a)
10^{-1}
10^{-2}
10^{-3}
$\tilde{\Phi}_v$
4
1.4
17
50
10^{-2}
10^{-1}
10^{0}
$\frac{f\Delta_y^{nom}}{U_o}$
(b)
10^{-1}
10^{-2}
10^{-3}
$\tilde{\Phi}_v$
4
50
1.4
17
10^{-2}
10^{-1}
10^{0}
$\frac{f\Delta_y^{nom}}{U_o}$

Fig. 16

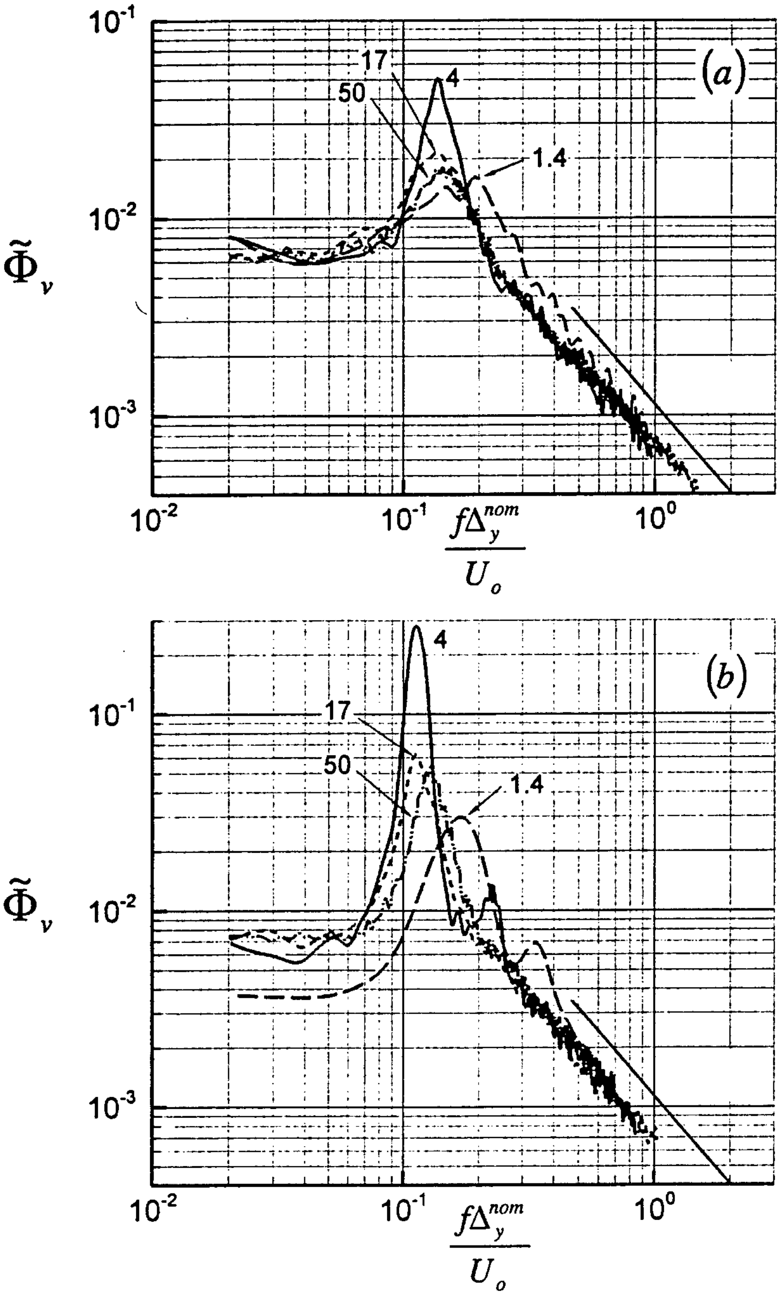

(a)
10^{-1}
10^{-2}
10^{-3}
$\tilde{\Phi}_v$
17
4
50
1.4
10^{-2}
10^{-1}
10^{0}
$\frac{f\Delta_y^{nom}}{U_o}$
(b)
4
10^{-1}
17
50
1.4
$\tilde{\Phi}_v$
10^{-2}
10^{-3}
10^{-2}
10^{-1}
10^{0}
$\frac{f\Delta_y^{nom}}{U_o}$

Fig. 17

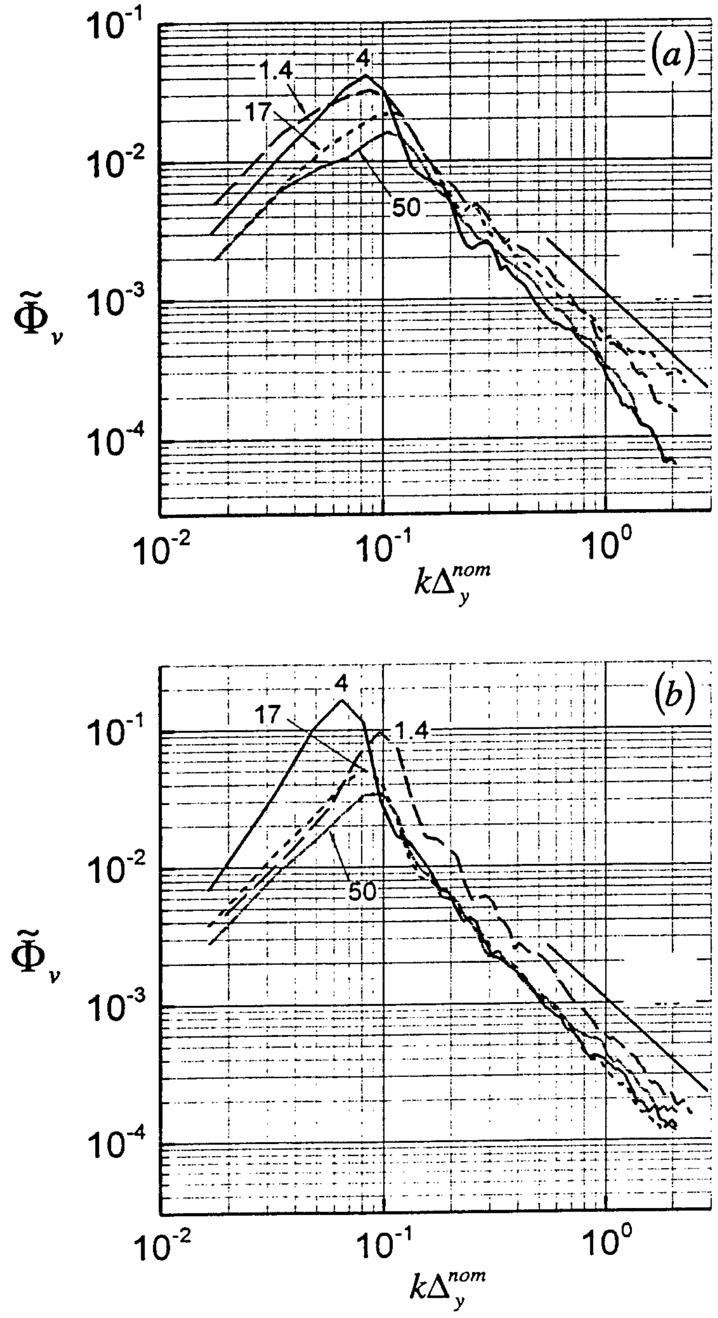
(a)
1.4
4
17
50
$\tilde{\Phi}_v$
10^{-1}
10^{-2}
10^{-3}
10^{-4}
10^{-2}
10^{-1}
10^{0}
$k\Delta_y^{nom}$
(b)
4
17
1.4
50
$\tilde{\Phi}_v$
10^{-1}
10^{-2}
10^{-3}
10^{-4}
10^{-2}
10^{-1}
10^{0}
$k\Delta_y^{nom}$

Fig. 18

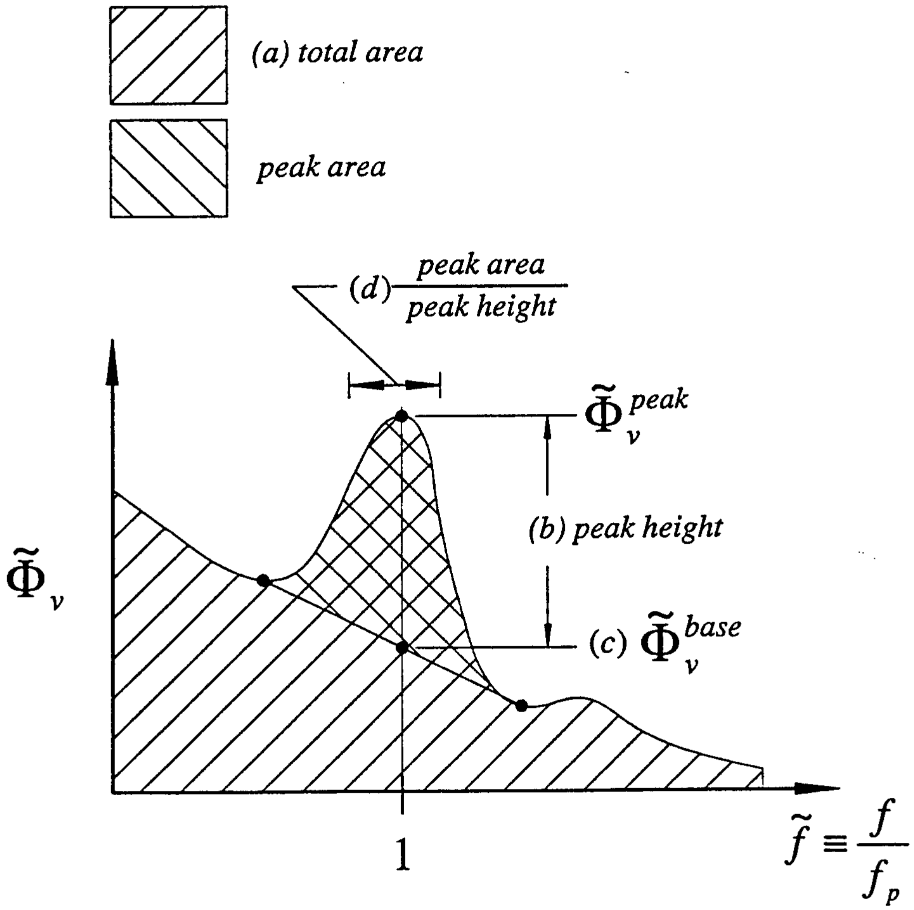
(a) total area
peak area
(d) $\frac{\text{peak area}}{\text{peak height}}$
$\tilde{\Phi}_v^{peak}$
(b) peak height
(c) $\tilde{\Phi}_v^{base}$
$\tilde{\Phi}_v$
1
$\tilde{f} \equiv \frac{f}{f_p}$

Fig. 19

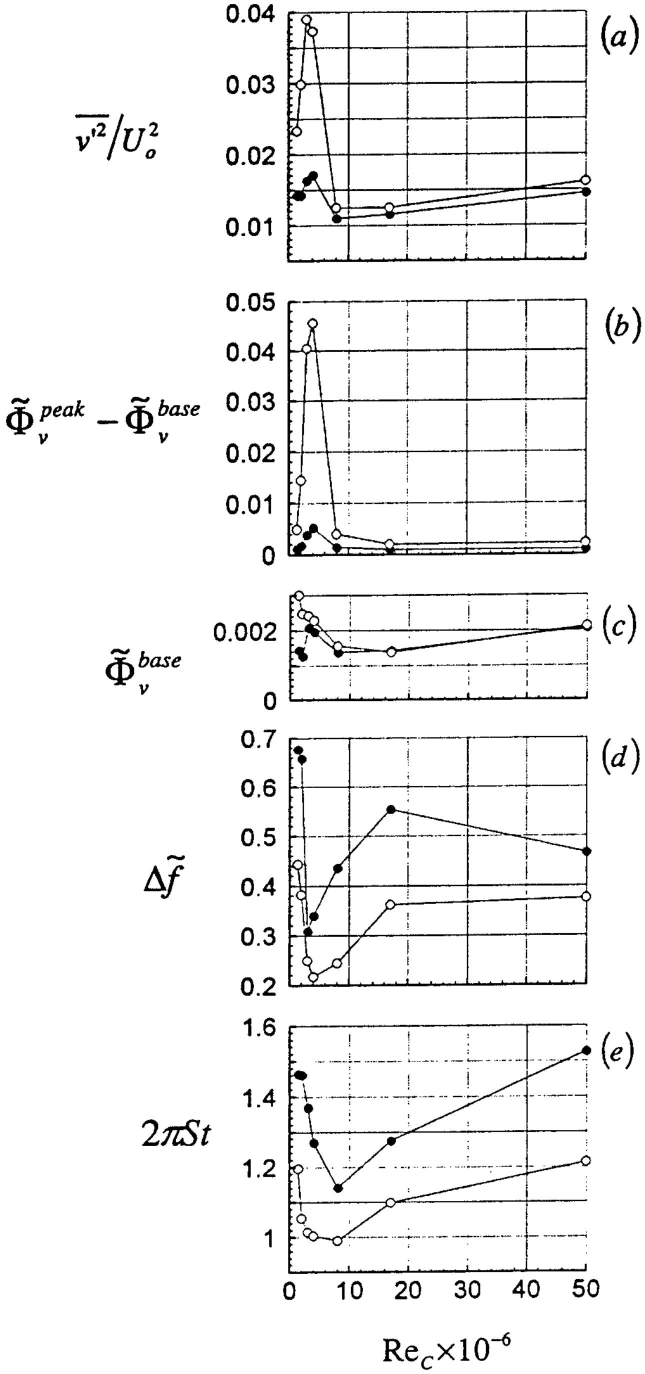
$\overline{v'^2}/U_o^2$
0.04
0.03
0.02
0.01
(a)
$\tilde{\Phi}_v^{peak} - \tilde{\Phi}_v^{base}$
0.05
0.04
0.03
0.02
0.01
0
(b)
$\tilde{\Phi}_v^{base}$
0.002
0
(c)
$\Delta\tilde{f}$
0.7
0.6
0.5
0.4
0.3
0.2
(d)
$2\pi St$
1.6
1.4
1.2
1
(e)
0
10
20
30
40
50
$\mathrm{Re}_C\times 10^{-6}$

Fig. 20

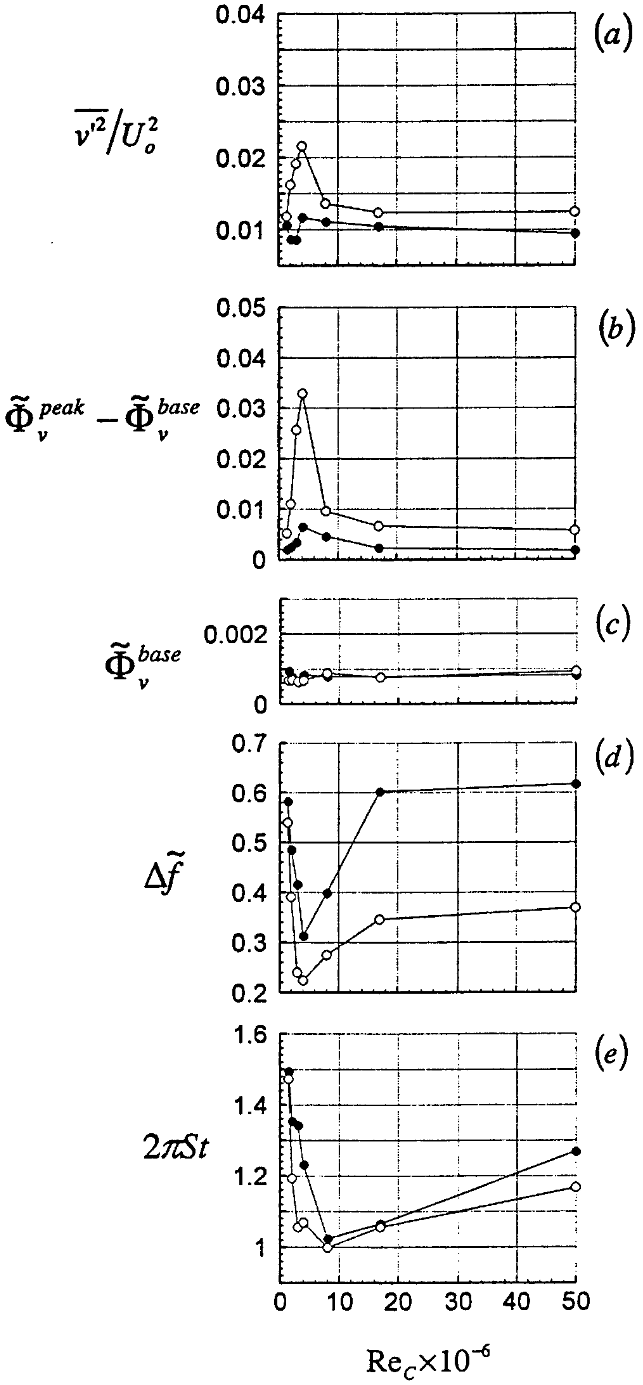
0.04
0.03
0.02
0.01
$\overline{v'^2}/U_o^2$
(a)
0.05
0.04
0.03
0.02
0.01
0
$\tilde{\Phi}_v^{peak} - \tilde{\Phi}_v^{base}$
(b)
0.002
0
$\tilde{\Phi}_v^{base}$
(c)
0.7
0.6
0.5
0.4
0.3
0.2
$\Delta\tilde{f}$
(d)
1.6
1.4
1.2
1
$2\pi St$
(e)
0
10
20
30
40
50
$\mathrm{Re}_C \times 10^{-6}$

Fig. 21

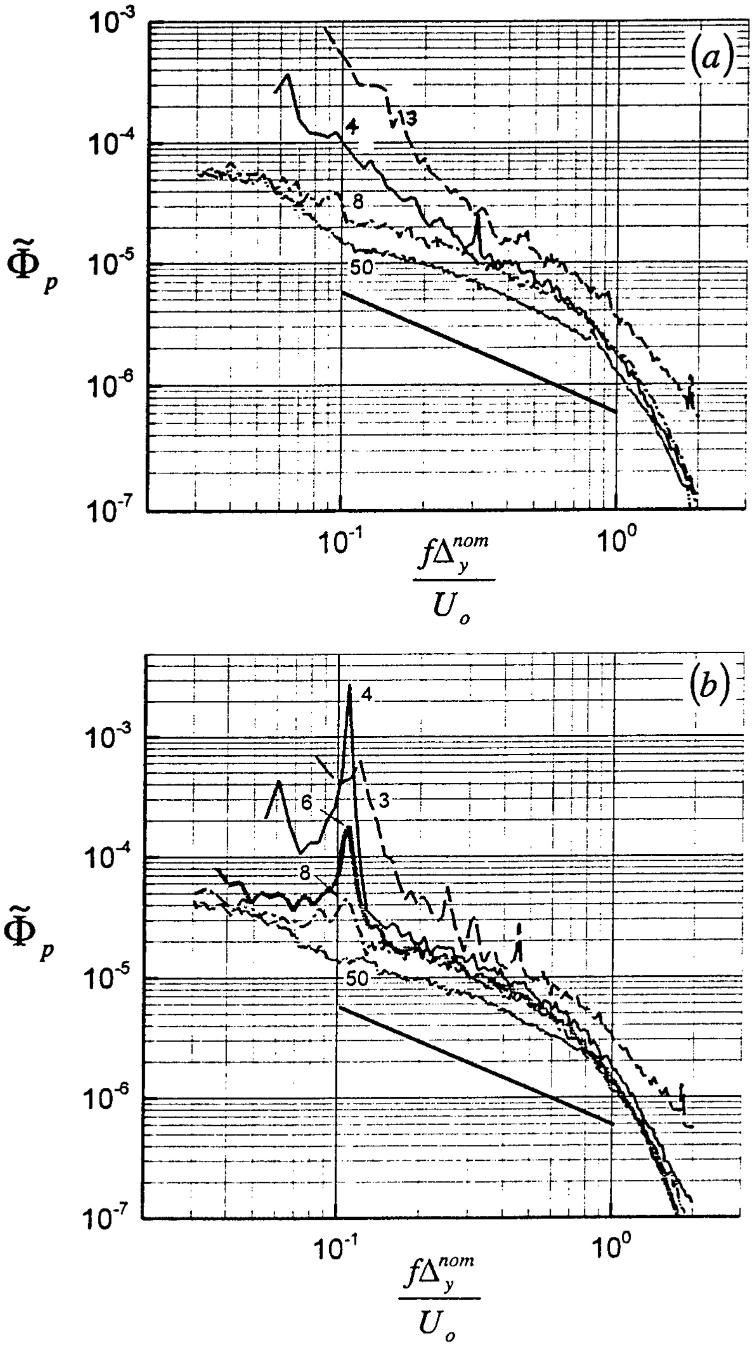
(a)
10^{-3}
10^{-4}
10^{-5}
10^{-6}
10^{-7}
$\tilde{\Phi}_p$
4
13
8
50
10^{-1}
10^{0}
$\frac{f\Delta_y^{nom}}{U_o}$
(b)
10^{-3}
10^{-4}
10^{-5}
10^{-6}
10^{-7}
$\tilde{\Phi}_p$
4
6
3
8
50
10^{-1}
10^{0}
$\frac{f\Delta_y^{nom}}{U_o}$

Fig. 22

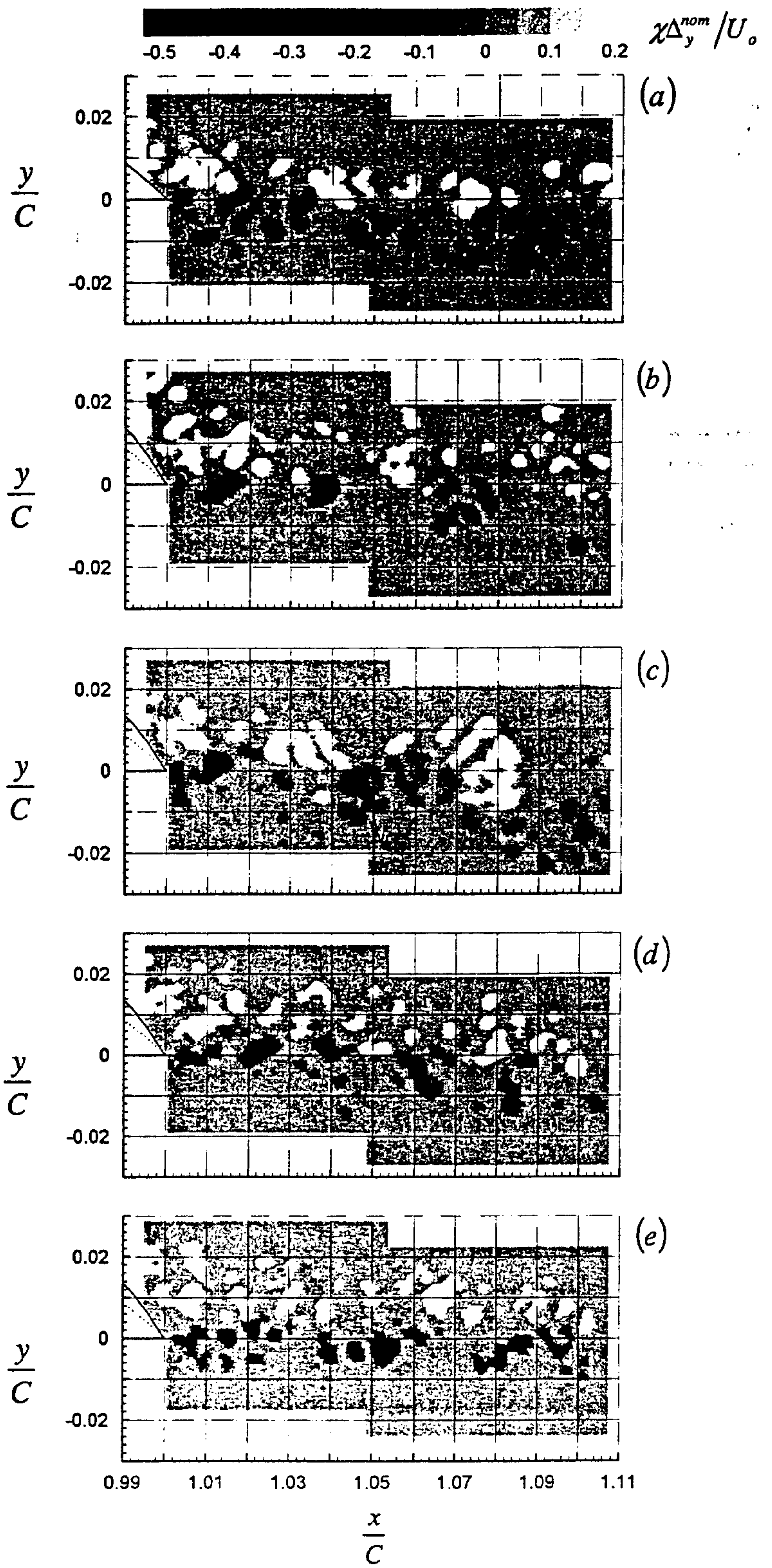
-0.5
-0.4
-0.3
-0.2
-0.1
0
0.1
0.2
$\chi\Delta_y^{nom}/U_o$
(a)
(b)
(c)
(d)
(e)
0.02
0
-0.02
$\frac{y}{C}$
0.99
1.01
1.03
1.05
1.07
1.09
1.11
$\frac{x}{C}$

Fig. 23

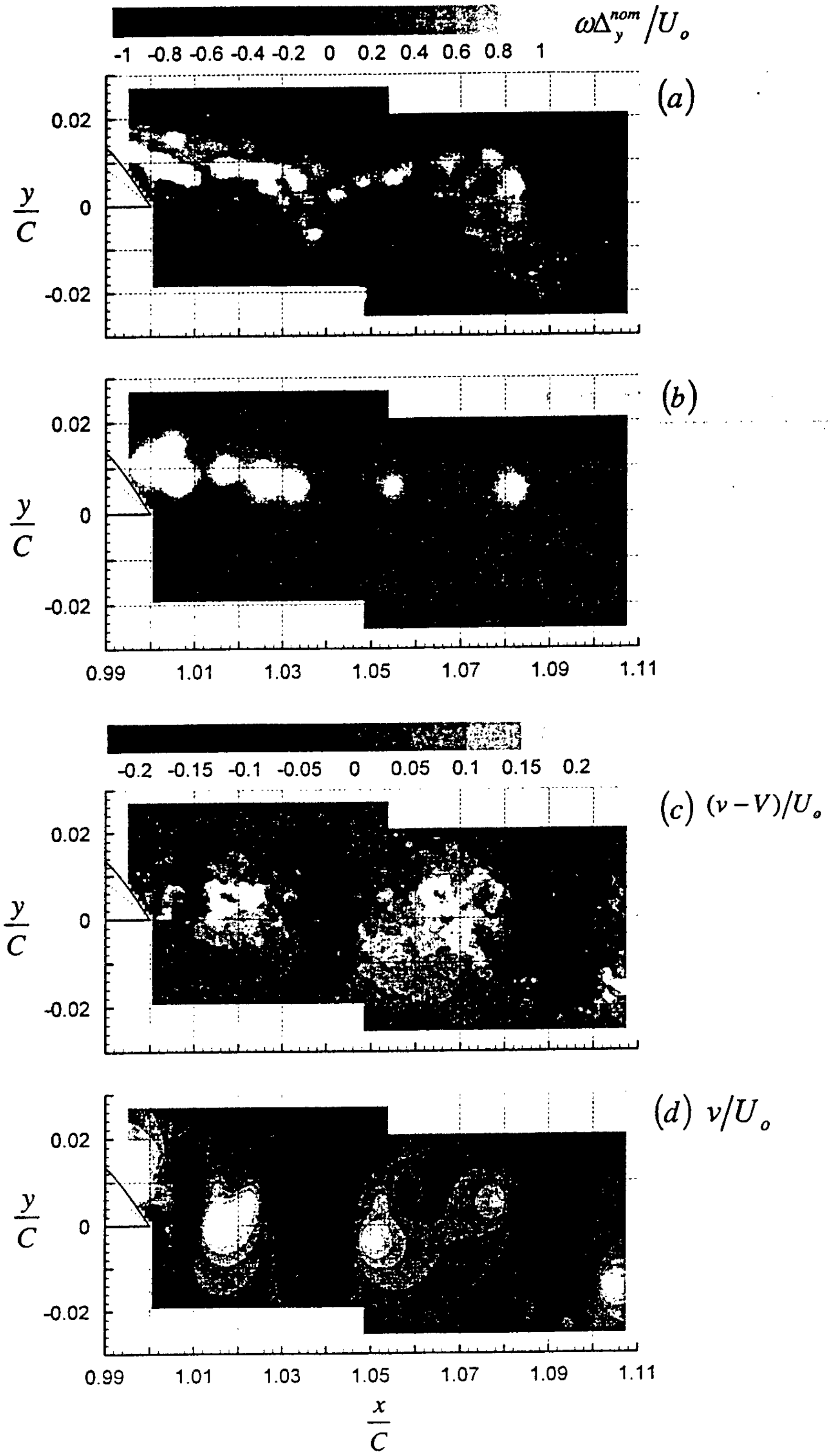
$\omega\Delta_y^{nom}/U_o$
-1 -0.8 -0.6 -0.4 -0.2 0 0.2 0.4 0.6 0.8 1
(a)
(b)
-0.2 -0.15 -0.1 -0.05 0 0.05 0.1 0.15 0.2
(c) $(v-V)/U_o$
(d) v/U_o
$\frac{y}{C}$
0.02
0
-0.02
0.99
1.01
1.03
1.05
1.07
1.09
1.11
$\frac{x}{C}$

Fig. 24

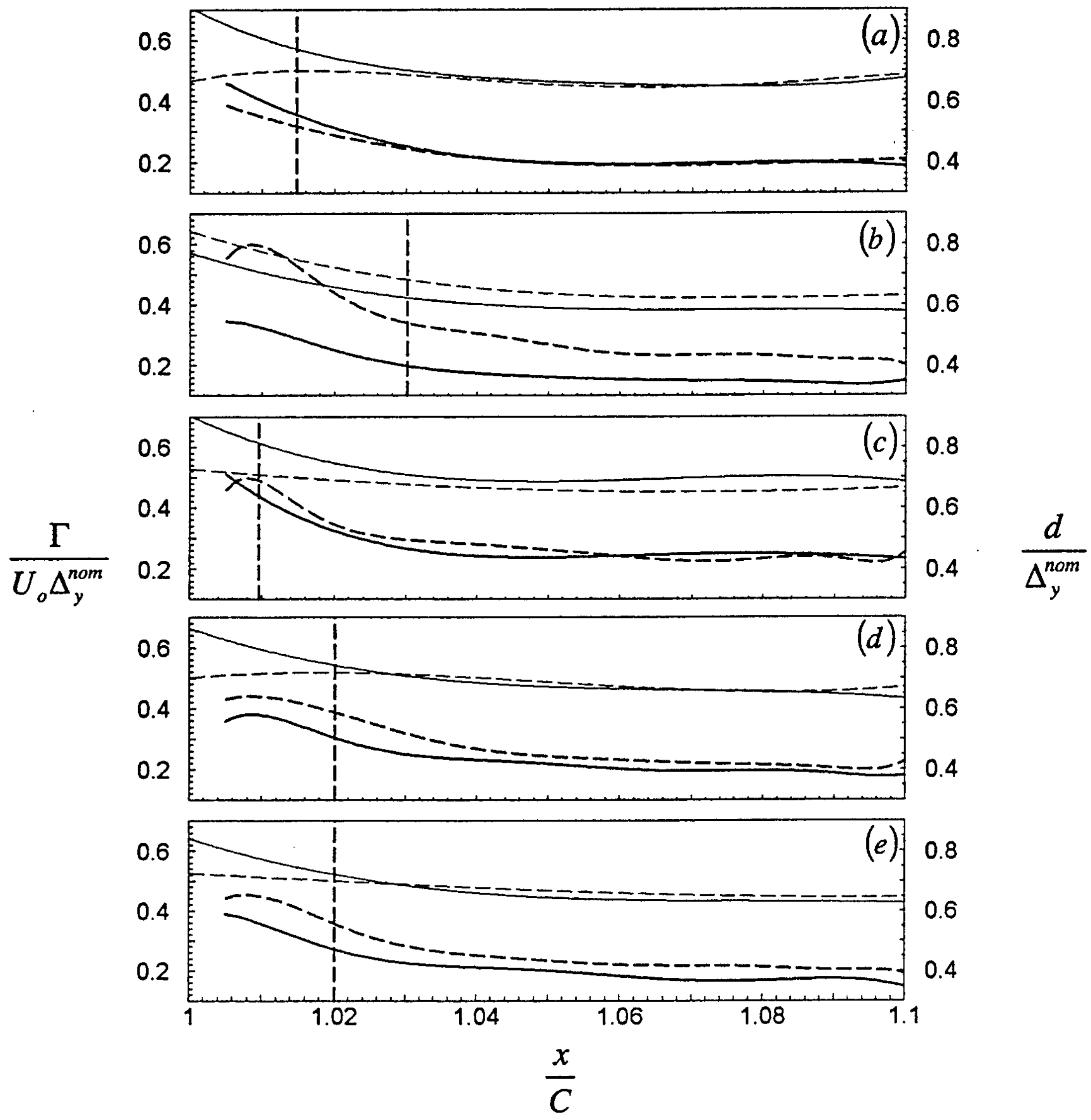
(a)
(b)
(c)
(d)
(e)
0.6
0.4
0.2
0.8
0.6
0.4
1
1.02
1.04
1.06
1.08
1.1
$\frac{\Gamma}{U_o \Delta_y^{nom}}$
$\frac{d}{\Delta_y^{nom}}$
$\frac{x}{C}$

Fig. 25

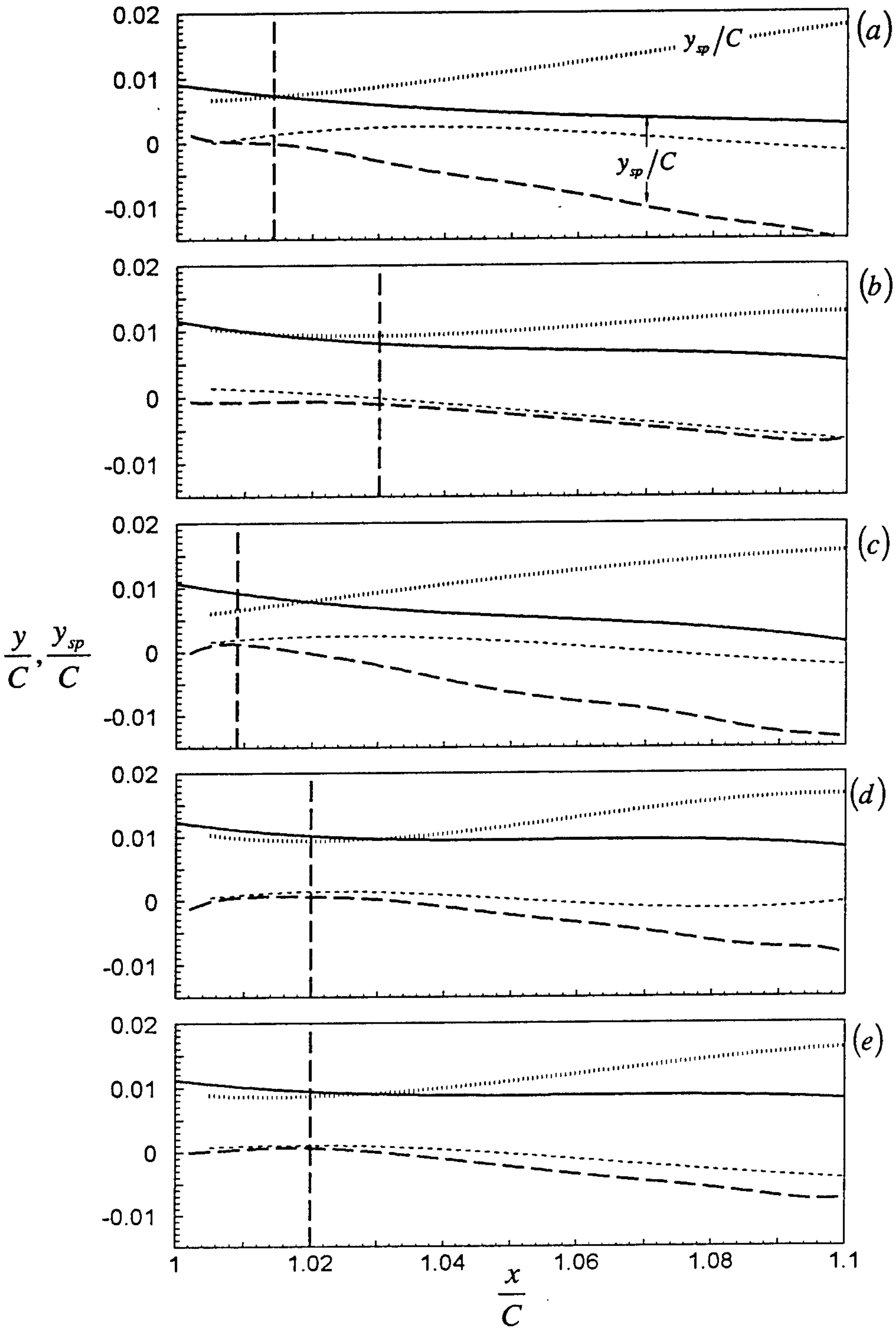
0.02
0.01
0
-0.01
y_{sp}/C
y_{sp}/C
(a)
(b)
(c)
(d)
(e)
$\frac{y}{C}, \frac{y_{sp}}{C}$
1
1.02
1.04
1.06
1.08
1.1
$\frac{x}{C}$

Fig. 26

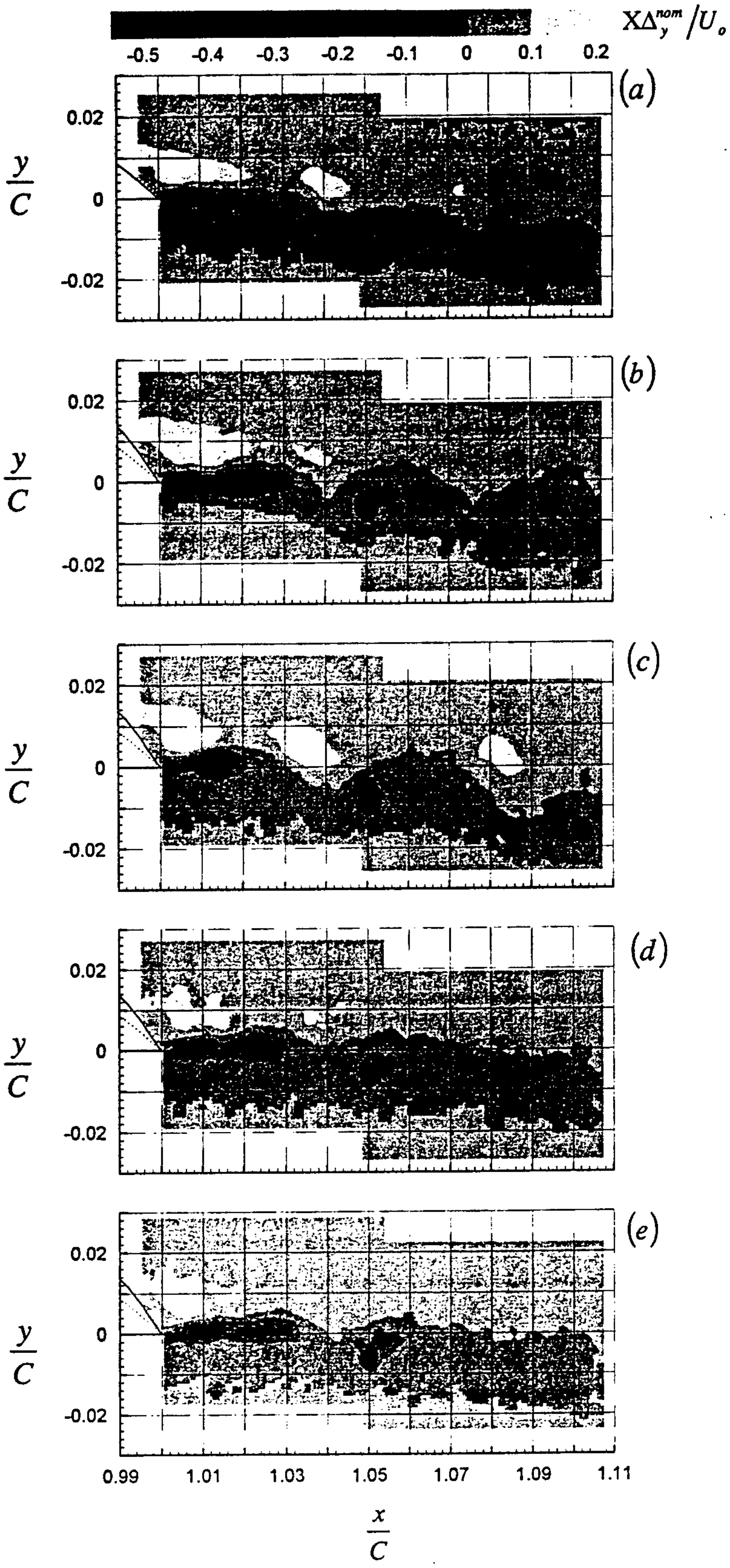
$X\Delta_y^{nom}/U_o$
-0.5
-0.4
-0.3
-0.2
-0.1
0
0.1
0.2
(a)
(b)
(c)
(d)
(e)
0.02
0
-0.02
$\frac{y}{C}$
0.99
1.01
1.03
1.05
1.07
1.09
1.11
$\frac{x}{C}$

Fig.27

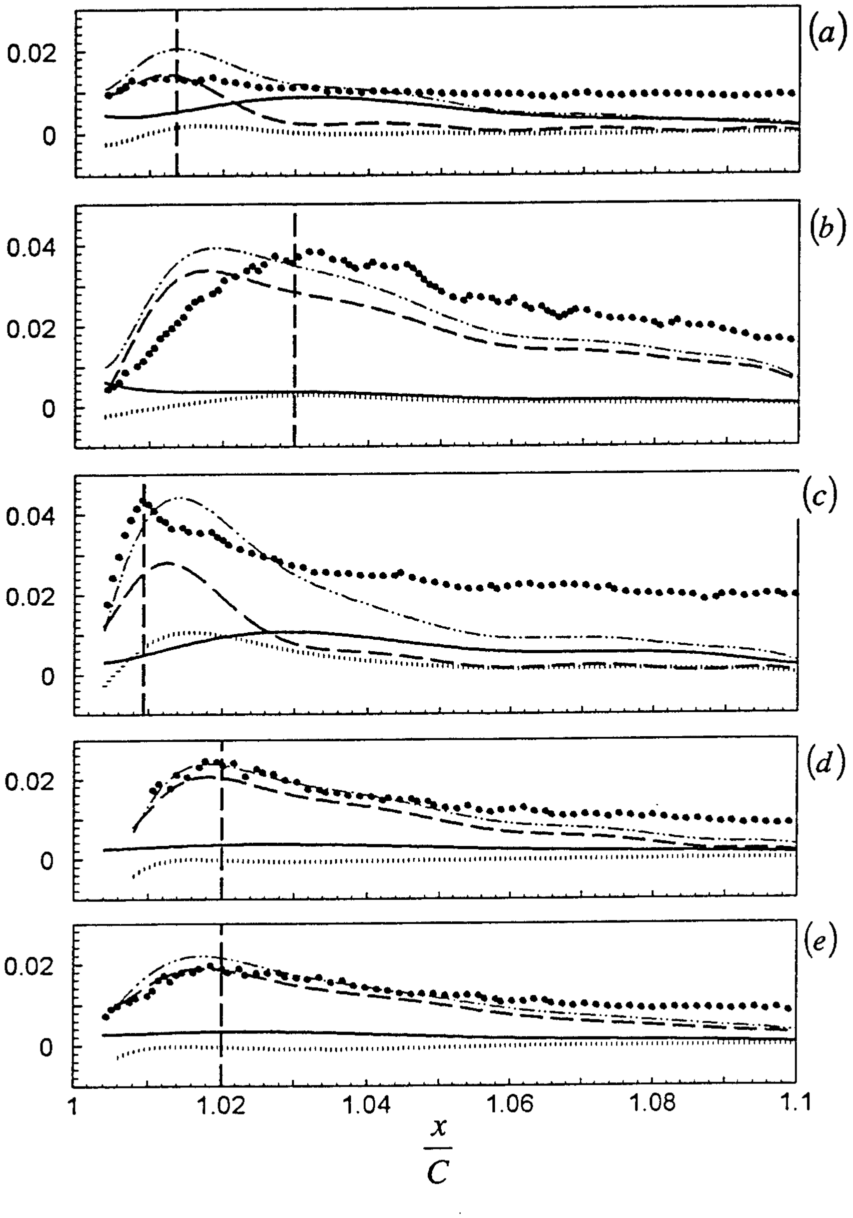

Fig. 28

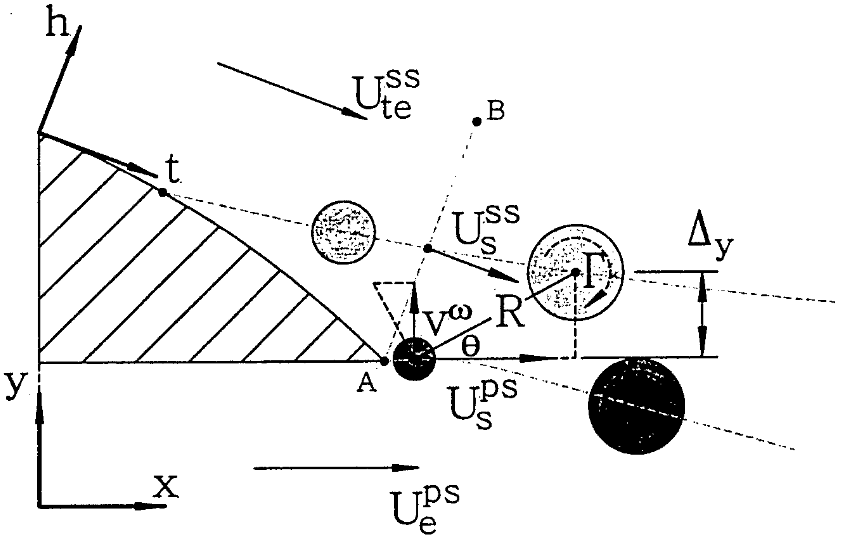
h
U_{te}^{ss}
B
t
U_s^{ss}
Δ_y
Γ
V^{ω}
R
θ
y
A
U_s^{ps}
x
U_e^{ps}

Fig. 29

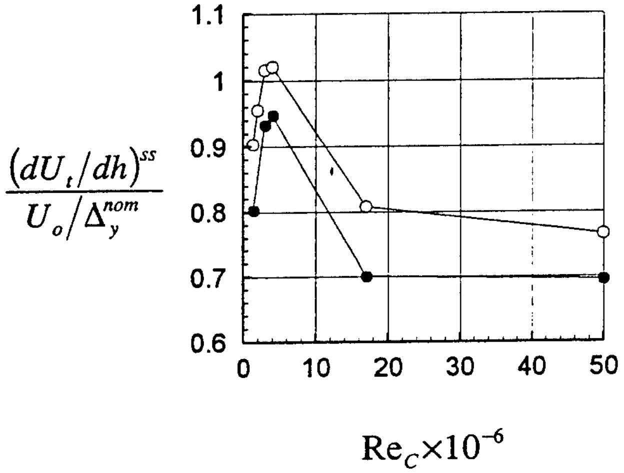
$\frac{(dU_t/dh)^{ss}}{U_o/\Delta_y^{nom}}$
1.1
1
0.9
0.8
0.7
0.6
0
10
20
30
40
50
$\mathrm{Re}_C \times 10^{-6}$

Fig. 30

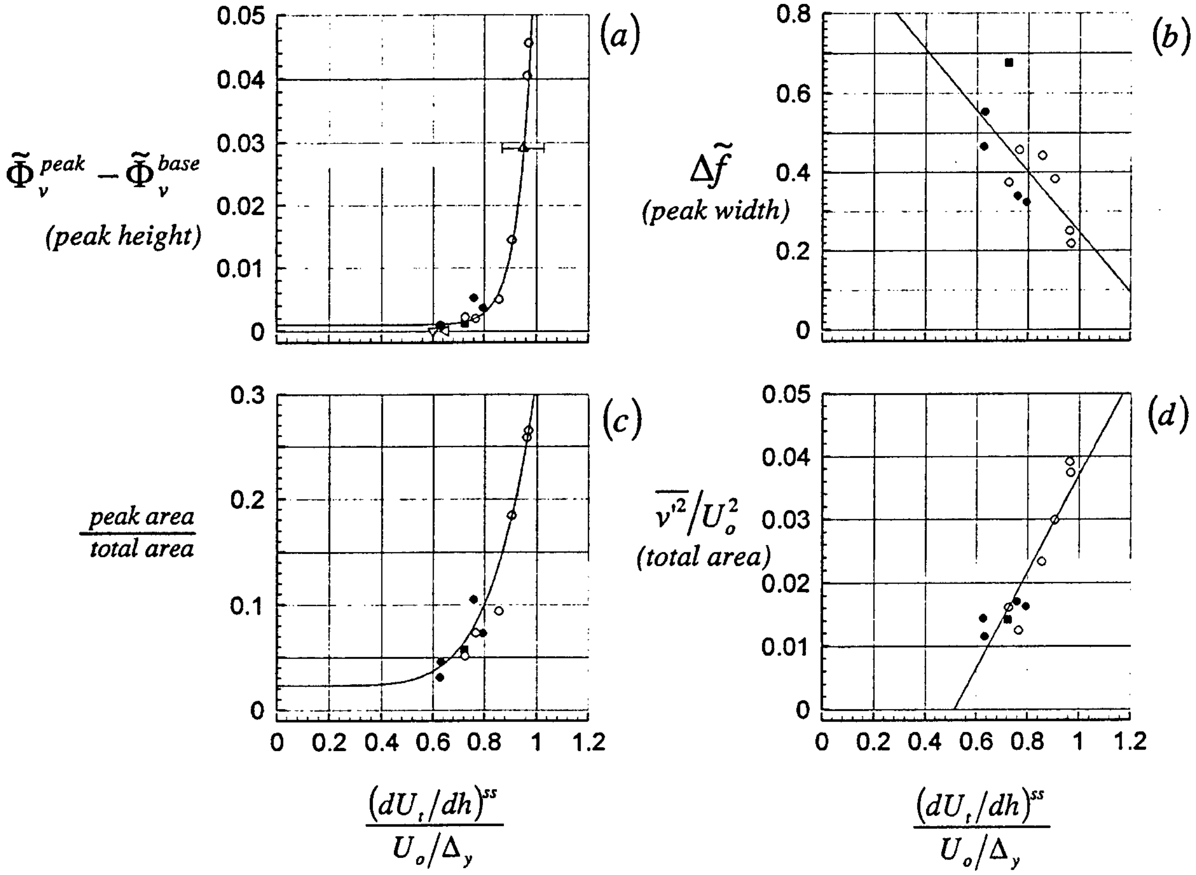
(a)
(b)
(c)
(d)
$\tilde{\Phi}_v^{peak} - \tilde{\Phi}_v^{base}$
(peak height)
0.05
0.04
0.03
0.02
0.01
0
$\Delta\tilde{f}$
(peak width)
0.8
0.6
0.4
0.2
0
peak area / total area
0.3
0.2
0.1
0
$\overline{v'^2}/U_o^2$
(total area)
0.05
0.04
0.03
0.02
0.01
0
0
0.2
0.4
0.6
0.8
1
1.2
$\frac{(dU_t/dh)^{ss}}{U_o/\Delta_y}$
0
0.2
0.4
0.6
0.8
1
1.2
$\frac{(dU_t/dh)^{ss}}{U_o/\Delta_y}$

Fig. 31